Utilization of Metal Oxide Cathode Interfacial Layer on Donor/Acceptor Solar Cells

WANG, Mingdong

A Thesis Submitted in Partial Fulfillment

of the Requirements for the Degree of

Doctor of Philosophy

in

Electronic Engineering

The Chinese University of Hong Kong
September 2011

ProQuest LLC.
789 East Eisenhower Parkway
P.O. Box 1346
Ann Arbor, MI 48106 - 1346

Acknowledgements

Firstly, I would like to express my sincere appreciation to my supervisor, Prof. Jianbin Xu, for his generous support and patient guidance at the forefront of science and technology through my Ph.D. study in The Chinese University of Hong Kong. I would also like to thank my co-supervisor, Prof. Ni Zhao, for her kind guidance and advice. I have learned from them a lot about Physics, but also a great deal about other aspects of conducting scientific research.

I would like to thank Prof. Qian Miao in the Department of Chemistry, Prof. K. Y. Wong in the Department of Physics, and Prof. Arron Ho, for their helps and advices on various occasions.

My gratitude is extended to Dr. Fanyang Xie and Prof. Jian Chen of Sun Yat-sen University for their full support and helpful discussions on XPS and UPS experiments.

I would like to thank Dr. Ning Ke for her valuable support and advices on my Ph. D. research. I wish to thank Mr W. K. Chen for his help.

I would like to express my sincere thanks to Mr. Qin Tang in the Department of Chemistry, for his full support and help on device fabrication and measurements.

I would like to thank Mr. Shizhao Zheng, and Mr. Wenguang Wong in the Department of Physics, Wang Feng in the Department of Chemistry, for their helps and advices on device fabrication and measurements.

I would like to thank to my lab maters, Dr. Jin An, Mr. Jun Du, Mr. Haixi Zhang, Dr. Weiguang Xie, Dr. Chengliang Wang, Mr. Xi Wan, Mr. Yaorong Su, Mr. Xiaomu Wang, Mr. Kun Chen, Mr. Haifei Lv, for their encouragement and appreciation.

I thank my family for their love and supports.

Abstract

By

WANG, Mingdong

Under supervision of Prof. Xu Jianbin

Co-supervision Prof. Zhao Ni

The Chinese University of Hong Kong

Electronic Engineering

September 2011

In a world of ever-increasing energy demands, organic photovoltaics (OPVs) are becoming an increasingly appealing option for renewable energy. Although the most efficient OPVs have recently reached efficiencies of 8~9.2%, there are still a number of crucial problems, particularly the device stability, that must be solved before their practical application and commercialization can be realized.

In this thesis, we find that insertion of a thermally-evaporated metal oxide layer at the cathode/organic active layer interface can significantly improve the efficiency and air stability of the OPVs. We propose that the metal oxide interfacial layer leads to a more air-resistive cathode/organic interface by stopping or minimizing penetration of thermally evaporated Al into the organic active layer, which would otherwise create a diffused organic-Al interface that will become a charge-blocking layer when exposed to air. We first verify this mechanism in poly(3-hexylthiophene)

and [6,6]-phenyl C_{61} butyric acid methyl ester (P3HT:PCBM) bulkheterojunction (BHJ) solar cells with a CrO_x cathode interfacial layer. We then exam the validity of the mechanism to other oxide interlayers, such as CuO_x, and other organic solar cell systems, including poly[(2-methoxy-5-ethylhexyloxy)-1,4-phenylenevinylene] and PCBM (MEH-PPV:PCBM) BHJ, copper phthalocyanine and C_{60} (CuPc/C_{60}) small molecular bilayer, poly(9,9-dioctylfluorene-co-bis-N, N′-(4,butylphenyl)-bis-N, N′-phenyl-1,4-phenylene-diamine) and poly(9,9-dioctylfluorene-co-benzothiadiazole) (PFB:F8BT) full-polymer BHJ. We find the extent of the stability improvement by metal oxide varies for different OPV systems, and the underlying reasons are discussed. Furthermore we design a metal oxide-LiF interfacial bilayer structure that can maintain both good stability and high open-circuit voltage (V_{oc}).

To further understand the physics of how cathode modification affects device performance, we study the limit of V_{oc} in polymeric BHJ solar cells using a double-junction model. In addition to the often-discussed donor/acceptor junction, we also consider the role of a Schottky junction formed between the cathode and the donor material. To investigate the double-junction structure, we combined measurements of AFM, XPS, UPS, impedance spectroscopy, and transient photovoltage. By studying different BHJ systems, including P3HT:PCBM, MEH-PPV:PCBM, and PFB:F8BT blend films, we found that V_{oc} is determined by the junction with a smaller negative capacitance onset and that cathode modification can tune the V_{oc} maximum from the Schottky junction limited regime to the donor/acceptor junction limited regime.

論文摘要

隨著人類發展,對能源的需求越來越大, 聚合物有機太陽能電池(OPV)激發了全世界廣大學者的研究興趣, 因為 OPV 在大面積低成本可再生能源中具有非常大的潛力。到目前, 這些研究在材料、器件及相關的理論上都取得了許多進展,此類電池最高光電轉化效率已達 8-9.2%。然而, 要想把 OPV 發展成為能真正應用的可再生能源產品,還有許多關鍵性問題需要進一步解決, 尤其是器件的穩定性。

本論文,我們利用熱蒸發所製備的氧化鉻(CrO_x)作為 P3HT:PCBM 體異質結聚合物有機太陽能電池的陰極鋁電極的介面修飾層, 能有效提高這些器件的性能以及在中空氣中的穩定性。我們認為製備 Al 電極時, 蒸發的 Al 原子擴散進入有機活性層,形成大的 Al 和有機混合介面層,這個介面層很容易被氧化而變成電荷傳輸阻擋層。然而, CrO_x 能有效阻止或減少蒸發的 Al 向有機活性層中擴散, 從而減小鋁電極和有機活性層之間的介面, 提高器件的穩定性。我們將這個機制推廣到其他氧化物半導體和其他有機太陽能電池。氧化銅(CuO_x)也能極大的提高 P3HT:PCBM 聚合物有機太陽能電池空氣中的穩定性。同樣, CrO_x 也能有效的提高 MEHPPV:PCBM 聚合物富勒烯體異質結, PFB:F8BT 全聚合物體異質結, 和 CuPc/C60 雙層小分子等太陽能電池的穩定性。CrO_x-LiF 和 CuO_x-LiF 的雙層陰極介面修飾層能進一步提高器件穩定性以及開路電壓。

為進一步理解陰極修飾對器件性能的影響,我們提出和應用 Double-Junction(雙結)模型來研究體異質結中開路電壓的限制因素。Double-Junction 模型考慮通常認為的給體和受體介面的 PN 結之外, 還考慮了給體和陰極鋁之間的肖特基結。同時應用阻抗譜和光電壓的瞬態譜來說明雙結的存在。在電壓電容關係中發現負電容效應, 其最大電容所對應的電壓落在開路電壓附近。我們認為同一個結引起負電容和限制開路電壓, 不同的陰極介面修飾, 可將開路電壓由肖特基結限制區域, 轉變為 PN 結限制區域。

Table of contents

List of Figure Captions

Page

Chapter 1

Chapter 2

Chapter 3

Chapter 4

Chapter 5

List of Table Captions

Chapter 1

Introduction

1.1 Solar energy

Solar radiation energy is essential for almost all life on Earth as it supports photosynthesis, a vital life-sustaining process, and regulates the Earth climate system. Solar radiation energy originates from the fusion of hydrogen into helium in the core of the Sun, converting lost mass into energy by the mass-energy equivalence law. Sunlight is an electromagnetic radiation with its wavelength in the region of 0.2~3.0 μ m. The solar spectrum reaching the Earth is approximated to the one of a black-body of 6,000 K with atomic absorption patterns. During its pass to the earth's surface about 30% of solar photons are absorbed and scattered by atmospheric gases (such as O_2, N_2, CO_2, SO_2, etc), cloud (aqueous vapor) and dust particles.[1-3]

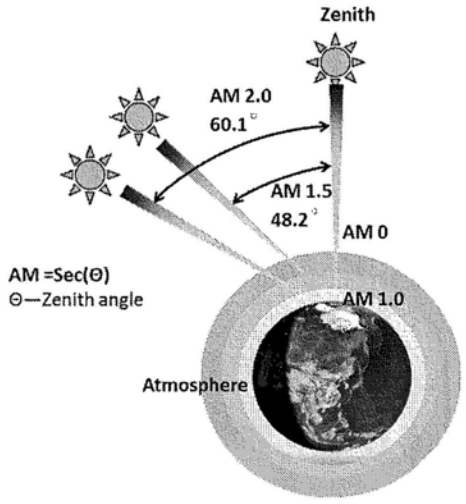

Fig. 1.1 Definition of the air mass (AM)

Air mass (AM) is defined to quantitatively describe the attenuation of sunlight (shown in figure 1), by $m=1/\cos\theta$, where θ is the angle of the sunlight incidence as

relative to the normal to the Earth's surface. It measures the ratio of the optical path length through the earth's atmosphere to the minimum path length when the sun is at zenith. During the day, θ changes from a maximum of 90° to a minimum θ_{min} at noon, which varies with the season of the year between the limits θ_{min}=latitude±23.5°. AM0 (135.3 mW/cm^2) is often used to describe the solar spectrum outside the earth's atmosphere and AM1 (92.5 mW/cm^2) is the light intensity at the earth's surface when θ is 0. AM1.5 describes the situation when θ is 48.2°, the solar spectrum of which is often used to characterize solar energy for the terrestrial conditions. In practical, a white light source that contains similar spectrum to the AM1.5 condition and has a light intensity of 100 mW/cm^2 is used as the characterization light source to measure the power conversion efficiency (PCE) of varies solar cells. [4-5]

Solar cells or photovoltaics (PV) is a technology based on semiconductor materials, it directly converts sun photons into electricity. Solar cell (module) systems have shown great potential for the future energy resource consideration because they are based on a clean technology and utilize an inexhaustible and renewable energy source. Considering both the greenhouse effect and ever-increasing energy demands of our world, solar cells are becoming an increasingly appealing option for energy production. As predicted, the world population will increase to 10 billion, and the number of required energy gap to 33 TW, by 2100 [6]. The value consumed in 2010 is ~14 TW [6]. No resource other than solar energy can alone satisfy this huge demand of our planet. In theory ~10,000 TW of the solar energy at the earth surface can be used to generate electricity via solar cells. So how can we reach 33 TW in the next 90

years if we rely on the PV technologies? For example, let solar cells with a efficiency of 10% all work 12 hours a day under light intensity of 100 mW/cm^2, to generate 33 TW energy we would need to install solar panels with total area of 660,000 km^2 (around the area of Qinghai, the fourth largest province in China). To reach this requirement, we need to make 20 km^2 solar panels every day from now on, i.e., to cover a whole Hong Kong area with solar panels in 50 days. The demand is so huge that the traditional PV technologies such as crystalline silicon solar cells and copper indium gallium selenide (CIGS) thin film solar cells can not fully complete the job.

An alternative approach to making solar cells is to use organic materials, such as small molecules and conjugated polymers. Polymer based organic solar cells offer the combined attractions of low-cost, large-scale, roll-to-roll process ability, amenability to manufacture, light weight and mechanical flexibility. Additionally, the optical and electrical properties of organic semiconductors can be tailored by functionalization of their chemical groups, rendering greater flexibility in material design than the traditional solar cell materials.

1.2 Conjugated polymer

1.2.1 Energy bands

All organic semiconductors, including polymers and small molecules as well as dyes, share in common part of their electronic structure based on conjugated π system. A typical conjugated system is one featuring an alternation between single and double bonds [7]. Butadiene and benzene are basic representative element of a conjugated

system [8]. As shown in Fig.1.2 (a), in butadiene, each carbon atom in a conjugated system has 3 nearest neighbors with which it forms 3 equivalent σ bonds made from the trigonal sp^2 hybridization of 3 valence atomic orbitals of the carbon atom: 2s, $2p_x$ and $2p_y$ for instance [9]. The σ bonds lie in the x-y plane. For such a hybridization state, the fourth orbital $2p_z$ is perpendicular to the σ bonds plane. The lateral overlap of out-of-plane $2p_z$ atomic orbitals gives the π bond. And, adjacent $2p_z$ orbitals lateral and continuously overlap from one to another, so the π electrons can jump from site to site. The more carbon atoms in a molecule, the more sites a π electron can jump to, thus π electrons are more mobile and become delocalization, which results in conductivity of organic materials [9, 10].

When the number of repeated elements increase, the molecule becomes a conductive polymer such as poly-acetylene (Fig.1.2 (b)) or thiophene (Fig.1.2 (c)) due to the delocalization of π electrons in the long chain. The π electron system essentially causes light absorption and emission, charge generation and transport. The electronic properties of polymer can be described in terms of semiconductor, in particular, one dimensional periodic solid, physics [7, 11-12]. The band gap is firstly limited by π-π^* molecule orbitals in organic semiconductor. According to the Pauli Exclusion Principle, splitting of the energy level of π orbital occurs and forms two energy bands. The Highest Occupied Molecular Orbital (HOMO) and Lowest Unoccupied Molecular Orbital (LUMO) correspond to the maximum level of valence band (VB) and minimum level of conduction band (CB) in inorganic semiconductors, shown in Fig.1.2 (c) and (d) [13]. Unlike the continuous conduction band and valence band in

most inorganic semiconductor, bands of organic semiconductor consist of numerous discrete energy levels, simplifying a Gaussian distribution of their density of state (DOS) [14].

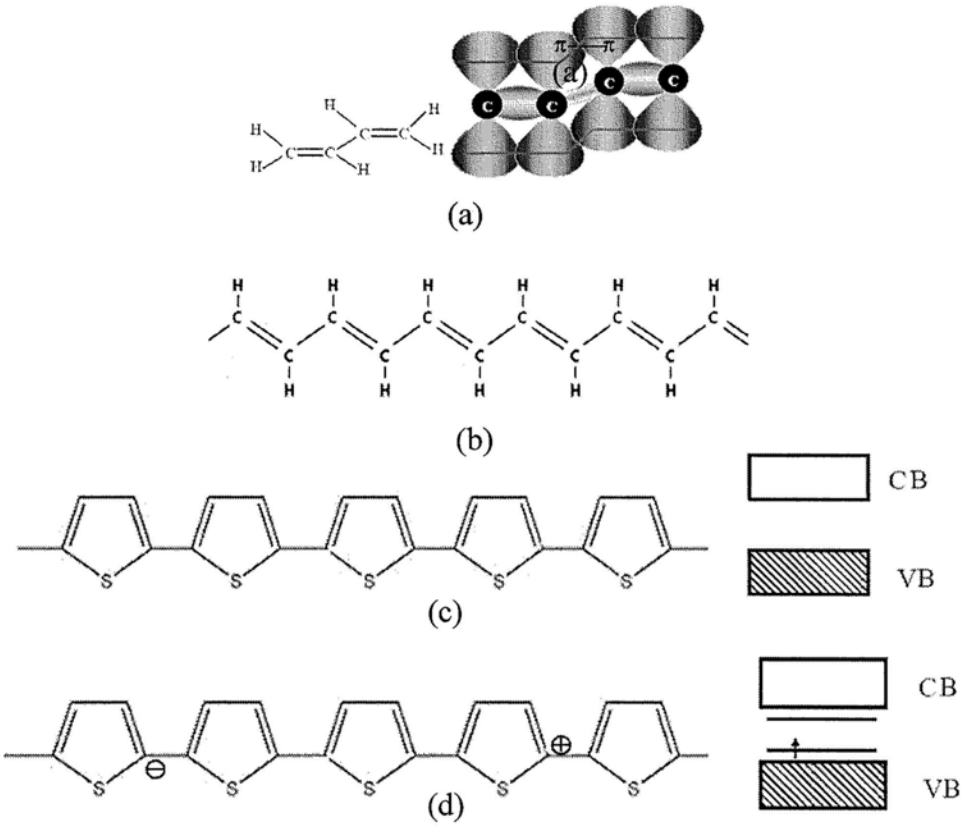

Fig.1.2 Conjugated molecules and polymers: (a) 1,3-butadiene (b) polyacetylene, (c) polythiophene and (d) charged polythiophene.

1.2.2 Transport and mobility

The nature of bonding is fundamentally different between the organic semiconductor and inorganic semiconductors. In inorganic semiconductors, strong covalent bonds hold atoms together with a well-ordered structure, e.g. Si, Ge, GaN and GaAs. The energy bands in this case are considered to be continuous in the bulk so that the carriers can move independently from each other within the bands with a

relative high mobility. By contrast, organic molecules are bonded into crystal by the Van Der Waals force, which is much weaker compared to covalent bonding in inorganic semiconductors. As a result, the mechanical and thermodynamic properties of organic semiconductors differ greatly from inorganic semiconductor, such as reduced hardness or lower melting point, but even more importantly, in a much weaker delocalization of electronic wave-function among neighbouring molecules, which directly influence optical and electrical properties [10, 15].

The hopping transport is the most commonly accepted charge transport mechanism in organic semiconductor, especially in disordered organic thin films prepared by vacuum deposition and spin-casting. Models have been given to describe the hopping transport in organic semiconductors, such as the polaron model [16], the Scher-Montroll model [17], and the Gaussian disordered model [18]. The hopping process is a temperature activated behavior and its mobiliy also depends on a applied electric field [15, 19]: $\mu(T,F) \propto \exp(-\frac{\Delta E}{kT})\exp(\frac{\beta\sqrt{F}}{kT})$, where μ is the mobility, ΔE is the activated energy, F is the electircal field, T is the termperature, and the others are constants. Furthermore, the maximum current density that can pass through a trap-free, depleted semiconductor with thickness L is given by the Mott-Gurney law [20], i.e., the space-charge-limited current (SCLC): $J_{SCLC} = \frac{9}{8}\varepsilon\mu_{dc}\frac{V^2}{L^3}$, where ε is the dielectric constant and μ_{dc} the average carrier mobility.

The mobility is crucial for the application of organic semiconductors to fabricate organic solar cells. The mobility can be experimentally determined by photocurrent

transients (time of flight) [21], space charge limited current [22], field effect transistor saturation current [23], or impedance spectroscopy [24]. The mobility in organic semiconductors is usually rather small from ~1 to 10^{-8} cm^2/Vs [7, 22-25], orders of magnitude less than that of crystalline Si. Lots of work have been done to improve the mobility in organic semiconductors. For organic solar cells with a high efficiency of ~10%, J ~20 mA/cm^2 is required at working voltage ~0.5 V. In this case, a lower limitation of the mobility is extracted as $\mu \geq 1\times10^{-4} cm^2V^{-1}s^{-1}$, with a 100 nm thick active layer and dielectric constant of 3, according to the SCLC law. The mobility of pure P3HT is ~0.1 cm^2/Vs [26], while the value drops down 3 orders of magnitude to ~10^{-4} cm^2/Vs in the P3HT:PCBM blend system. Impurities and defects in deed act as traps to heavily reduce the mobility of organic semiconductors.

1.3. Photovoltaic device principle

1.3.1 Working process

The working principle of organic solar cells is shown in Fig.1.3. The incoming photons are absorbed inside the active layer and the excitons are generated (①), excitons then diffuse into the donor/acceptor (D/A) interface (②) for dissociation into charges (③), which are finally transported into corresponding electrodes and collected (④).

Upon a photon absorption in organic solar cells, an electron is excited from the HOMO of an organic semiconductor to the LUMO. This electron-hole pair then relaxes into an exciton with a binding energy between 0.1 and 1.0 eV [27-28], a

typical Frenkel exciton. By contrast, the exciton binding energy is only a few milli-electron volts in inorganic semiconductors, a typical Wanner exciton that relaxes into a free electron and a hole due to room temperature energy of ~20 meV. The large binding energy in organic semiconductor is most likely caused by the more localized wave-functions of electrons and holes. Furthermore the lower dielectric constants (ε~3) increase the Coulomb attraction between the electron and hole. The bound excitons diffuse into an interface, where there is a sufficient energy to drive them to dissociate into free charges. It is fully known that the built-in electric field, in the depletion region between the n type region and p type, separates electrons and holes in single crystalline Si solar cells. It is thought that the offset of chemical potential energy at $LUMO_D/HOMO_A$ (>0.3 eV) can be the driving force to dissociate bound excitons to free carriers in organic solar cells [29]. In 1986, Tang made a significant jump of a efficiency to 1%, using two-layer structure which consisted of a donor/acceptor interface, in similar to a pn junction, to promote exciton dissociation and thus increase photocurrent.

After dissociation, each carrier must be transported through the layers to the appropriate contact while avoiding traps and recombination. These charges are transported by drift, although diffusion can also play an important role. Therefore, a large difference of workfunction between the anode and cathode is required to create strong built-in electric field to assist the carrier transport. The narrow absorption spectrum, poor charge transport property, small exciton diffusion length and dissociation at donor/acceptor interface limit the power conversion efficiency of

organic solar cells.

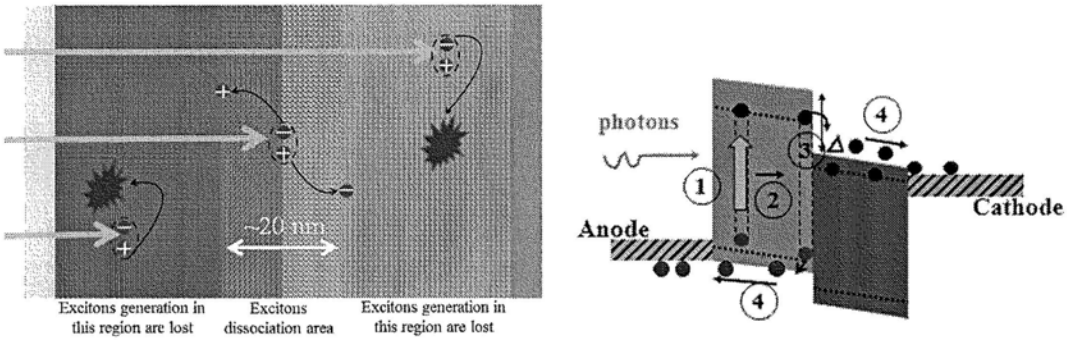

Fig. 1.3 The working process of a bilayer organic solar cell in (a) device structure and (b) energy diagram.

1.3.2 Donor-Acceptor bulk heterojunction

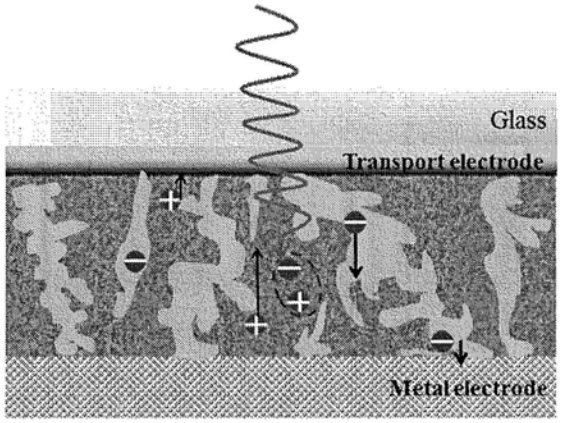

Fig.1.4 Schematic of bulkheterojunction structure of organic solar cells.

The efficiency of the planar heterojunction device is limited by the exciton diffusion length. The diffusion length of an exciton before its recombination is usually small within ~15 nm in most organic semiconductor [31-32]. As a result, the effective active volume of bilayer in OPV is limited to a very thin region close to the interface, shown in Fig.1.3, which is not enough to absorb most incident photons. As shown in

Fig.1.4, bulk heterojunction (BHJ), with nano-scale phase separation of the donor and acceptor materials in the bulk, leads to the exciton dissociation at heterojunctions throughout the bulk of the D/A blend film. Separated charges then move toward the corresponding electrodes through the bi-continuous interpenetrated networks. BHJs are usually formed by spincasting a solution of the donor material and acceptor material mixed in the same solvent. So far, BHJ is the most successful structure, demonstrated by the P3HT:PCBM and PTB7: $PC_{71}BM$ BHJ solar cells with their efficiencies of ~5% and 7.4%, respectively [33-35].

The morphology of phase separation is crucial to BHJ solar cells because it simultaneously enables both charge separation and charge collection. The size of phase separation should be within the order of $2L_D$ (L_D being an exciton diffusion length), ensuring most of the excitons have a good chance to reach the D/A interface. More importantly, the donor and acceptor respectively formed the interpenetrated networks for carrier transport to the corresponding electrode. It is difficult to observe the interconnected phase separation, with its size smaller than its diffusion length, by AFM or SEM. TEM is usually employed to investigate the phase separation between polymer and fullerene. Since the nano-morphology of BHJ blend film is difficult to control or predict, the empirical relationships between processing and performance become important. While there are some methods for fabrication of high quality BHJ films from solution, they all must be optimized with simultaneous considerations for high mobility in the organic active layer, smaller size and interpenetrated phase separation. Methods to optimize the solution-processing BHJ morphology are the

choice of solvent [36], very-slow-drying solvent additive [37], and thermal annealing process [38, 39]. In original MEHPPV:PCBM based BHJ solar cells, when the toluene is used as the common solvent, PCBM domains are over 100 nm in size. There are lots of dead regions which do not contribute to the photocurrent. However, the morphology is significantly improved by chlorobenzene or 1,2-dichlorobenzene (ODCB) solvent, a good solvent for MEHPPV and PCBM, reaching a efficiency of ~2.9% with blend ratio MEHPPV:PCBM 1:5 [40].

1.3.3 Quantum efficiency

In solar cells, the short circuit current (J_{sc}) can be described as $J_{sc} = \int \frac{q\lambda}{hc} \eta_{EQE}(\lambda) S(\lambda) d\lambda$ [41], where q is the electron charge, h is Planck constant, c is the speed of light, λ is the wavelength, $S(\lambda)$ is the spectral irradiation of the incident light, and η_{EQE} is the external quantum efficiency in the device, which indicates the ratio of the number of charges collected at the electrodes to the number of photons incident on the device. The external quantum efficiency is described via four steps as shown in Fig.1.5, and defined as: $\eta_{EQE} = \eta_A \eta_{ED} \eta_{CT} \eta_{CC}$, where η_A is the absorption efficiency of the incident photons in the photoactive region resulting in formation of excitons, η_{ED} is the probability that photo-generated excitons diffuse into the D/A interface before their recombination, η_{CT} it the charge transfer efficiency for excitons to dissociate into holes and electrons at D/A interfaces, and η_{CC} is the charge collection efficiency.

Light absorption is a common issue in all solar cells. In most organic solar cells,

only a small part of the incident photons are absorbed by the active layer. There are several causes of reduced absorption efficiency. Firstly, the bandgap is usually large in organic semiconductors. A single crystalline Si band gap of 1.1 eV can absorb 77% of the solar photons. By contrast, most used organic semiconductors have bandgaps larger than 1.85 eV (the bandgap of P3HT), limiting the possible absorption to about 27%, corresponding to a calculated maximum J_{ph}~18 mA/cm^2. Secondly, the active layer is usually thin (~100 nm) due to its poor electric property. Fortunately, the absorption coefficient (~10^{-5} cm^{-1}) is larger than that of silicon, which is necessary for 100 nm layer to absorb more than 60% of the incident light. Thirdly, the interference effect of multiple thin layers can obviously affect light density distribution in different functional layers of a device. It is necessary to optimize the device structure to enhance light absorption in the active layer, e.g. inserting TiO_x optical space between organic active layer and Al cathode [42]. Additionally, reflection losses into air should be reduced by light trapping techniques.

Ideally, all photo-induced excitons should reach a dissociation site to separate into charges. Some excitons recombine before dissociation due to limited diffusion length of ~15 nm, and thus the photons are wasted. In bilayer OPV, a trade-off between the exciton diffusion efficiency and absorption efficiency comes with varying thickness of the active layer. Exciton diffusion efficiency is greatly improved in BHJ structure, reaching over 85% [43].

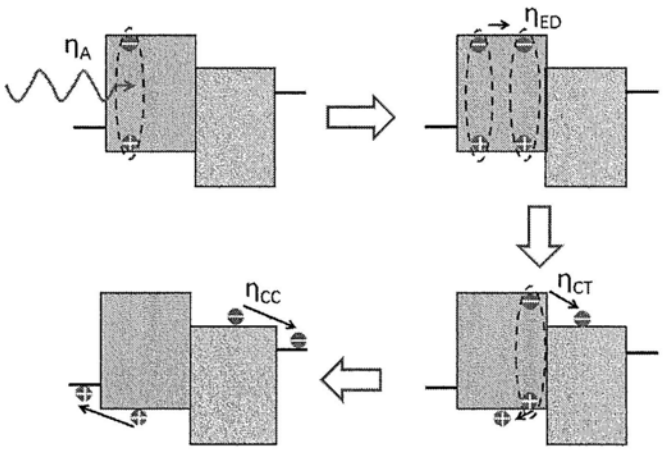

Fig.1.5 Four steps to generate the photo-current.

Charge transfer efficiency becomes appreciable when the binding energy of excitons is smaller than the offset of $LUMO_{donor}$ ($LUMO_D$) and $LUMO_{acceptor}$ ($LUMO_A$), $E_b < LUMO_D - LUMO_A$. Marcus' Theory can partially calculate charge transfer efficiency with a function of offset of $LUMO_D$-$LUMO_A$, while neglecting the contribution from tunneling [44]. Typically, it is assumed that $\eta_{CT} = 1$ in polymer-fullerene BHJ solar cells due to the rapidity (~10-100 fs) of the dissociation process [45]. However, the charge transfer efficiency might be lower in polymer-inorganic hybrid BHJ system, the photoluminescence lifetime decay is ~1 ns from the time resolved PL spectroscopy [46]. The interfacial modification of metal oxide nanorods or particle is crucial for the improvement of charge transfer efficiency. Yun reported that interface modification of a TiO_2 nanorod surface yielded a very promising device (P3HT:TiO_2 BHJ) performance of 2.20% [47].

The final contribution to external quantum efficiency is that of charge collection efficiency, which is strongly dependent on the nano-morphology and mobility of the

active blend. It can be estimated by $\eta_{CC}(V) = \frac{\mu\tau(V_{bi}-V)}{d^2}[1-e^{-\frac{d^2}{\mu\tau(V_{bi}-V)}}]$, where d is the thickness of active layer, τ the life time, μ the mobility of carrier, V_{bi} the built-in voltage, and V applied voltage. Over 90% of η_{CT}, can be reached in the P3HT:PCBM system at short circuit condition, with $\tau \sim 1.0\times10^{-4}$ s [48], $\mu \sim 1.0\times10^{-4}$ cm^2/Vs [49], a thickness of active layer 100 nm and V_{bi} is ~ 0.6 V. The trapping, recombination and low mobility are the most likely causes of reduced collection efficiency, especially in BHJ structure.

1.3.4 Characteristic solar cell parameters

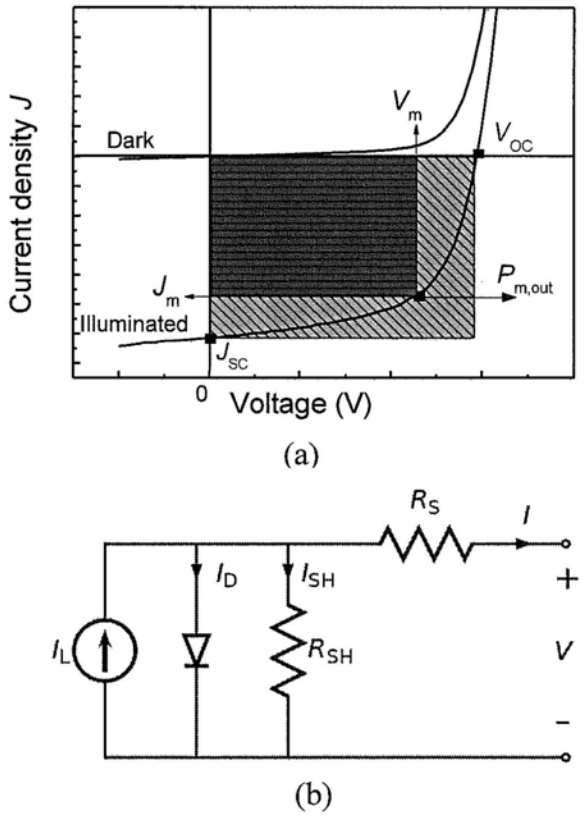

Fig.1.6 (a) Definition of efficiency and (b) a traditional equivalent circuit of solar cells.

Solar cells are electronic devices that convert light directly into electricity. The current density-voltage (*J-V*) characteristics of a solar cell in dark and under illumination are shown in Fig.1. 6. The J_{sc} is the delivering current when voltage is zero, while the open circuit voltage (V_{oc}) is the corresponding voltage when current density is zero under illumination. The solar cells can generate energy from light in its operational region $0<V<V_{oc}$. The maximum output power (P_m) in the operational region is the most energy that a cell can deliver out with corresponding current J_m and voltage V_m. Thus, the power conversion efficiency can be expressed by $\eta = \frac{P_m}{P_0} = \frac{J_m V_m}{P_0} = \frac{J_{sc} V_{oc} FF}{P_0}$, $FF = \frac{J_m V_m}{J_{sc} V_{oc}}$, where P_0 is the incident light power and the FF the calculated fill factor.

The commonly used Shockley model [1, 50] for solar cells (shown in Fig.1.6) is $J = J_0(e^{\frac{q(V-JR_s)}{nk_BT}} - 1) + \frac{V - JR_s}{R_{sh}} - J_{ph}$, where J_{ph} is the photocurrent, J_0, the saturation current, n the ideal factor, k the Boltzman constant, T the temperature, R_s the series resistance, R_{sh} the shunt resistance. In organic solar cells, the series resistance R_s is relatively higher than those of in inorganic devices, caused by poor mobility of the active layer and non-ideal contact resistance between the organic active layer and metal, or organic polymer and oxides. It is suggested that the R_p is dominated by D/A interface or depletion region at electrodes and the high purity and low carrier concentration means large parallel resistance. The lower FF in organic solar cells is sometimes primarily controlled by both higher R_s and lower parallel resistance R_p, by

a simplified expression of $FF(R_s, R_p) = FF(0,\infty)(1 - \frac{J_{sc}R_s}{V_{oc}} - \frac{V_{oc}}{J_{sc}R_p})$ [1, 50]. Both resistances need to be optimized to obtain a high performance in organic solar cells.

1.4 Development of organic solar cells

The photovoltaic effect was firstly discovered by French physicist Antoine-César Becquerel in 1839 in electrochemical cells [51]. At the beginning, Se and Cu-CuO_2 rectifiers with barriers on front and back sides was studied as potential solar cells. With improvements in Si technology, a Si PV solar cell was produced by formation of a pn junction during crystal growth and patented in 1946 by Russell Ohl [52]. In 1954, three American researchers, Gerald Pearson, Calvin Fuller and Daryl Chapin, designed a silicon wafer solar cell capable of 6% power conversion efficiency by the diffusion technology in Bell Laboratories [53, 54]. The oil crisis occurred in 1974, and the fragility of the energy source (the black blood of oil) upon which modern world civilization was built was exposed. Since then, efforts on renewable energy, particularly in photovoltaics, have intensively increased. The cost of PV production has significantly decreased, and various inorganic semiconductors such as GaAs, CdTe, and CIGS have successfully developed into second generation solar cells based on thin film deposition technologies such as chemical vacuum deposition (CVD) [1-2, 55]. Although an industrial era of photovoltaics based on silicon and second generation solar cells is beginning, PV research continues to be motivated by reduction of the cost, protection of the environment, and limitation of the raw materials on our earth.

Emerging PVs including dye sensitized solar cells, organic-inorganic hybrid solar cells, small molecule solar cells, and polymer based solar cells are developing into practical application. It has been over 30 years to study organic solar cells. At the beginning, ITO\organic\Al, a single layer structure was used. In 1986, a typical two layer organic solar cells made by Tang W. C. based on copper phthalocyanine (CuPc) (donor material) and perylene tetracarboxylic derivatives (acceptor material) reached 1% efficiency [30]. In 1995, A. J. Heeger group demonstrated an enhanced efficiency of over 2% by using MEHPPV:PCBM BHJ structure, which overcomes the drawbacks of bilayer structure [40]. With better control of nano-scale phase separation, P3HT:PCBM solar cells reached over 5% efficiency with suitable solvent and annealing process in several groups around 2005 [33-34, 56]. Compared to PPV, P3HT has higher mobility due to the semicrystalline nature of its spin-cast thin film, and smaller size of nanoscale phase separation for exciton quenching [57].

For the last 3 years, significant progress in organic solar cells has been made as shown in Fig.1.7. New lower bandgap polymers were designed to obtain higher efficiency with increased light absorption. In 2009, Sung reported that poly[N-900-hepta-decanyl-2,7-carbazole-alt-5,5-(40,70-di-2-thienyl-20,10,30-benzothiadiazole) (PCDTBT): fullerene derivative [6,6]-phenyl C_{70}-butyric acid methyl ester ($PC_{70}BM$) BHJ solar cells have the internal quantum efficiency approaching 100% with its efficiency of 6.1% [58]. In following year, an efficiency of 7.4% was achieved in PTB7:$PC_{71}BM$ BHJ solar cells. Solarmer, a company focusing on OPV, broke a psychological barrier with 8.13% efficiency in 2010 [59].

Alternatively, using tandem structure overcomes the limited absorption spectra of organic semiconductors.

Many attempts have also been made in organic-inorganic hybrid solar cells, replacing the fullerene with high mobility inorganic nanocrystals such as CdS [60], CdSe [61], TiO_2 [62] and ZnO [63]. It is crucial for modification of organic-inorganic interface to improve charge transfer efficiency as well as controlling BHJ morphology.

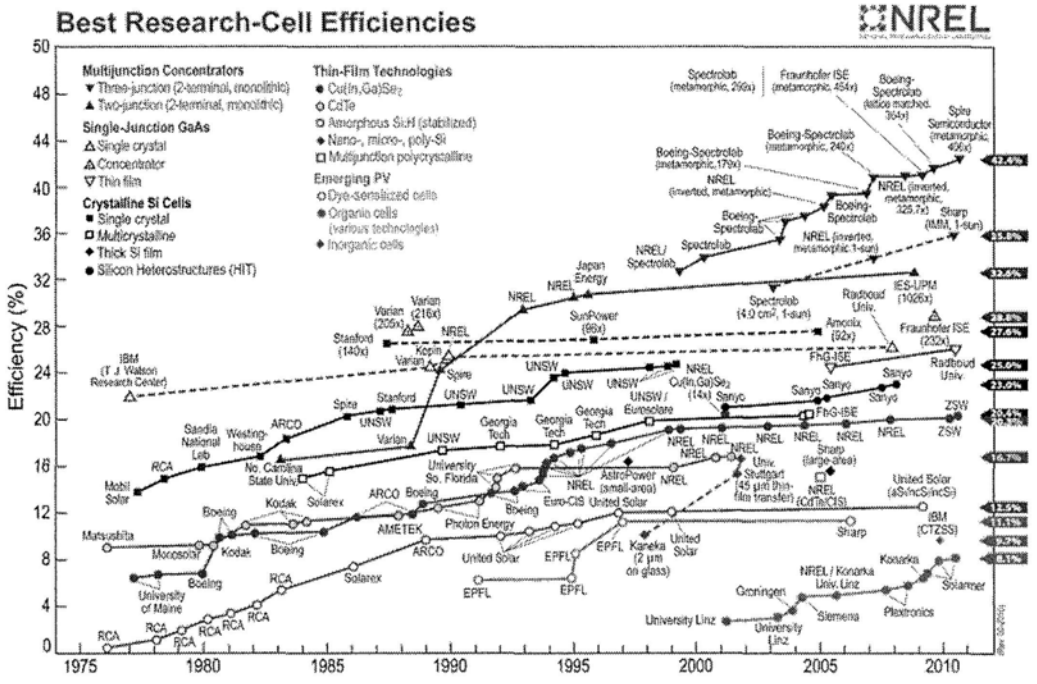

Fig.1.7 Development of organic solar cells [64].

1.5 Application and future market opportunities

1.5.1 Efficiency improvement

Organic solar cells promise lightweight and large-area solar panels for commercialization. However, the technology must simultaneously meet three important requirements: high efficiency, low cost and long lifetime. As shown in

Table 1.1 [56, 59, 65-74], single crystalline silicon solar cells have a lab efficiency of over 24% and 14%-17% for industry products. OPV efficiency has only reached ~8%, which has been comparable to the value of commercial amorphous silicon solar cells of 6%-8% (the lab recorded efficiency is 10.1%) [69]. In order to improve the efficiency of OPV, the development of new materials and optimization of device physics are necessary. And there is still much room for improvement of J_{sc} to obtain over 10% efficiency. The J_{sc} can be increased by broadening absorption spectrum and fine controlling nano-morphology phase separation. It is important to extend the absorption edge of polymer from 650 nm to 900 nm to double the light harvest, by using new lower bandgap polymers. Besides, it is also a good option to develop organic-inorganic hybrid solar cells using small bandgap inorganic semiconductor, such as quantum dots of PbS, CdSe, Cu_2S and so on.

Another method of obtaining 10% efficiency is to reduce the V_{oc} loss. P3HT has a LUMO of ~3.3 eV, while PCBM having a LUMO of 3.7 eV [75]. There is an energy offset of approximately 0.4 eV ($LUMO_D$-$LUMO_A$) which is used as driving force for exciton dissociation and charge transfer. It is commonly accepted that V_{oc} is limited by $HOMO_D$-$LUMO_A$ -Δ eV, and Δ is suggested to be ~0.3 [76]. The Δ in fact is not a constant value in different D/A system, even changing with D/A ratio in the same materials system. The $HOMO_D$-$LUMO_A$ is ~1.3 eV in P3HT:PCBM blend, but the V_{oc} is ~0.6 V. The loss mechanism is not clear so far. However, the changes of $HOMO_D$ and $LUMO_A$ can effectively alter V_{oc}. One of the advantages of organic semiconductors is the ability to shift energy levels by incorporating different

functional groups to alter the molecule structure. As a result, selecting proper functional groups to match the donor/acceptor energy levels can effectively increase the V_{oc}.

Table 1.1 Parameters of different kinds of solar cells.

cells	Efficiency (%)	V_{oc} (V)	J_{sc}(mA/cm^2)	FF(%)	Ref
Organic					
Dye sensitized	11.1	0.736	20.9	0.722	[65]
polymer	8.13	0.757	14.95	0.67	[59]
P3HT:PCBM	5.2	0.64	11.3	0.69	[56]
small molecule	5.0	0.54	15.0	0.61	[66]
small molecule tandem	8.3	--	--	--	[67] Heliatek
Inorganic					
Si (crystalline)	25.0±0.5	0.706	42.7	0.828	[68]
Si (amorphous)	10.1±0.3	0.886	16.75	0.67	[69]
GaAs(crystalline)	27.6±0.8	1.107	29.6	0.841	[70]
InP(crystalline)	22.1±0.7	0.878	29.5	0.854	[71]
CuInGaSe (CIGS)	19.4±0.6	0.716	33.7	0.803	[72]
CdTe	16.7±0.5	0.845	26.1	0.755	[73]
GaInP/GaAs tandem	30.3	2.488	14.22	0.856	[74]

1.5.2 Stability improvement

Polymer based solar cells have the potential to be competitive in the marketplace. Inorganic silicon-based solar cells can work for more than 25 years, while the goal for OPV has always been 10% efficiency and a 10-year lifetime. There is still lot of work to be done to tremendously improve this technology for practical applications.

Organic materials are by nature more susceptible to chemical degradation from oxygen and water than inorganic materials, which relates to its molecule structure and the order of structure between molecules. Stability is one of the key issues of organic

devices. Although a lot of works relating to the stability of OLEDs and PLEDs reported in the last two decades are highly relevant for polymer or small organic solar cells, the contributing factors to the degradation may change because the two kinds of devices work under different conditions: OLEDs work under larger electric fields; while OPVs work at lower voltage (usually <1 V); and the work principles are also opposite.

The decrease of OPV's efficiency seems to be caused by changes of morphology and degradation of interfaces [77-78]. Importantly, polymer-based organic solar cells are known to offer a poor stability in real application conditions, and the photo-degradation of the active layer plays a role in the reduced lifetime of the devices. MDMO-PPV and P3HT thin films were submitted to photo-ageing (wavelength >300 nm) in the presence and in the absence of oxygen [80]. Photons with higher energy can assist the oxidation of side chains of organic molecules due to their weaker bonds, as listed in Table 1.2 [81-82], to degrade the conjugated polymer in both conductivity and absorption. When PCBM is present into polymer however, the polymer-fullerene blend was shown to be much more stable under illumination. PCBM protects the polymer by acting as a radical scavenger, absorbing higher energy photons and accepting photon-induced electrons very quickly [80, 83-84]. If deposited on an inert substrate and well protected from oxygen and water with a convenient encapsulation, P3HT:PCBM based active layer should be intrinsically stable for several years of use, and there was almost no degradation of absorption after ~5000 h of irradiation [80,85].

Table 1.2 Bonding energy in organic materials.

Chemical bonds	Bonding energy (eV)	Wavelength (nm)
C=O	7.76	160
C=C	6.33	196
O-H	4.81	258
C-H	4.29	290
N-H	4.03	308
C-O	3.73	333
C-C	3.60	345
C-N	3.16	393
S-C	2.82	440
S=C	5.95	209
S-O	3.78	329
S=O	5.42	229
O-O	1.47	845
O=O	5.13	242

Al is most commonly used low work function metal as a top electrode. However, low work function metals are susceptible to oxidation when exposed to air, leading to the formation of an insulating barrier (such as Al_2O_3) that hinders charge extraction. More importantly, the low workfunction metal may react with the organic active layer. PCBM have a very high electron affinity and would seem more prone to react with a metal electrode [83]. It is also demonstrated that the Al-C_{60} bond formed would dominate the charge transport at interface [86]. So a more air-stable and low cost metal with similar work function is favorable to replace Al. An alternative method is to use interfacial layers to effectively improve the stability of the Al electrode.

1.6. Motivation and outline of this thesis

Although great progress has been made, the efficiency and stability of current

polymer based BHJ solar cells can not satisfy the requirements of real application and commercialization. The main motivations of this thesis are to understand the degradation mechanisms of organic solar cells, to develop new strategies that can be used to improve device stability and are compatible with device flexibility and ease of fabrication, and to achieve an in-depth insight into the relationship between the device structure and the limitation of V_{oc} of organic solar cells. The rest of the thesis is organized as follows:

In Chapter 2, instrumentation and experimental procedures are introduced. Fabrication of organic solar cells is commonly based on a solution process and thermal evaporation.

In Chapter 3, I fabricate prototype organic solar cells with P3HT:PCBM active layer and Al cathode and use them to investigate the degradation mechanisms of the solar cells in air. I then focus on the thermally evaporated chromium oxide (CrO_x) as a cathode interfacial layer to improve the device efficiency and air stability. More than 100 times improvement in device lifetime is observed and the driven mechanism is proposed and discussed.

In Chapter 4, I extend the previously proposed mechanism of device degradation and stability improvement to other metal oxides and organic solar cell systems. Firstly, I investigate the use of CuO_x as a cathode interfacial layer to increase the device lifetime of P3HT:PCBM BHJ solar cells. Following that I demonstrate that the CrO_x cathode interfacial layer can be applied to a variety of organic solar cell systems to improve the device stability. I show that the extent of the stability improvement varies

for different systems. Possible degradation mechanisms in these cells are discussed.

In chapter 5, I utilize the different cathode interfacial layers to study the limit of V_{oc} in polymeric BHJ solar cells. A double-junction model is proposed: In addition to the often-discussed donor/acceptor junction, I also consider the role of a Schottky junction formed between the Al cathode and the donor material. The existence of such double junction structure is confirmed by Atomic force microscopy (AFM), X-Ray photoelectron spectroscopy (XPS), Ultraviolet photoemission spectroscopy (UPS), impedance spectroscopy and transient photovoltage measurement, and its relation with V_{oc} are discussed.

In Chapter 6, I provide a summary of the major contributions of this thesis and suggest a few future research directions that could be pursued to follow up this work.

References:

[1] M. A. Green, Solar cells: Operation Principles, Technology, and System Applications, University of New South Wales, Australia (1986).

[2] J. Poortmans and V. Arkhipov, Thin film solar cells fabrication, characterization and application, Wiley, UK (2006).

[3] http://en.wikipedia.org/wiki/Sun

[4] http://rredc.nrel.gov/solar/spectra/am1.5

[5] R. E. Bird, R.L. Hulstrom, L. J. Lewis, Sol. Energy, 30, 563 (1983).

[6] M. I. Hoffert, K. Caldeira, A. K. Jain, E. F. Haites, L. D. D. Harveyk, S. D. Potter, M. E. Schlesinger, S. H. Schneider, R. G.Watts, T. L. Wigley and D. J. Wuebbles, Nature, 395,881 (1998).

[7] J. M. Marshall and D. Dimova-Malinovska, Photovoltaic and photoactive materials properties, technology and application, Kluwer Academic Pulishers, USA, (2002).

[8] L. Salem, The molecular orbital theory of conjugated systems, Benjanmin, New York (1966).

[9] F. A. Carey and R. J. Sundberg, Advanced Organic Chemistry: Structure and mechanisms, Springer, Germany (2008).

[10] F. So, Organic electronics materials, processing, device and application, CRC Press, FL (2010).
[11] Kun Huang, Solid states physics, Peking University press, China (2009).
[12] C. Cojan, G. P. Agrawal, C. Flytzanis, Phys. Rev. B, 15, 909, (1977).
[13] R. Hoffmann, C. Janiak, and C. Kollmar, Macromolecules, 24, 3725 (1991).
[14] A. J. Campbell, D. D. C. Bradley, and D. G. Lidzey, J. Appl. Phys. 82, 6326 (1997).
[15] W. Brütting, Physics of organic semiconductors, Wiley-VCH, Germany (2008).
[16] D. Emin, Phys. Rev. Lett. 32, 303 (1974).
[17] H. Scher and E. W. Montroll, Phys. Rev. B 12, 2455 (1977).
[18] H. Bässler, Phys. Status Solidi B 15, 175 (1993)
[19] S. W. Tsang, Charge Carrier Transport and Injection across Organic Heterojunctions, PHD thesis, University of Toronto, Canada (2009).
[20] M. A. Lambert, P. Mark, Current Injection in Solids, Academic Press, New York, (1970).
[21] R. G. Kepler, P. M. Beeson, S. J. Jacobs, R. A. Anderson, M. B. Sinclair, V. S. Valencia and P. A. Cahill, Appl. Phys. Lett. 66, 3618 (2000).
[22] M. Giulianini, E. R. Waclawik, J. M. Bell and N. Motta, Appl. Phys. Lett. 94, 083302 (2009).
[23] R. J. Kline, M. D. McGehee, E. N. Kadnikova, J. S. Liu and J. M. J. Frechet, Adv. Mater. 15, 1519 (2003).
[24] S. W. Tsang, S. K. So, and J. B. Xu, J. Appl. Phys. 99, 013706 (2006).
[25] E. G. Thianche, C. Sentein, A. Lorin, C. Denis, P. Raimond and J.M. Nunzi, J. Appl. Phys, 83, 4236 (1998).
[26] H. Sirringhaus, P. J. Brown, R. H. Friend, M. M. Nielsen, K. Bechgaard, B. M. W. Langeveld-Voss, A. J. H. Spiering, R. A. J. Janssen, E. W. Meijer, P. Herwig and D. M. de Leeuw, Nature, 401, 685 (1999).
[27] C. Deibel, T. Strobel and V. Dyakonov, Adv Mater, 22, 4097 (2010)
[28] I .Hill, A. Kahn, Z. Soos and R. Pascal, Chem. Phys. Lett. 327, 181 (2000).
[29] E. Silinsh, V. Capek, Organic molecular crystals, AIP press: Woodbury, New York, (1994).
[30] C. W. Tang, Appl. Phys. Lett. 48, 183 (1986).
[31] P. W. M. Blom, V. D. Mihailetchi, L. J. A. Koster and D. E. Markov, Adv. Mater, 19, 1551 (2007).
[32] S. R. Scully and M. D. McGehee J. Appl. Phys. 100, 034907 (2006).
[33] W. Ma, C. Yang, X. Gong, K. Lee, A. J. Heeger. Adv. Funct. Mater. 15, 1617 (2005)
[34] M. Reyes-Reyes, K. Kim, and D. L. Carroll, Appl. Phys. Lett, 87, 083506 (2005)
[35] Y. Liang, Z. Xu, J. Xia, S.-T. Tsai, Y. Wu, G. Li, C. Ray and L. Yu, Adv. Mater.

22, E135 (2010).
[36] S. Alem, R. D. Bettignies, J. -M. Nunzia and M. Cariou, Appl. Phys. Lett. 84, 2178 (2004).
[37] J. Peet, C. Soci, R. C. Coffin, T. Q. Nguyen, A. Mikhailovsky, D. Moses and G. C. Bazan, Appl. Phys. Lett. 89, 252105 (2006).
[38] G. Li, V. Shrotriya, J. Huang, Y. Yao, Tommoriarty, K. Emery and Y. Yang Nature Materials, 4, 864 (2005).
[39] S. Wu, J. Li, Q. Tai and F. Yan, J. Phys. Chem. C 114, 21873 (2010).
[40] G. Yu, J. Gao, J. C. Hummelen, F. Wudl and A. J. Heeger, Science, 270, 1789 (1995).
[41] B. P. Rand, J. Genoe, P. Heremans and J. Poortmans, Prog. Photovolt.: Res. Appl. 15, 659 (2007).
[42] K. Lee, J. Y. Kim, S. H. Park, S. H. Kim, S. Cho, A.J. Heeger, Adv. Mater. 19, 2445 (2007).
[43] S. D. Oosterhout, M. M. Wienk, S. S. V. Bavel, R. Thiedmann, L. J. A. Koster, J. Gilot, J. Loos, V. Schmidt and R. A. J. Janssen, Nature Mater. 8, 818 (2009).
[44] R. A. Marcus and N. sutin, Biochimica et Biophysica Acta 811, 265 (1985).
[45] F. Yang and S. R. Forrest, ACS Nano 5 1022 (2008).
[46] Y. Y. Lin, C. W. Chen, T. H. Chu, W. F. Su, C. C. Lin, C. H. Ku, J. J. Wu and C. H. Chen, J. Mater. Chem. 17, 4571 (2007).
[47] Y. Y. Lin, T. H. Chu, S. S. Li, C. H. Chuang, C. H. Chang, W. F. Su, C. P. Chang, M. W. Chu, and C. W. Chen, J. Am. Chem. Soc. 131, 3644 (2009).
[48] G. Garcia-Belmonte, A. Munar, E. M. Barea, J. Bisquert, I. Ugarte and R. Pacios, Organ. Electron. 9, 847 (2008).
[49] V. D. Mihailetchi, H. Xie, B de Boer, L. J. Koster, P. W. M. Blom, Adv. Funct. Mater. 16, 699 (2006).
[50] R. Bube and A. Fahrenbruch, Advances in Electronics and Electron Physics, Vol. 56. Academic Press: New York, (1981).
[51] http://en.wikipedia.org/wiki/Solar_cell
[52] "Light sensitive device" U.S. Patent 2,402,662 Issue date: June (1946).
[53] J. Perlin, The Silicon Solar Cell Turns 50, National Renewable Energy Laboratory, http://www.nrel.gov/docs/fy04osti/33947.pdf (2004).
[54] D. M. Chapin, C. F. Fuller, and G. L. J. Pearson, Appl. Phys. Lett. 25, 676 (1954).
[55] P. Würfel, Physics of solar cells: from principles to new concepts, Wiley-VCH, Germany (2005).
[56] M. D. Irwin, D. B. Buchholz, A. W. Hains, R. P. H. Chang, and T. J. Marks, PNAS, 8, 2783 (2008).
[57] H. Wang, H. Y. Wang, B. R. Gao, L. Wang, Z. Y. Yang, X. B. Du, Q. D. Chen, J.

F. Song and H. B. Sun, Nanoscale, 3, 2280 (2011).
[58] S. H. Park, A. Roy, S. Beaupre, S. Cho, N. Coates, J. S. Moon, D. Moses, M. Leclerc, K. Lee, and A. J. Heeger, Nature photonics, 3, 297 (2009).
[59] http://www.solarmer.com
[60] H. C. Liao, S. Y. Chen, and D. M. Liu, Macromolecules 42, 6558 (2009).
[61] W. U. Huynh, J. J. Dittmer, A. P. Alivisatos, Science, 295, 2425 (2002).
[62] Y. Y. Lin, T. H. Chu, C. W. Chen, and W. F. Su, Appl. Phys. Lett. 92, 053312 (2008).
[63] W. J. E. Beek, M. M. Wienk and R. A. J. Janssen, Adv. Mater. 16,1009 (2004).
[64] www.nrel.gov/pv/thin_film/docs/kaz_best_research_cells.pp
[65] Y. Chiba, A. Islam, Y. Watanabe, R. Komiya, N. Koide and L. Han, Jpn. J. Appl. Phys. 45, L638 (2006).
[66] J. Xue, B. P. Rand, S. Uchida, S. R. Forrest, Adv. Mater. 17, 66 (2005).
[67] http://www.heliatek.com
[68] J. Zhao, A. Wang, M. Green, F. Ferrazza, Appl. Phys. Lett. 73, 1991 (1998).
[69] S. Benagli, D. Borrello, E. Vallat-Sauvain, J. Meier, U. Kroll, 24th European Photovoltaic Solar Energy Conference, Hamburg, (2009).
[70] M. A. Green, K. Emery, Y. Hishikawa and W. Warta, Prog. Photovolt: Res. Appl. 18, 346 (2010).
[71] C. J. Keavney, V. E. Haven and S. M. Vernon, Conference Record 21st IEEE Photovoltaic Specialists Conference, Kissimimee, 141 (1990).
[72] I. Repins, M. A. Contreras, B. Egaas, C. DeHart, J. Scharf, C. L. Perkins, B. To, R. Noufi, Progress in Photovoltaics: Research and Applications 16, 235 (2008).
[73] X. Wu, J. C. Keane, R. G. Dhere, C. DeHart, A. Duda, T. A. Gessert, S. Asher, D. H. Levi, P. Sheldon, Proceedings of the 17th European Photovoltaic Solar Energy Conference, 995, Munich, (2001).
[74] M. Ohmori, T. Takamoto, E. Ikeda, H. Kurita, High efficiency InGaP/GaAs tandem solar cells, Techical Digest, International PVSEC-9, Miyasaki, 525, (1996).
[75] J. Y. Kim, S. H. Kim, H. H. Lee, K. Lee, W. Li, X. Gong, A. J. Heeger, Adv. Mater. 18, 572 (2006).
[76] M. C. Scharber, D. Mühlbacher, M. Koppe, P. Denk, C. Waldauf, A. J. Heeger and C. J. Brabec, Adv. Mater. 18, 789 (2006).
[77] B. Conings, S. Bertho, K. Vandewal, A. Senes, J. D'Haen, J. Manca, R. A. J. Janssen, Appl. Phys. Lett. 96, 163301 (2010).
[78] M. D. Wang, Q. Tang, J. An, F. Xie, J. Chen, S. Zheng, K. Wong, Q. Miao, J. B. Xu, ACS Appl. Mater. Inter.10, 2699 (2010).
[79] M. D. Wang, F. Y. Xie, W. G. Xie,S. Z. Zheng, N. Ke, J. Chen, N. Zhao, and J. B. Xu, Appl. Phys. Lett. 98, 183304 (2011).

[80] A. Rivaton, S. Chambon, M. Manceau, J. Gardette, N. Lemaître and S. Guillerez, Polym. Degrad. Stab. 95, 278 (2010).

[81] http://www.uksaf.org/data.html

[82] D. R. Lide, CRC Handbook of Chemistry and Physics, 87th Edition, CRC Press, (2006).

[83] M. Jørgensen, K. Norrman, F. C. Krebs, Sol. Energy Mater. Sol. Cells, 92 686 (2008).

[84] K. Kawano, R. Pacios, D. Poplavskyy, J. Nelson, D. D. C. Bradley and J. R. Durrant, Sol. Energy Mater. Sol. Cells, 90, 3520 (2006).

[85] B. Zimmermann, U.Wurfel and M. Niggemann, Sol. Energy Mater. Sol. Cells 93, 491 (2009).

[86] J. Nishnaga, T. Aihara, H. Yamagata, Y. Horikoshi, J. Cryst. Growth 278, 633, (2005).

Chapter 2

Experimental procedure and characterization technology

2.1 Overview

Fabrication of organic solar cells (OPVs) is mostly based on a solution process and thermal evaporation, which is simple compared to that of traditional inorganic solar cells. However, the interfacial layers and fabrication process are essential in order to make the OPVs with high efficiency and stability. Since organic solar cells, particularly BHJ structure, are essentially nano-electronic devices due to their phase separation in nano-scale, with an active layer about 100 nm and different engaged interfacial layers ranging from 0.6 nm to 40 nm. Additionally, the organic materials are sensitive to oxygen and water molecules, causing the rapid degradation of devices in air. Therefore, the operation of instruments, fabrication procedures and characterizations should be carefully controlled.

In this chapter, the instruments, fabrication processes and characterizations of the organic active layers, interfacial layers and devices used in this thesis, are introduced for a common polymeric BHJ solar cells. The schematic flowchart of experimental procedures of device fabrication and characterization is shown in Fig.2.1. The unique and novel features of our studied OPVs with metal oxide or metal oxide/LiF interfacial bilayer at the Al cathode, along with fabrication procedures and characterization, will be described in detail in following chapters.

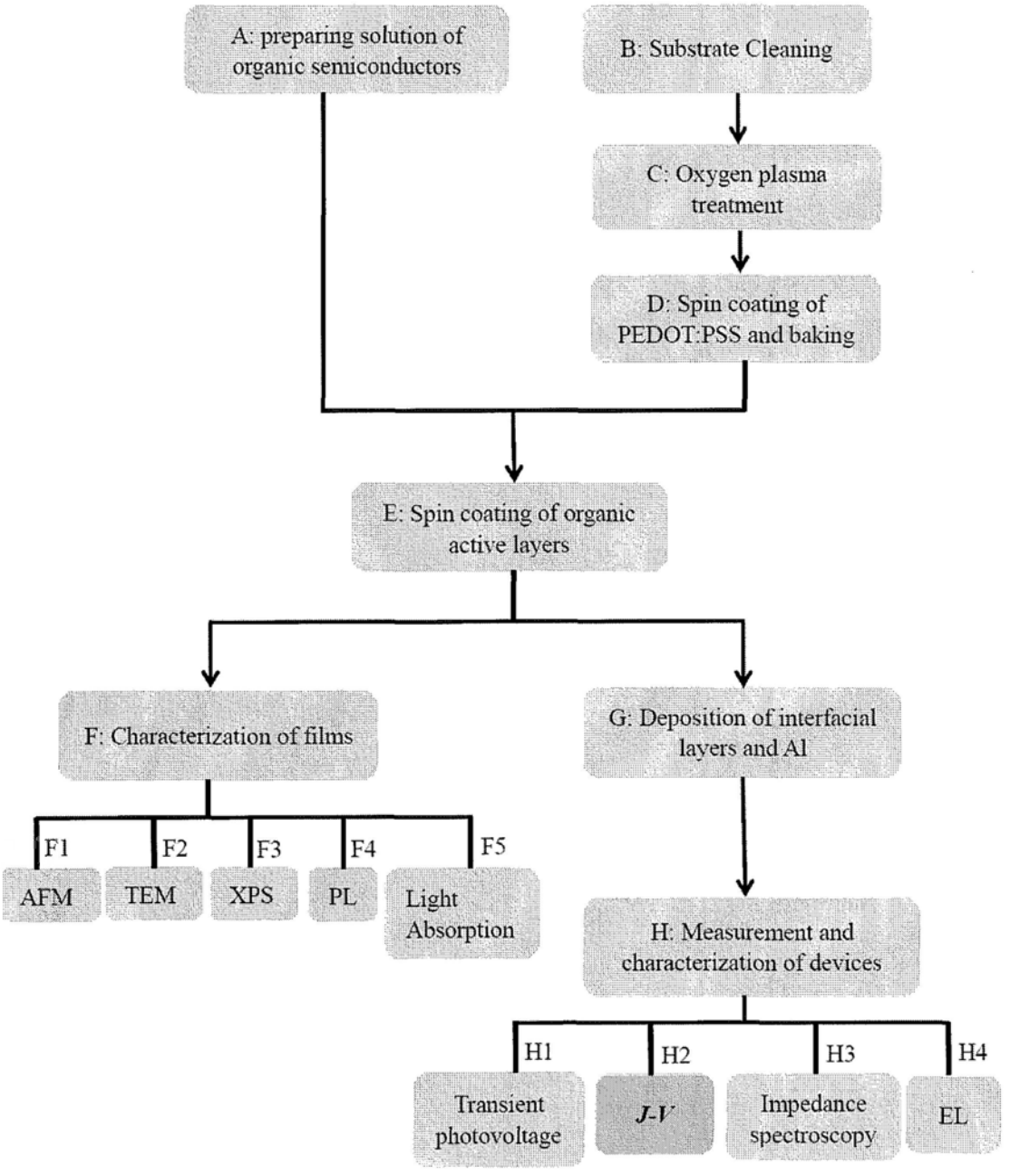

Fig.2.1 Schematic flowchart showing the experimental procedure of the organic solar cells in this thesis work, involving complementary studies of organic semiconductor films, fabrication of solar cells, and influence of interfacial layers on device performance.

2.2 Instruments and experimental methods

2.2.1 preparing solution of organic semiconductors

Firstly, a calculation for the weight of donor materials (e.g. P3HT) and acceptor materials (e.g. PCBM) as well as the volume of solvent were carefully carried out before preparing the solution. The organic materials were stored in nitrogen glove box or vacuum condition. However, they were weighted in air. Then, they were dissolved in a solvent, usually 1,2-dichlorobenzene (DCB). For instance, the mixed DCB solution had a P3HT:PCBM weight ratio of 1:1 with a concentration of 20 mg/mL. During the solvation process, the solution was properly stirred overnight in a nitrogen atmosphere so that the organic materials could fully dissolve into the solvent. It is better to firstly dissolve the donor material and acceptor material in the solvent, and then mix these solutions together according to a required ratio and pass through that solution through a 0.45 μm filter.

2.2.2 Substrate cleaning

Generally, several steps are involved in cleaning of the ITO glass substrates. Firstly, the glasses were put into deionized water under ultra-sonic condition for 20 minutes. Next, they were ultra-sonicated for 20 min in acetone, and then in 2-propanol for 20 min. After liquid cleaning, the glass substrates were dried by blowing N_2 gas with high pressure over them before the oxygen plasma treatment.

2.2.3 Oxygen plasma treatment

Oxygen plasma can be generated in different discharges, but high-frequency electrodeless discharges seem especially suitable as the entire discharge chamber is made from glass, which has a low recombination of charge [1]. In our setup, oxygen plasma is generated by microwave in vacuum (~5 Pa) with a specified oxygen flow inlet. It is believed that the active O in oxygen plasma can remove organic contamination near the ITO surface and effectively increase the workfunction of ITO, thus improving contact between the ITO and donor material (e.g. P3HT) [2]. An optimized etching time of oxygen plasma on ITO glass is ~2 min, with an O_2 flow rate of 4 sccm.

2.2.4 Spin coating of PEDOT:PSS and baking

PEDOT:PSS (Poly(3,4-ethylenedioxythiophene) poly(styrenesulfonate)) is a polymer mixture of two ionomers. One component of PSS is deprotonated by the sulfonyl groups and carries a negative charge. The other component of PEDOT is a conjugated polymer based on polythiophene, which carries positive charges. A macromolecular salt is formed by combination of these charged macromolecules. It is considered as a good hole injection or extraction layer that simultaneously blocks electrons in organic devices.

The PEDOT:PSS layer was spun using a Model KW-4A spincaster on ITO at a slow speed of 500 rpm for 5 s and a high speed of 4000 rpm for 50 s, with a thickness of about 40 nm in this thesis. And it was then annealed at 145℃ for 10 min in air. The work function of PEDOT:PSS was determined to be 5.0 eV by UPS.

2.2.5 Spin coating of an organic active layer

An organic active layer was spun onto the PEDOT:PSS layer in a glove box. The glove box is filled with nitrogen gases to create an environment with ultra-low water and oxygen contents for preparation of polymer solutions and films. The volume ratios of water and oxygen to nitrogen were no more than 10 ppm during the operation.

Generally, the organic active layers in a BHJ solar cells consist of donor and acceptor materials, deposited from one mixed solution. It should be noted that during this step, the thickness of the active layer is dependent on the concentration and viscosity of the mixed solution, surface energy of substrates, volatility of the solvent, and speed of spinning [3]. For example, a mixed solution composed of P3HT:PCBM (1:1 with a concentration of 20 mg/mL) in dichlorobenzene was spun cast onto the PEDOT:PSS layer with a slow speed of 500 rpm for 5 s and a high speed of 1200 rpm for 50 s, producing an active layer between 90-110 nm thick. The as-grown organic active layer is then annealed at 120℃ for 10 min to improve morphology of the phase separation and charge transport networks.

2.2.6 Deposition of an interfacial layer and Al

Thermal evaporation technology is used to deposit the interfacial layers (LiF, Ca) and metal electrode. The vacuum system of the thermal evaporator is composed of two pumps, a mechanical pump and a turbo pump, reaching a lowest pressure of ~3

$\times 10^{-5}$ Pa after 48 hours of pumping. There are more than four sources for metals, oxides and organic materials. The depositions of LiF, Ca, and Al were carried out in a high vacuum condition with a background pressure of around 1.2×10^{-4} Pa. The device performance is sensitive to deposition conditions, particularly the deposition rate of the interfacial layer of LiF and Ca. The deposition rates were around 0.1-0.2 Å/second for LiF, 0.4-0.6 Å/second for Ca and 2-3 Å/second for Al.

2.3 Characterization of organic films and devices

2.3.1 Atomic force microscopy (AFM)

The morphology of the thin films was observed by AFM using the tapping mode. Tapping-mode AFM has been developed as a method to achieve high resolution without inducing destructive friction forces to the sample, so it is very useful for investigating the top surface of organic films. Tapping mode AFM senses the interaction imparted to the tip from a sample surface, reading changes from its amplitude of oscillation. Before approaching a sample surface, the cantilever has a free amplitude (typically 10-100 nm) with a resonant frequency which should be measured and matched before scanning [4]. When the tip approaches the surface of the sample, the interaction force between the tip and sample changes and the amplitude of oscillation is adjusted by the piezo-driver circuit, keeping its frequency unchanged. The tip oscillation is monitored by a position-sensitive photodetector (PSD), which collects the reflected laser beam signal from the cantilever, as shown in Fig. 2.2.

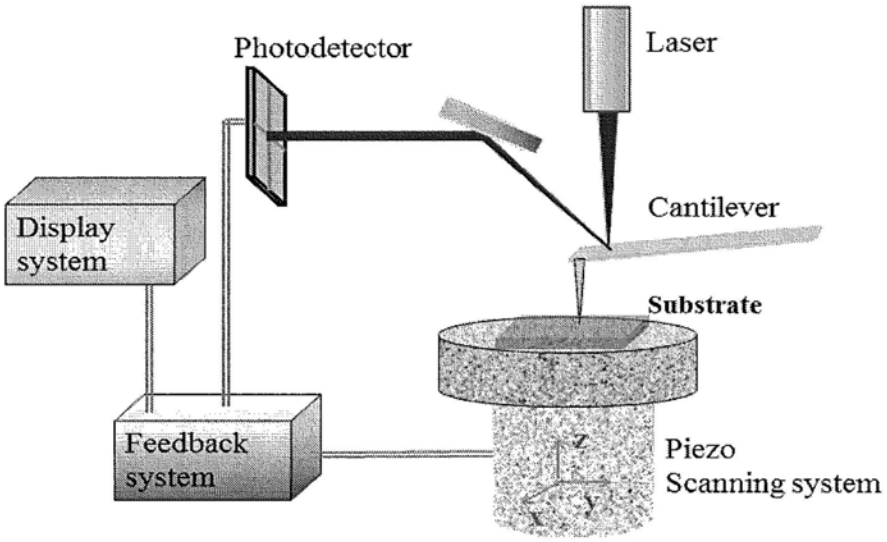

Fig.2.2 Schematic of AFM setup.

Besides observing the topographic morphology, tapping mode AFM can also do the phase imaging. A phase lag or ahead of the cantilever oscillation caused by the interaction force between the tip and sample can also be simultaneously recorded during taking images. A phase image can provide information on the distinction between different materials [5], for example between P3HT and PCBM, due to their differences in adhesion, friction, viscosity and elasticity. In this work, we use a Nanoscope II AFM.

2.3.2 X-Ray photoelectron spectroscopy (XPS)

XPS is a unique and non-destructive surface analysis technique used to determine the element compositions, chemical states, and electronic states of the elements that exist within a material. The detective depth is about 1 to 10 nm due to

the small mean length of emitted photoelectrons. The basic principle of XPS is the photoelectric effect explained by Einstein in 1905, which relies on the creation of photoelectrons via interaction between the irradiating photons and the sample. When a beam of X-ray hits the surface of a sample, locally a photon is absorbed by the inner electron in the core level of the atoms and this electron is emitted as shown in Fig.2.3. XPS spectra are obtained by simultaneously measuring the kinetic energy and corresponding number of electrons. Kinetic energy of a emitted photo-electron is defined by $E_K=hv-E_B-\phi$, where hv is the energy of a X-ray photon being used, E_B is the binding energy of electron in solid, ϕ is the work function of the spectrometer (not the material) [6]. Thus, a binding energy can be described by $E_B=hv-E_K-\phi$. The binding energy is essentially determined by the atomic orbitals where an electron is excited. Since hv and ϕ are already known in the measuring system, and the kinetic energy E_K of the emitted electrons can be measured by an energy analyzer, thus the binding energy E_B can be finally calculated. From XPS spectra, elements can be determined from peak BE (binding energy) corresponding to the electron of the characteristic atomic orbitals, while information on chemical states and binding environment can also be obtained from the shift of binding energy. XPS can identify all elements except hydrogen and helium.

A quantitative analysis of chemical compositions, e.g. the relative ratio of different atoms (x), can also be obtained from the XPS spectra. The peak area (noted as A) in XPS spectra relates a concentration of electrons with a binding energy characteristic of an element. Given the sensitivity factor (noted as S), the relative ratio

of different elements can be calculated by $x_i = \frac{A_i S_i}{\sum A_j / S_j}$. The resolution of the relative element concentration ranges from 0.1% to 1% in various elements [6].

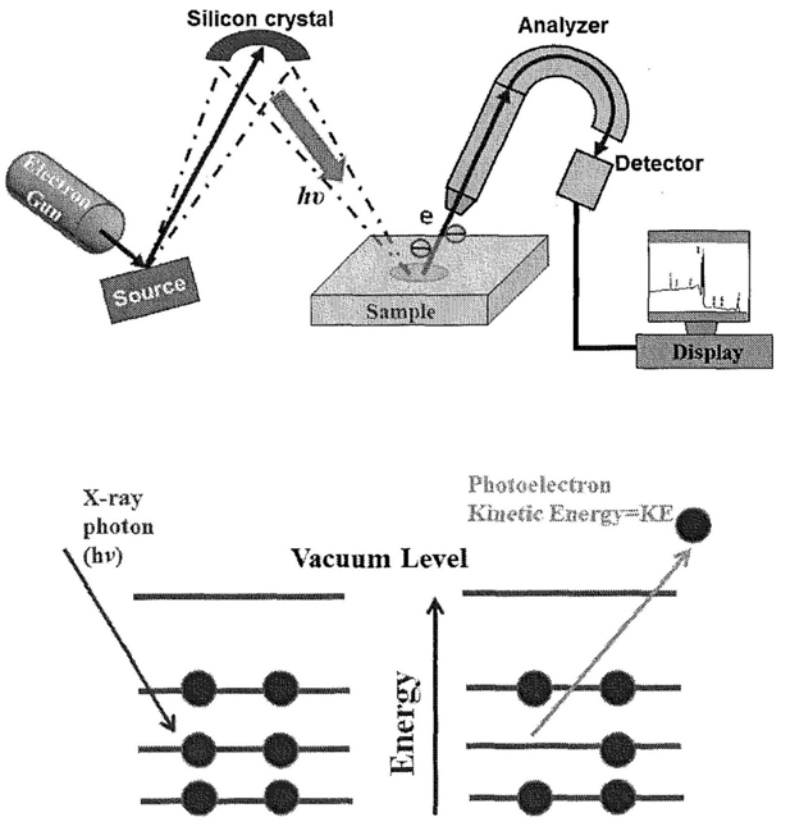

Fig.2.3 Schematic of (a) XPS and (b) energy level diagrams of a photoelectron emission process.

In this work, XPS was employed to investigate the chemical composition of metal oxides as a cathode interfacial layer, the oxidation of the Al electrode and the chemical composition ratio of donor/acceptor materials in the active layer (e.g. P3HT/PCBM). The XPS measurements were performed on a Thermo VG ESCALAB 250 X-ray photoelectron spectrometer using a monochromated Al Kα(1486.6 eV) X-ray source. The X-ray spot size was 500 μm. The XPS spectra were collected in a

constant analyzer energy (CAE) mode, at a chamber pressure of 10^{-9} mbar and pass energy of 20 eV, with a 0.05 eV/step for high-resolution scaning.

XPS depth profile is used to provide compositional information as a function of depth. XPS depth profile can be achieved by removing material from the surface of the specimen in situ by ion sputtering. XPS spectra are recorded after each Ar^+ bombardment. The Ar^+ bombardment is operated with EX05 argon ion gun at a chamber pressure of 6.5×10^{-6} Pa. The ion beam voltage is 1 kV and the emission current is 1 μA. The etching area is 2 mm×2 mm. At this condition the etch rate of SiO_2 is 0.034 nm/s.

Ultraviolet photoemission spectroscopy (UPS) has been extensively used for investigating the electronic structure of a solid. These photons are generated by a He gas discharge lamp with an energy of 21.2 eV (He I). These low energy photons are restricted to probing the valence structure of the sample. The probing depth of UPS is typically 1.5 nm. In this work, UPS analysis using a He I radiation (21.22 eV) source is performed to measure the valence states and the vacuum level positions. For the collection of secondary electrons, samples are biased at -3 V.

2.3.3 X-Ray diffraction (XRD)

XRD is a non-destructive analytical technique which can give crystallographic information. XRD is based on characterizing the scattered intensity of an X-Ray beam hitting a sample as a function of incident and scattered angle. According to Bragg's Law, the distance between different layers of atoms in an ordered structure can be

calculated from the peaks of XRD spectra. It is difficult to observe the peaks in an amorphous structure. It is thought that crystallization can improve charge transport. The XRD measurements are carried out on a Sienmens D5005 powder diffractormeter in the θ-2θ geometry, using a Cu Kα source with its wavelength of λ=1.15418 Å . The X-Ray generator works under a power of 40 kV and 40 mA. An area of X-ray beam on a sample was usually ~5 mm^2. In this work, we used XRD to determine the structure of metal oxides as the cathode interfacial layer and the order of the organic active layer.

2.3.4 Light absorption spectroscopy

Photons can be absorbed by a semiconductor material, leading to a transition of electrons from lower energy levels to higher energy levels. The light absorption coefficient can be determined by [7] $\alpha(\lambda)=\frac{1}{d}\ln(\frac{1}{T_0(\lambda)})$, where α is the light absorption coefficient, d is the thickness of the layer, and T_0 is the transmittance of light. For solar cells, it is better to absorb as much light as possible in the active layer, avoiding light absorption by the interfacial layers at electrodes. In this work, the absorption spectra of the metal oxides and organic active layer on glass and quartz substrates were collected by a UV-visible-infrared spectrophotometer (Shimadzu UV-2550).

2.3.5 Current density-voltage (*J-V*)

Electrical measurements were performed by a semiconductor characterization

system (Keithley Model 236) at room temperature in air. For photocurrent measurement, the Newport solar simulator, using AM 1.5 filter with a light power of 100 mW/cm^2 was employed. All the measurements were controlled by computer programs.

2.3.6 Impedance spectroscopy

Impedance spectroscopy is a useful tool for investigating the electrical properties of solid electronic devices, including inorganic and organic devices. The impedance spectroscopy measurements were performed by the Hewlett Packard 4284A analyzer. The sweeping frequency varies from 1 MHz to 20 Hz. There are two equivalent circuits mode in HP 4284A, parallel and series. In parallel mode, the parallel resistance has a more significant effect than that of series resistance. It is opposite in the series mode. During the measurement, different *dc* voltage (v_{dc}) can be superimposed with a modulation signal v_{ac}. The capacitance can be obtained by $C(w)=\mathrm{Im}(Y/w)$, where Y is admittance and $f=w/2\pi$. And there are two ways measuring capacitance, the capacitance-voltage (*C-V*) and capacitance-frequency (*C-f*). Traditionally, *C-V* is employed to obtain the built-in voltage of a diode and concentration of impurities [8]. *C-f* is usually performed to investigate the charge transportation and relaxation dynamics, including the mobility of carriers and their lifetime [8-9]. It is found that the recombination of electrons or holes can be monitored by *C-V* and *C-f*.

In this thesis, impedance spectroscopy is used to investigate the formation of a

charge blocking layer during the degradation of organic solar cells when exposed to air. The recombination of electrons or holes at the donor/acceptor interface and at the electrode surface was also found to have characteristics of negative capacitance.

2.3.7 Electroluminescence (EL)

EL is an optical and electrical phenomenon in which a semiconductor device emits light in response to the radiation recombination of injected electrons and holes. The EL spectra can provide the information about energy levels, particularly the charge transfer states (CTs) in solid semiconductors.

For EL measurement, we used the PL measurement system with blocking laser incident onto a sample, just to use its detector system and software. It is usually difficult to detect the EL emission from P3HT:PCBM BHJ solar cells due to its extremely weak signal. Luckily, EL emission in PFB:F8BT devices is stronger, although still very low at bias voltage around V_{oc} or bellow.

2.3.8 Transient photovoltage

It has been previously reported that the optical spectroscopy of transient photovoltage performed at the external contact is a good measurement of transient offset of a Fermi levels of electron and hole in solar cells [10-11]. As shown in Fig.2.4, the V_{oc} of a device can be adjusted by a bias light for which we used the white light. A small perturbation on V_{oc} is introduced by a flashing green LED. The flashing frequency of LED can ranges from 1 to 49 Hz. The transient photovoltage

curves are monitored at down side. By fitting an exponential decay curve to the data, the recombination rate constant can be extracted. The recombination consists of either bimolecular recombination at interfaces of the donor and acceptor, surface recombination at electrodes or trap sites in the bulk and at interfaces.

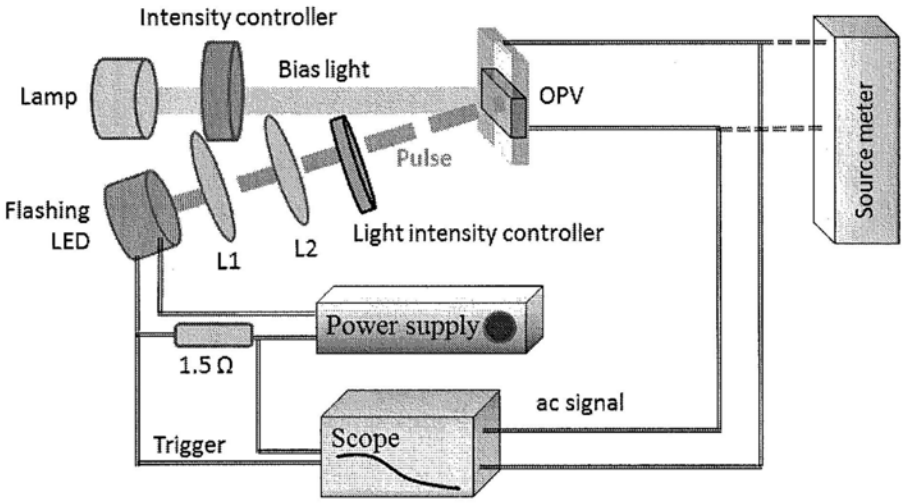

Fig.2.4 Schematic of the transient photovoltage measurement setup.

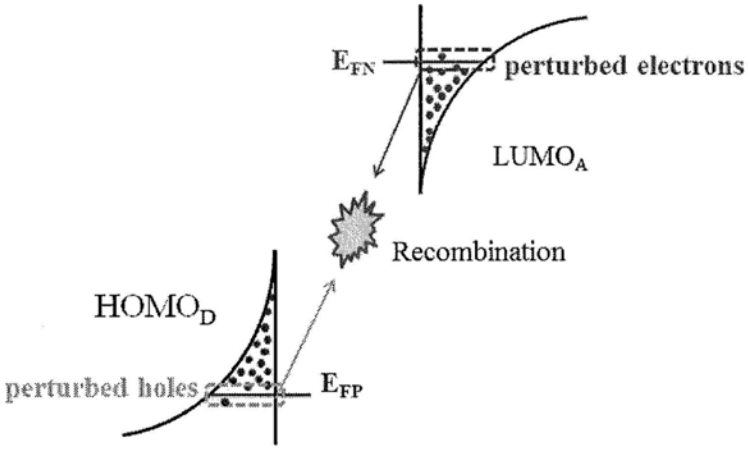

Fig.2.5 Schematic energy level diagram of donor and acceptor in the transient photovoltage measurement.

For bimolecular recombination during the measurements of transient

photovoltage as shown in Fig.2.5, the perturbed electrons from separated quasi Fermi level of electron (E_{FN}) in the acceptor material recombine with holes release from the quasi Fermi level of holes (E_{FP}) of donor material. The bias light can adjust the positions of E_{FN} and E_{FP}, such that the distance between the two Fermi levels should be equal to the value of V_{oc}. If the density of states (DOS) is exponentially distributed in both the HOMO of donor and the LUMO of acceptor material, the bimolecular recombination should be dependent on the distance between E_{FN} and E_{FP}, and thus greatly decrease with decreasing V_{oc} by changing the intensity of the bias light.

The positions of $HOMO_D$ and $LUMO_A$ fundamentally determine the value of V_{oc} in donor/acceptor organic solar cells. However, the surface recombination at the cathode will in advance reduce the V_{oc}, which can be eliminated by modification at the cathode. We use the transient photovoltage technology to find the first order of recombination at bulk interfaces or the cathode interface in organic solar cells with different cathode interfacial layers.

2.4 Summary for Chapter 2

The main instruments, procedures of fabrication, and characterization techniques for organic solar cells are introduced in this chapter.

Reference

[1] A. Vesel, M. Mozetic and M. Balat-Pichelin, Vacuum 81, 1088 (2007).

[2] J. Xue, and S. R Forrest, J. Appl. Phys. 95 1869 (2004).

[3] S. Middleman and A. K. Hochberg, Process Engineering Analysis in Semiconductor Device Fabrication, McGraw-Hill (1993).

[4] Veeco, DI 3100 operation Manual.

[5] B. T. de Villers, C. J. Tassone, S. H. Tolbert, and B. J. Schwartz, J. Phys. Chem. C 113, 18978 (2009).

[6] J. F. Moulder, W. F. Sticle, P. E. Sobol, K. D. Bomben, Handbook of X-ray Photoelectron spectroscopy, Physical Electronics Inc (1992).

[7] M. D. Wang, D. Y. Zhu, Y. Liu, L. Zhang, C. H. Zheng, Z. H. He, D. H. Chen, L. S. Wen, Chin. Phys. Lett. 25, 743 (2008).

[8] J. R. Macdonald, Impedance Spectroscopy, John Wiley and Sons, New York, (1987).

[9] S. W. Tsang, S. K. So, and J. B. Xu, J. Appl. Phys. 99, 013706 (2006).

[10] B. C. O'Regan, S. Scully, A. C. Mayer, E. Palomares and J. Durrant, J. Phys. Chem. B 109, 4616 (2005).

[11] I. Mora-Sero´, T. Dittrich, A. Belaidi, G. Garcia-Belmonte, and Juan Bisquert, J. Phys. Chem. B 109, 14932 (2005).

Chapter 3

Performance and stability improvement in P3HT:PCBM BHJ solar cells by chromium oxide (CrO_x)

3.1 Overview

In this chapter, we focus on the thermally evaporated chromium oxide (CrO_x) as a cathode interfacial layer to improve the efficiency and air stability of P3HT:PCBM BHJ solar cells. Devices with a CrO_x interfacial layer show an improved stability more than 100 times better than that of devices without any interfacial layer or with LiL interfacial layer. The mechanisms for the Al/organic cathode interface degradation and the improvement by CrO_x are proposed and discussed.

3.2 Introduction

Recent progress in polymeric solar cells has led to power conversion efficiencies (PCEs) of 6~8% [1-3]. In organic solar cells, the organic active layer usually has a thickness of around 100 nm because of its poor electric conductivity. Electrode engineering is a key strategy for improving the performance through optimization of the short circuit current (J_{sc}), open circuit voltage (V_{oc}), fill factor (FF), and stability [4-7].

The metal-organic interface plays an essential role in determining the overall device performance in organic solar cells, and inserting a functional interfacial layer can effectively change the interface properties, thus effectively improve the device

performance. The main functions of the interfacial layers are:

(1) Improvement of charge selectivity at the electrodes

(2) Reduction of diffusion and reaction between the electrode materials and polymer

(3) Enhancement of optical absorption as an optical spacer

(4) Modification of the surface properties to alter film morphology

The cathode interface is crucial for the device performance. It is preferable for the cathode electrode to have a low workfunction contact for efficient electron extraction. Al is the most commonly used electrode material in solar cells, which is generally deposited by thermal evaporation, although this process frequently alters the quality of the metal/organic interface, because the hot metal atoms may react with oxygen species remaining in the vacuum chamber, and diffuse into the organic active layer. It is suggested that the instability of the Al electrode is related to Al-C bond formation, which interrupts the π-conjugation systems [8-9].

In previous decades, extensive efforts have been devoted to OLED research and a variety of functional interfacial materials have been developed. Many of the interfacial materials used for OLEDs have been successfully transferred to engineer interfaces for organic solar cells. Alkali metal compounds, including LiF and Cs_2CO_3, typically provide low workfunction contacts. They are commonly used an electron injection layer in OLEDs, and have also found success in polymer solar cells [10-12]. Although it is reported that Al deposition decomposes LiF, causing Li-doping of the organic material to yield a low workfunction for (sub)monolayer coverage while

thicker LiF creates a dipole layer that downshifts the workfunction [13, 14]. Hovever, the detailed mechanisms behind improving efficiency with a LiF interfacial layer are still under debate.

The low workfunction metals Ca, Mg, and Ba have also been used as cathode interfacial layers to improve device performance, forming an ohmic contact that reduces series resistance, and thus increases FF. It is thought that a thin n-doped layer induced by Ca deposition pins the surface energy level at the polymer/Al interface, facilitating the electron extraction [15]. But low workfunction metals themselves are usually unstable in air and easily oxidized to form a thicker insulator layer at the interface, which causes the device to degrade rapidly. Transparent metal oxide semiconductors such as TiO_2 and ZnO are commonly employed as interfacial layer to improve the performance and stability of organic solar cells [16-20]. It has been suggested that using the inverted structure with ZnO and TiO_2 can improve device stability by avoiding the anode degradation between ITO and acidic PEDOT:PSS [17, 18]. Although a number of studies have been carried out and progress has been made, the degradation issue is rather complicated and certainly not yet fully understood. It is important to develop new strategies that improve device stability and are compatible with device flexibility and ease of fabrication, while continuing to work towards understanding the degradation mechanisms.

In this chapter, we will demonstrated that incorporation of a thermally evaporated CrO_x layer can improve performance and air stability of P3HT:PCBM BHJ solar cells with Al cathode. Mechanisms for the rapid degradation in devices without any

interfacial layer and stability improvement by including a CrO_x interfacial layer between the organic active layer and Al cathode in P3HT:PCBM solar cells will be discussed.

3.3 Experimental details

Device fabrication consisted of the following steps. Firstly, ITO glass was cleaned, and then treated with oxygen plasma. Secondly, the PEDOT:PSS was spin-cast on ITO glass with a thickness of ca. 40 nm, and then annealed at 145 °C for 10 min in air. A mixed solution composed of P3HT and PCBM in dichlorobenzene was spin-cast on the top of the PEDOT:PSS layer at a slow speed of 500 rpm for 5 seconds and a high speed of 1200 rpm for 50 seconds, producing an organic active layer about t 90-110 nm thick that was then annealed at 120 °C for 10 min in nitrogen atmosphere. The mixed solution had a P3HT:PCBM weight ratio of 1:1 with a concentration of 20 mg/mL. A 90 nm-thick film of Al was thermally evaporated onto the top of the device. Before evacuation, the chamber was exposed to air for several minutes, without intentional oxygen doping. The active area of device was 1×2 mm for all devices with interfacial layers such as LiF and CrO_x. And the devices without interfacial layer (the active areas 1×2 mm, 2×3 mm, 3×4 mm, and 8×10 mm) were fabricated to determine the area dependent degradation. The devices with LiF as interfacial layer (ITO/PEDOT:PSS/P3HT:PCBM/LiF/Al, with 1 nm-thick LiF), with bilayer LiF and CrO_x as interfacial layer (ITO/PEDOT:PSS/P3HT:PCBM/LiF/CrO_x/Al, with 0.8 nm-thick LiF 4.2 nm-thick CrO_x and ITO/PEDOT:PSS/P3HT:PCBM/CrO_x/LiF/Al),

and without interfacial layer (ITO/PEDOT:PSS/P3HT:PCBM/Al) were also fabricated and tested under the same conditions. For all devices, no external package or encapsulation was applied after device fabrication.

The thin CrO_x layer (ca.5 nm) was deposited by thermal evaporation of chromium metal under a low vacuum (from 1.2×10^{-2} to 5×10^{-3} Pa), where some oxygen still remain inside the chamber to react with Cr atoms to form Cr_2O_3. However it is not easy to control the oxidation of Cr to be Cr_2O_3 in this process. Cr is finally formed into partially oxidized chromium oxide, noted as CrO_x, with some Cr metal species remaining in the Cr_2O_3. For control devices with Cr, the Cr interfacial layer is evaporated from a Cr metal under high vacuum (1.5×10^{-4} Pa) condition. For devices with Cr_2O_3, the Cr_2O_3 interfacial layer was deposited by thermal evaporation of Cr_2O_3 powder under high vacuum (1.2×10^{-4} Pa) condition.

Electrical measurements were conducted by a semiconductor characterization system (Keithley 236) at room temperature in air under the spectral output from solar simulator (Newport) using an AM 1.5G filter with a light power of 100 mW/cm^2. The light intensity is precisely calibrated by a standard solar cell. For all devices, no external package or encapsulation was applied after device fabrication. The capacitance measurements were performed with Hewlett Packard 4284A impedance analyzer. The fixed frequency to measure capacitance-voltage is 1kHz.

3.4 Properties of a CrO_x film

3.4.1 XRD of CrO_x

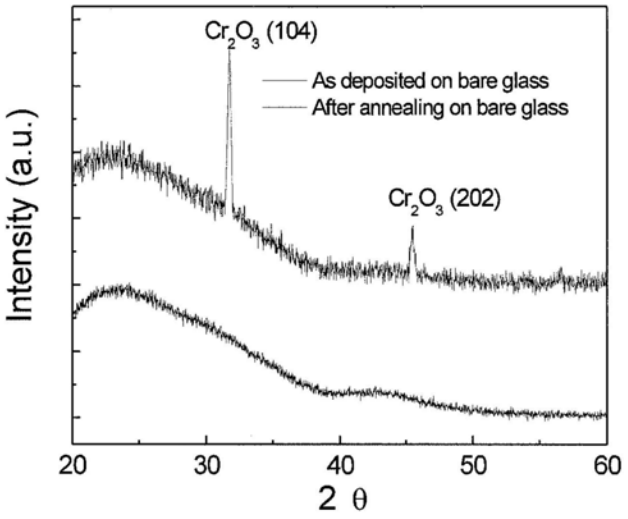

Fig.3.1 XRD patterns of the CrO_x films as grown and annealed at 450℃ in air.

To investigate the structure of thermally evaporated CrO_x, 20 nm-thick CrO_x films were deposited on bare glass. XRD patterns of the CrO_x films are shown in Fig.3.1. The as-grown CrO_x film exhibits amorphous property. It is common to deposit amorphous films by thermal evaporation because the evaporated atoms usually have lower kinetic energy compared to those from other deposition methods such as e-beam, sputter, MOCVD etc. [21]. Since there is not enough energy for evaporated atoms or molecules to mobile and re-order on the substrate, thus amorphous structures are formed. A broad peak in the XRD spectra between 20° and 30° is due to the substrate of amorphous glass. Two peaks are observed in the films annealed at 450℃ for half an hour in air, which indicates the crystallization of chromium oxide in film. The peak around 32° is attributed to Cr_2O_3 (104), and the one round 45° to Cr_2O_3 (202) [22].

3.4.2 Optical properties of CrO_x

In organic solar cells, non-effective absorption should be avoided within their functional interfacial layers. Cr_2O_3 is a compound semiconductor, with a bandgap of 3.3 eV [23], which indicates a good optical transmittance property of a buffer layer for solar cells. UV-visible absorption spectra of CrO_x thin film are shown in Fig.3.2. For 5 nm thick CrO_x, the transmittance in the visible region is high, although there is little absorption after the wavelength of 500 nm, possibly caused by the metal species in the film. Obviously, absorption increases with the film thickness.

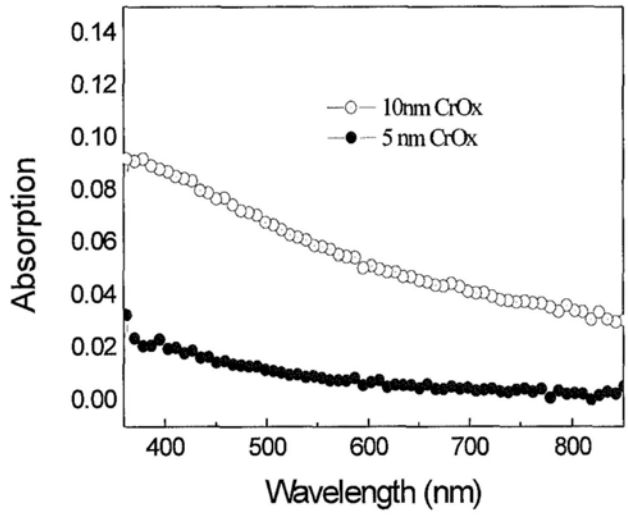

Fig.3.2 Absorption spectra of CrO_x thin films.

3.4.3 Electrical properties of CrO_x

Mobility of CrO_x is measured by the Van der Pauw 4-probe method [24], which is commonly used to measure the resistivity, mobility, carrier concentration and Hall coefficient, particularly for inorganic semiconductor thin films. There are no requirements for the size and shape of the measued films, however, all four electrodes

should be placed at the edge of the film. A 20 nm-thick CrO_x thin film was firstly deposited on a bare glass substrate, then the glass was cut into 0.5 cm×0.5 cm square, four Al electrodes were deposited at the edge of the CrO_x film. The mobility was obtained from the majority carrier mobility in terms of the calculated sheet resistivity and Hall coefficient $\mu = \frac{|R_H|}{\rho}$ [24]. The thermally evaporated chromium oxide (CrO_x) was determined to be n-type with a mobility of 0.14 $cm^2/V \cdot s$, using the Hall System HL5500 measurement system. This value is much higher than that of TiO_x ($\sim 10^{-4}$ $cm^2/V \cdot s$) [16]. It is assumed that a interfacial layer with higher mobility is good for charge transport.

3.5 Performance and stablity improvement of P3HT:PCBM solar cells by CrO_x

3.5.1 Performance improvement by CrO_x

3.5.1.1 *J-V* characterisitcs

We tried using CrO_x as a cathode interfacial layer to improve the device efficiency. The device structure is shown in Fig.3.3, with different functional layers. While the *J-V* characteristics under illumination are shown in Fig.3.4. Devices without any interfacial layer between the polymer and Al (denoted as "Al only") (ITO/PEDOT:PSS/P3HT:PCBM/Al) exhibited an initial efficiency as high as 1.5% with V_{oc}=0.4 V, J_{sc}=8.55 mA/cm^2, and FF=0.43. It is well known that the quality of P3HT and PCBM, and the fine control of the phase separation in P3HT:PCBM blend are crucial for the device performance. This is the reason why a wide range of PCE

values were reported from different groups among the same material system [15, 25-26]. The values in our P3HT:PCBM solar cells are reasonable compared to values reported by others [25-26]. By comparison, it is found that device performance is significantly improved by including the interfacial layer of either LiF or CrO_x. Devices with LiF (ITO/PEDOT:PSS/P3HT:PCBM/LiF/Al) had a PCE of 3.5% with V_{oc}=0.59 V, J_{sc}=10.08 mA/cm^2, and FF=0.59. Device with CrO_x (ITO/PEDOT:PSS/P3HT:PCBM/CrO_x/Al) exhibited a PCE as high as 3.9%, with V_{oc}=0.58V, J_{sc}=11.15 mA/cm^2, and FF=0.61. In our experiment, the optimized performance was achieved in devices with a 5 nm thick CrO_x film as cathode interfacial layer. We also test 2 nm-thick and 10 nm thick CrO_x, which performed at 2.7% and 3.2% efficiency, respectively. In addition to the comparable efficiency improvement, devices with CrO_x show a dramatic improvement in stability, in comparison to those with a LiF interfacial layer. The detailed efficiencies, J_{sc}, V_{oc} and FF are listed in Table 3.1.

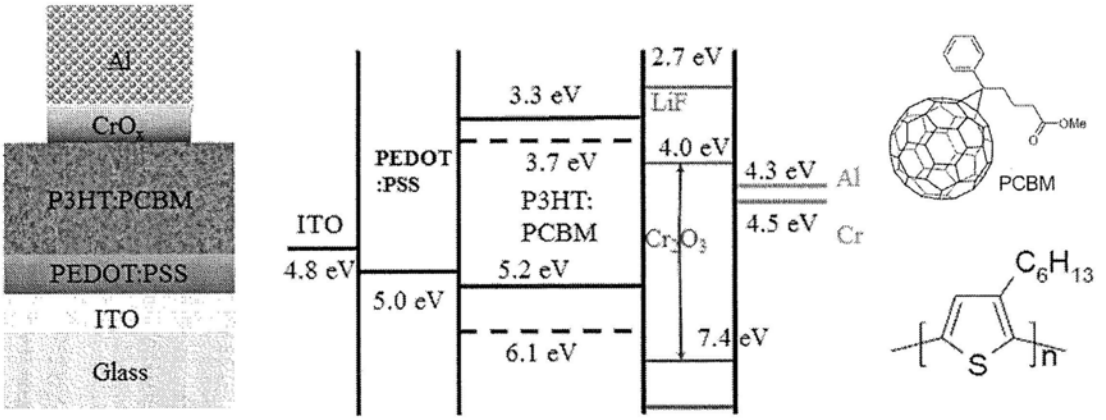

Fig.3.3 (a) Photovoltaic device structure, (b) energy-band diagram composed of different organic layers and interfacial layers.

Table 3.1 Initial parameters of P3HT:PCBM BHJ solar cells with interfacial layers

Sample	Efficiency	V_{oc}(V)	J_{sc} (mA/cm^2)	FF
Al only	1.5%	0.40	8.55	0.43
With LiF	3.5%	0.59	10.08	0.59
With CrO_x (2 nm)	2.7%	0.50	10.75	0.50
With CrO_x (5 nm)	3.9%	0.58	11.15	0.61
With CrO_x (10 nm)	3.2%	0.56	11.80	0.48

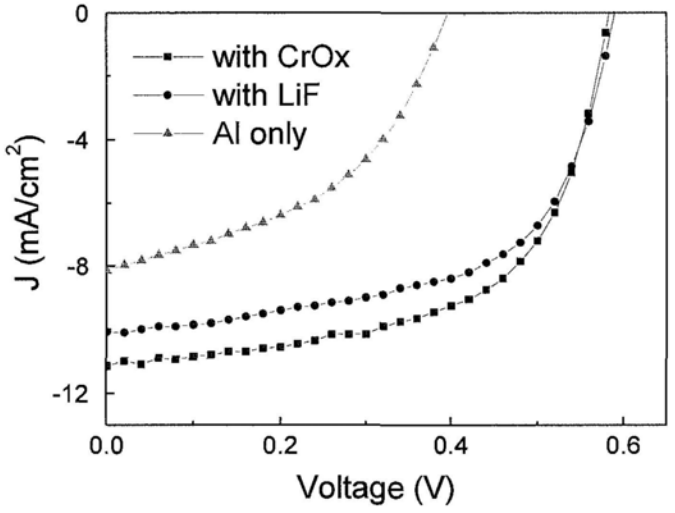

Fig.3.4 *J-V* characteristics of P3HT:PCBM BHJ solar cells with the different cathode interfacial layers under illumination.

During the deposition of electrode, Al is very easily oxidized, so the deposition pressure is crucial. A layer containing Al_2O_3, an insulator used as a dielectric layer in field effect transistor, is often formed during this process, which may lead to a higher contact resistance and lower FF. However, Cr_2O_3, an oxidation product of chromium, is an n-type semiconductor with a mobility of 0.14 cm^2/V·s, which is sufficient to facilitate electron transport in organic solar cells. Moreover, Cr_2O_3 is a very stable

semiconductor [27], with its conduction band minimum of 4.0 eV [23], just between the work function of Al and LUMO of PCBM (shown in Fig.3.3(b)), which renders it an efficient electron transport material. On other hand, its large band gap of 3.4 eV [23] is also capable of blocking the holes and excitons efficiently. In addition, the chromium oxide layer serves as an optical spacer to redistribute light intensity in the active layer, thereby increasing the short circuit current as previously reported for TiO_x [16]. As expected, a low work function material, small LUMO, or small conduction band minimum of the cathode interfacial layers can improve V_{oc}. Cr_2O_3 has a slightly lower conduction band minimum (shown in Fig.3.3) than that of Al, so inserting a CrO_x layer is very likely to result in a higher V_{oc}.

3.5.1.2 Chemical composition of CrO_x

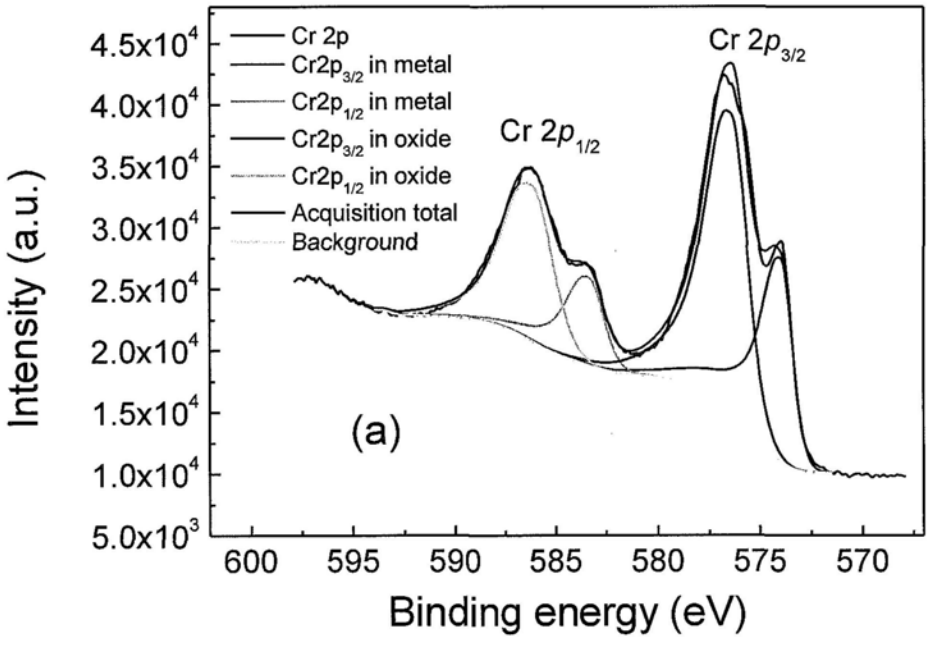

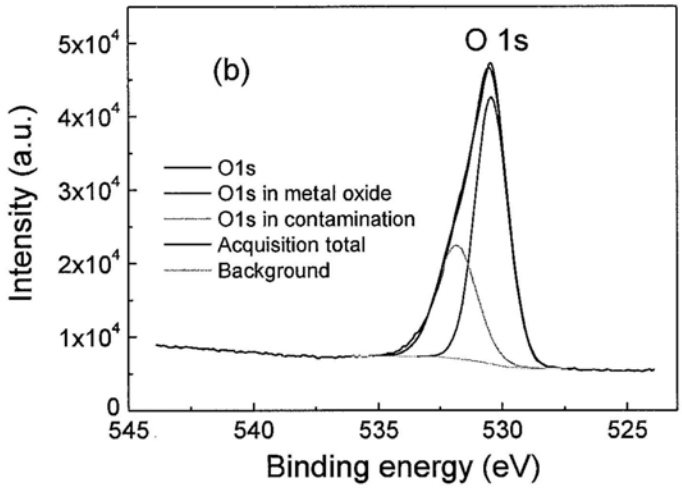

Fig.3.5 Fitted core level XPS spectra of (a) Cr 2*p* peaks, and (b) O 1*s* peak of the as-deposited CrO_x films on P3HT:PCBM.

To collect the compositional information of CrO_x, XPS analysis was performed. XPS spectra are shown in Fig.3.5. The Gaussian-Lorenztzian modeling is used to analyze the XPS data so as to obtain the element ratio and exact positions of peaks. In Fig.3.5 (a), the peak at 573.99 eV corresponds to Cr $2p_{3/2}$ of metallic chromium [28], while the peak at 583.37 eV to Cr $2p_{1/2}$ of metallic chromium. And the peak at 576.42 eV relates to Cr $2p_{3/2}$ of chromium oxide (Cr_2O_3) [28-30] while the peak at 586.21 to Cr $2p_{1/2}$ of chromium oxide. The O 1*s* spectrum (Fig.3.5.(b)) is composed of two peaks. The peak at a binding energy of 530.41 eV corresponds to O in Cr_2O_3 [30-32], and the other peak at binding energy of 531.82 eV is attributed to contamination. The XPS study reveals that the film is oxygen-deficient Cr_2O_3 films enriched with metallic Cr to form CrO_x (x being around ~1.2-1.4, slightly lower than that of Cr_2O_3 (1:1.5)). It is well known that Cr metal is easily oxidized. During thermal evaporation under a low vacuum (the base pressure around 10^{-2} Pa), some residual oxygen species still

exist in the chamber, and hot chromium atoms are perceived to react with them to form CrO_x. Along with the deposition process, the oxygen species should decrease. It is plausibly speculated that a perfect CrO_x layer should be Cr_2O_3 in the close proximity of organic-Cr-oxide interface to block holes, and facilitate electron transport by tunneling. The successive part will be oxygen-deficient with some metallic Cr species for electron collection. With the control of deposition pressure and rate, oxygen content in CrO_x can be manipulated, resulting in varied optical and electric properties of CrO_x.

3.5.1.3 Morphology of CrO_x

Fig.3.6 shows the AFM topography and phase images of P3HT:PCBM blend thin films before (Fig.3.6 (a) and (b)) and after deposition of LiF (Fig.3.6 (c) and (d)) and CrO_x (Fig.3.6 (e) and (f)). No grains or particles are observed on the pristine P3HT:PCBM surface. As shown in AFM images, the surfaces after deposition of LiF present particles (presumably LiF aggregates) which do not cover the entire surface of the polymeric blend. Both morphology and phase images indicate that the CrO_x layer consists of 30 nm size particles in diameter that fully cover the polymer surface. This fully covered CrO_x layer should reduce direct contact between the organic materials and Al.

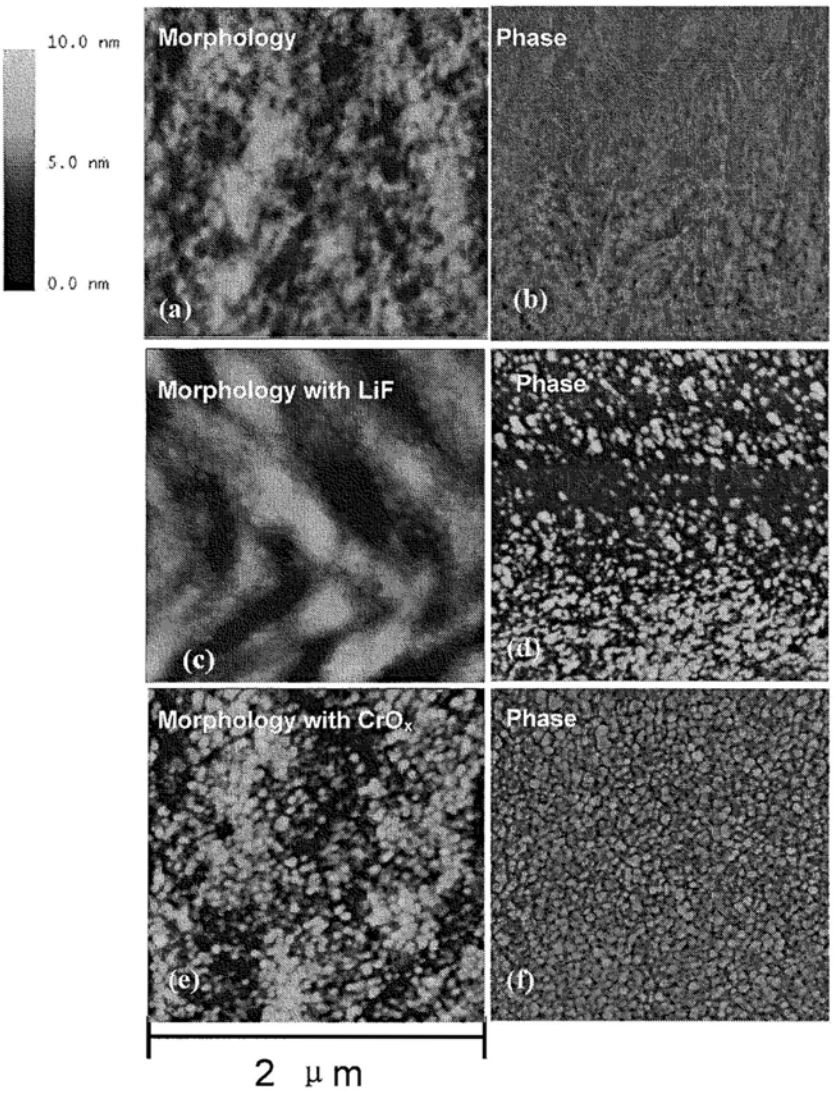

Fig.3.6 The AFM images of P3HT:PCBM (ITO/PEDOT:PSS/P3HT:PCBM) (a) morphology and (b) phase; with LiF on P3HT:PCBM (ITO/PEDOT:PSS/ P3HT:PCBM/LiF) (c) morphology and (d) phase; with CrO_x (ITO/PEDOT:PSS /P3HT:PCBM/CrO_x) (e) morphology and (f) phase.

Particles of CrO_x over 30 nm in diameter were formed on the organic active layer, as shown in Fig.3.7(a). This is surprising because the CrO_x layer was on averaged only 5 nm thick, as read out from the thickness monitor and calibrated by AFM. One possibility for this is that the substrate was not perfectly smooth, that could affect the

CrO_x growth. Another more likely possibility stems from the idea that surface energy plays an important role in affecting CrO_x film growth. It is speculated that the surface energy of P3HT:PCBM affected the over layer growth of CrO_x, which formed non-sphere aggregates on the organic active layer as shown in Fig.3.7 (c) [31]. In this way, CrO_x aggregates larger than 30 nm in diameter could be formed within 5 nm thick films. Similarly, it was also observed that particles of LiF greater than 10 nm in diameter could form within 1 nm thick films.

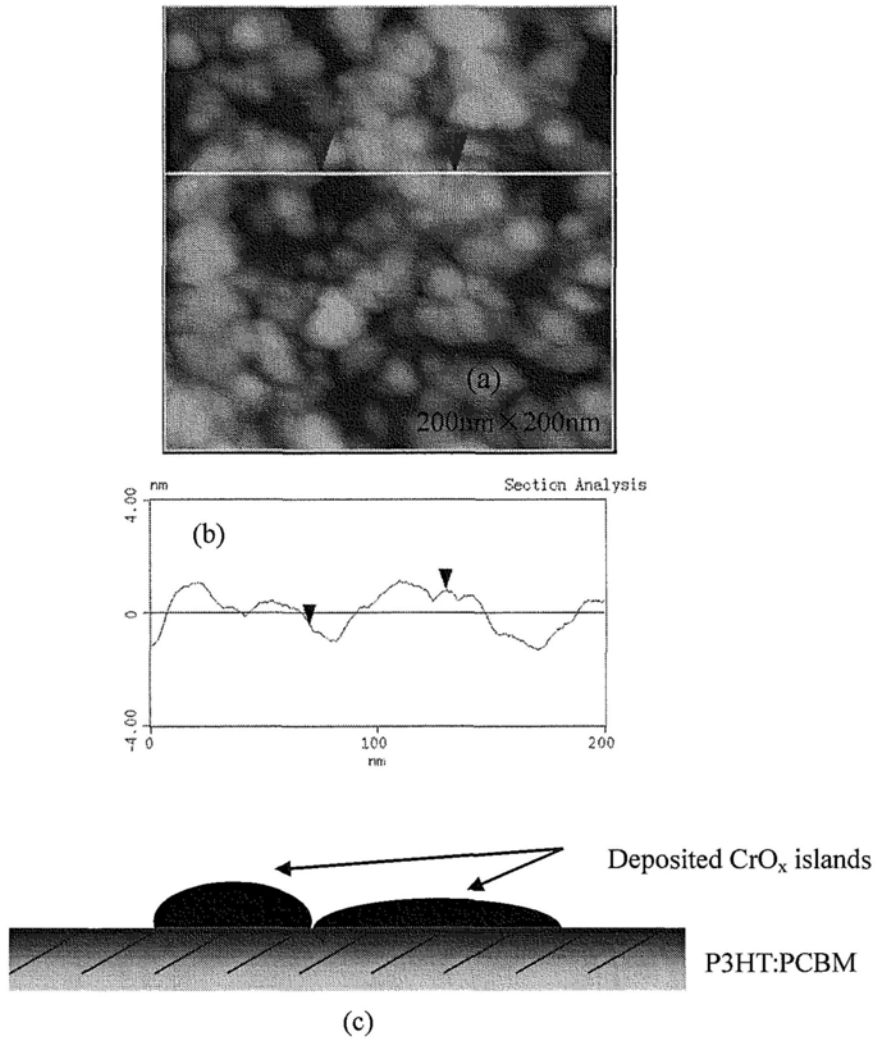

Fig.3.7 (a) AFM image of CrO_x on P3HT:PCBM, (b) cross-section line profile of the CrO_x film, and (c) the growth model of CrO_x on the organic active layer.

3.5.2 Stability improvement by CrO_x

Stability is another important issue for polymeric solar cells [32-34]. Here our experiments have shown that the thermally evaporated CrO_x layer indeed improves the lifetime of P3HT:PCBM BHJ solar cells in air. Fig.3.8 shows the comparison of efficiency versus storage time of the solar cells with a CrO_x layer, LiF layer, and without any interfacial layer (Al only). For all devices, no extra package or encapsulation was used. For devices with a LiF interfacial layer and without the interfacial layer stored in ambient air, dramatic decreases of PCE were observed as the storage time increased, and they lost 90% of their initial efficiencies after 5 hours, mainly due to the loss of photocurrent. However, for devices with a CrO_x interfacial layer, almost no decrease in the first several hours was observed. The devices still remained nearly 50% of the initial PCE after 6 days, and 35% after 12 days.

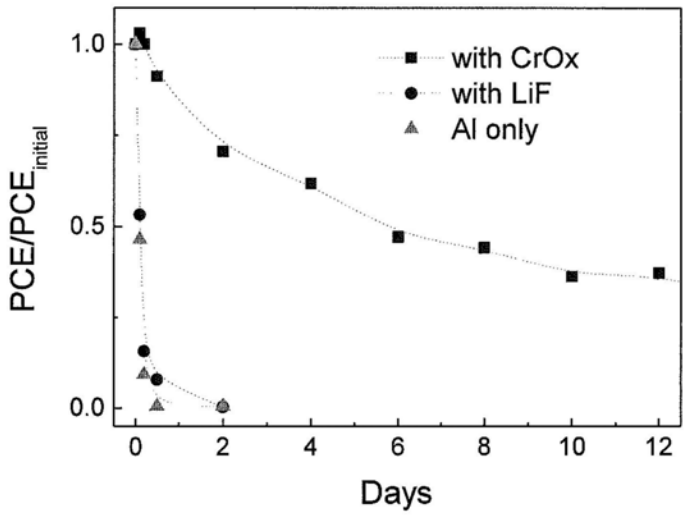

Fig.3.8 Comparison of the power conversion efficiencies as a function of storage time for P3HT:PCBM BHJ solar cells with the interfacial layers of CrO_x, LiF, and without the interfacial layer (Al only). Note that the device characteristics are monitored with increasing storage time for the same devices.

Based on the experimental results above, it can be deduced that the CrO_x layer plays a key role in retarding degradation. Theoretically, Lögdlund et. al. [7] proposed a direct reaction for the formation of Al-C bonds with high reductive power due to Al. An alternative to Al-C bonding is single-electron transfer with the creation of anion radicals on the polymer [7, 35]. Both organo-aluminum compounds and anion radicals are highly reactive species that can react with any proton donors present, such as water, or oxygen. Besides, it is reported that oxygen and water can diffuse through the aluminum electrode via microscopic pinholes and grain boundaries to the organic-Al interface and the active layer, resulting into degradation [36, 35]. On other hand, it is suggested that TiO_x layer functions as a robust diffusion barrier against oxygen and water into the organic active layer because of its scavenging effects due to photocatalysis and oxygen deficiency, leading the improved stability.

However, we attribute the rapid degradation in devices to the instability of the thick organic-aluminum interfacial layer in air, at least 5 nm thick as reported [37]. And CrO_x can avoid or minimize the formation of this thick interfacial layer. Our detailed mechanisms for the degradation and stability improvement will be fully discussed in part of 3.6.

3.5.3 Influence of chemical composition (Cr, CrO_x, Cr_2O_3)

As shown in Table 3.2, devices with a Cr_2O_3 interfacial layer produced by thermal evaporation of Cr_2O_3 powder have lower performance than those with CrO_x.

So do the devices with a Cr interfacial layer formed by thermally evaporating Cr under high vacuum. The devices with a Cr interfacial layer have poor performance with lower V_{oc}, while devices with a Cr_2O_3 interfacial layer have higher V_{oc} but relatively low PCE, which is attributed to the relatively low electron transport properties of amorphous Cr_2O_3 by thermal evaporation. Cr_2O_3 plays an important role in improving the V_{oc} due to its desired energy levels, while metallic Cr has good electronic properties. The CrO_x has the desired properties of both effectively blocking holes and still facilitating electron transport. It is plausibly speculated that an anticipated CrO_x layer would have the Cr_2O_3 in the vicinity of organic-chromium-oxide interface for blocking holes while facilitating electron tunneling and transport, and the successive part would be oxygen deficient with some metallic Cr species for electron transport. The chemical composition of the interfacial layer also alters the stability of device as shown in Fig.3.9. It is assumed that the Cr_2O_3, not the metal Cr, improve device stability. The poorer stability of device with Cr_2O_3 may partially result from the poorer quality of the film by thermal evaporation of Cr_2O_3 powder, because of its high melting point of 2435℃.

Table 3.2 Parameters of P3HT:PCBM BHJ solar cells with a cathode interfacial layer of CrO_x, Cr_2O_3 and Cr.

Sample	Efficiency	V_{oc}(V)	J_{sc} (mA/cm^2)	FF
With CrO_x	3.9%	0.58	11.15	0.61
With Cr_2O_3	2.8%	0.58	10.0	0.48
With Cr	2.2%	0.46	9.9	0.48

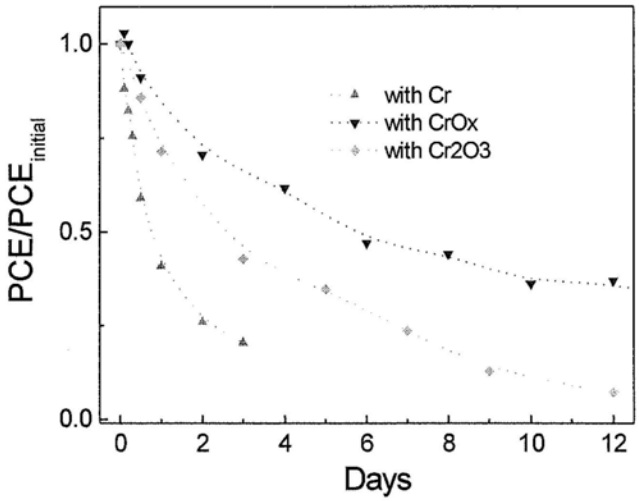

Fig.3.9 Comparison of the PCEs as a function of storage time for P3HT:PCBM BHJ solar cells with an interfacial layer of CrO_x, Cr_2O_3 and Cr. Note that the device characteristics are monitored with increasing storage time for the same devices.

3.6 Degradation mechanism

3.6.1 Degradation of device performance in air

There are several mechanisms leading to the degradation of OPV. Our above results have clearly demonstrated that the degradation at the organic/Al contact plays a dominant role in the overall device degradation in air. The structure of the photovoltaic devices investigated in this study is also shown in Fig.3.3. These devices were characterized under AM 1.5, 100 mW/cm^2 illumination and the *J-V* characteristics with storage time in air are shown in Fig.3.10. For all the devices, no packaging or encapsulation was used. Importantly, the aim of this work is to underline the degradation mechanism and propose approaches to prevent this process. Upon air exposure, the J_{sc} of these devices Al only decreased dramatically, while the V_{oc} remained almost unchanged. The overall PCE dropped by 90% after 5~6 hours of air

exposure. The devices with LiF a interfacial layer exhibited an initial PCE as high as 3.5 %. A dramatic decrease of PCE was also observed, losing over 75% of the initial PCE after ~5 hours and over 95% after 1 day in air. Devices with CrO_x layer (ITO/PEDOT:PSS/P3HT:PCBM/CrO_x/Al) exhibited a PCE as high as 3.9%. For these devices, almost no decrease of PCE was observed in the first several hours after air exposure. It preserved nearly 90% of the initial PCE after 1-day storage in air and ~50% after a week.

To check if the rapid degradation of the devices without CrO_x interfacial layer was due to the degradation of organic active materials or the anode interfaces, the substrates with an organic active layer (ITO/PEDOT:PSS/P3HT:PCBM) were first exposed to air for 1~2 days. LiF and Al layers were then deposited, immediately followed by device characterization. In this case the devices still had high initial PCE, as shown in Fig.3.10 (d). We also repeated the same experiment but changed the air exposure time to 3 months, and we were still able to obtain an initial PCE of 1% after LiF and Al deposition. The degradation of multiple layers without a cathode layer was a rather slow process. These results suggest that the rapid failure of devices is due to degradation at the polymer/cathode interface, rather than the degradation of the organic active layer itself or the anode interface. By contrast, it has been demonstrated that the degradation of OLED and PLED is due to the anode interface of PEDOT:PSS rather than to the cathode interface [38]. It may result from the different work condition of high bias voltages used in OLED, which allows charges to tunnel through the cathode much more easily, despite the formation of a thin barrier at the cathode.

We agree that the degradation of the bottom interface is an important process and that a more detailed study is needed to monitor this process under electrical testing condition in air. We, however, emphasize that we have clearly shown that the cathode interface dominates the initial fast degradation of P3HT:PCBM solar cells in air.

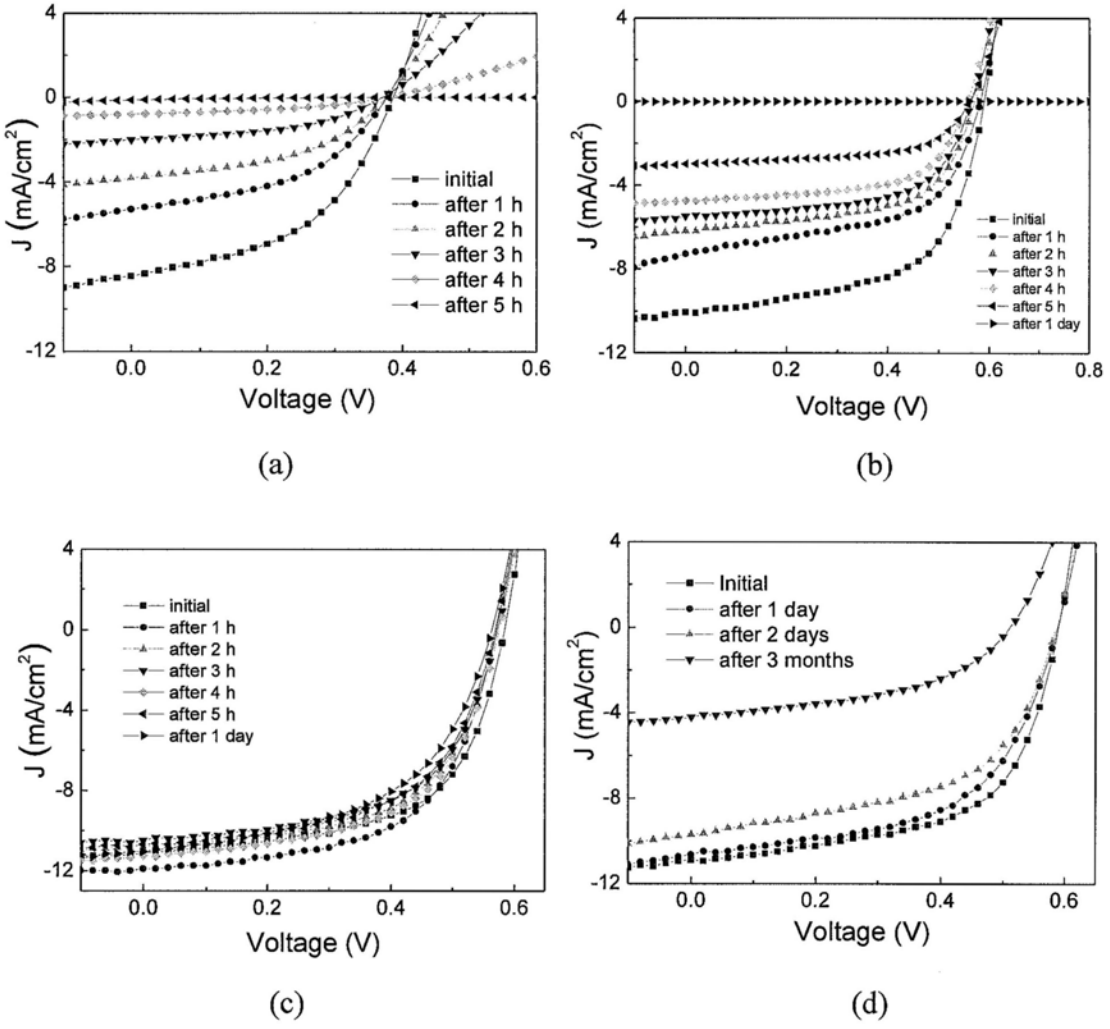

Fig.3.10 *J-V* characteristics as a function of storage time in the dark of P3HT:PCBM BHJ solar cells under illumination (a) without interfacial layer (Al only), (b) with LiF, (c) CrO_x layer, and (d) with the organic active layers that were pre-exposured to air for the indicated time before LiF and Al deposition.

For devices without any cathode interfacial layer, we observed that the degradation process is device area-dependent. As shown in Fig.3.11, the devices with larger area show better stability. On the other hand, degradation of Al-only devices with large area (0.72 cm^2) is still much faster than that of the CrO_x-modified devices with small active area, suggesting that increasing the device area could only slow down, but not stop, the failure of the entire device. For comparison, the degradation rate of our devices with the active area of 0.06 cm^2 is similar to that of the devices with 0.045cm^2 active area reported by Heeger *et al.* [16].

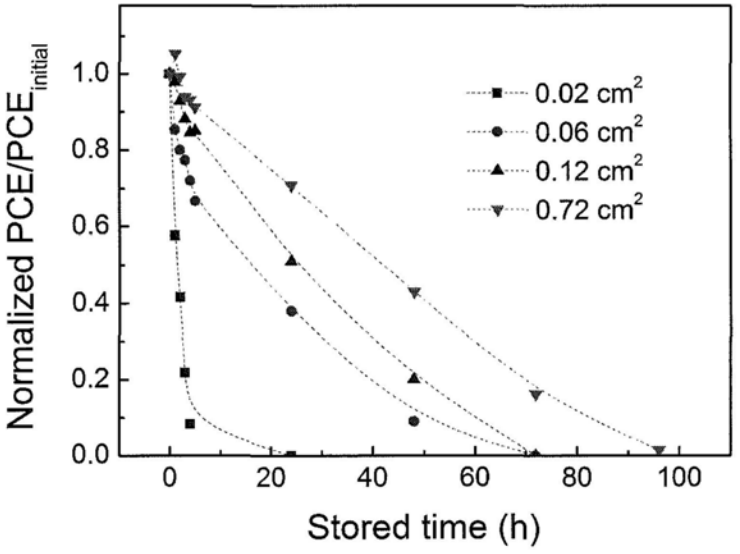

Fig.3.11 PCEs as a function of storage time in dark of P3HT:PCBM BHJ solar cells with different active areas and without any cathode interfacial layers (Al only).

There are several routes for oxygen and water diffusion into the cathode interface to cause the rapid degradation. It has been suggested that the oxygen and water can diffusion through pinholes or grain boundaries of Al electrode [39], or through the hygroscopic PEDOT:PSS layer from its edges to cause cathode oxidation [40]. We,

however, emphasize that diffusion of water or oxygen molecules from the top lateral side of the cathode/polymer interface significantly contributes to the degradation process because the degradation process is device area-dependent, as shown in Fig.3.12.

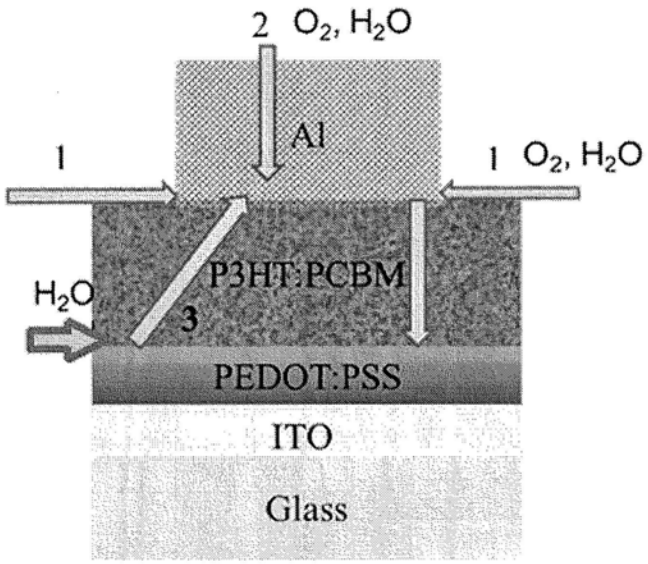

Fig.3.12 Routes of oxygen and water diffusion into the organic solar cells.

3.6.2 Formation of charge blocking layer at Al/organic contact

Fig.3.13 shows the changes of the dark *J-V* characteristics of the devices without any interfacial layer (Al only) during air exposure. The current density in the forward voltage dramatically decreases. The series resistance is extracted from the slope of the dark *J-V* curve at the voltage of 1.2 V [41]. The series resistance increases with storage time in air. Such rapid increase of series resistance can result from the degradation of the ITO and PEDOT:PSS interface, the degradation of the organic active layer, or the degradation of the cathode/organic interface. It is, however,

evident that the first two mechanisms do not account for the increase of the series resistance, as our control samples with pre-air exposed organic layers (corresponding to Fig.3.10 (d)) show *J-V* characteristics similar to the freshly made devices.

We therefore propose that the increase in series resistance is mainly due to the oxidation of Al at the organic/Al contact. This oxidation layer grows thicker upon air exposure time and hinders the charge transport between the Al cathode and the organic active layer. This process can be illustrated in the schematic diagrams shown in Fig.3.14: in fresh devices, both electrons and holes can be injected into the organic active layer to recombine; Upon air exposure, a charge-blocking barrier grows between the organic active layer and Al, resulting in the decrease of charge injection/extraction and the increase of series resistance.

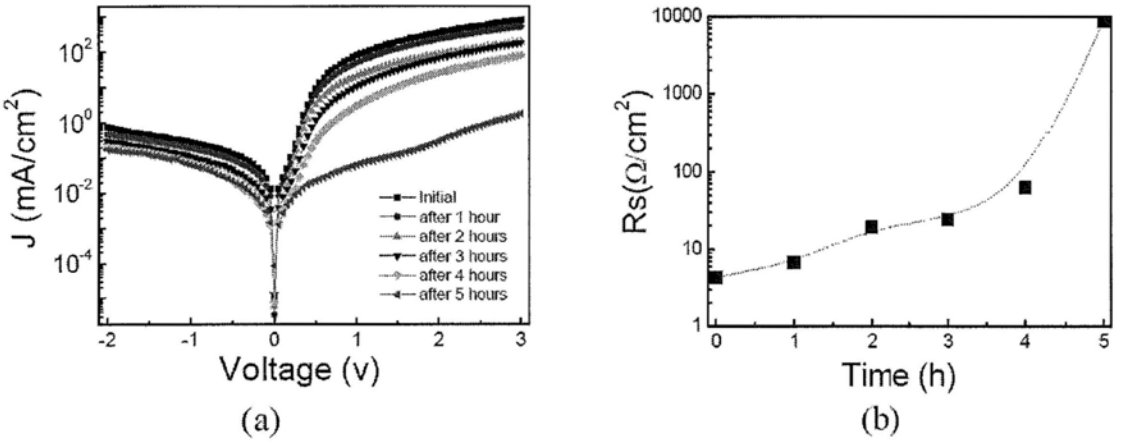

Fig.3.13 (a) Dark *J-V* characteristics as a function of storage time in dark of P3HT:PCBM BHJ solar cells without any interfacial layer (Al only), and (b) the corresponding series resistance.

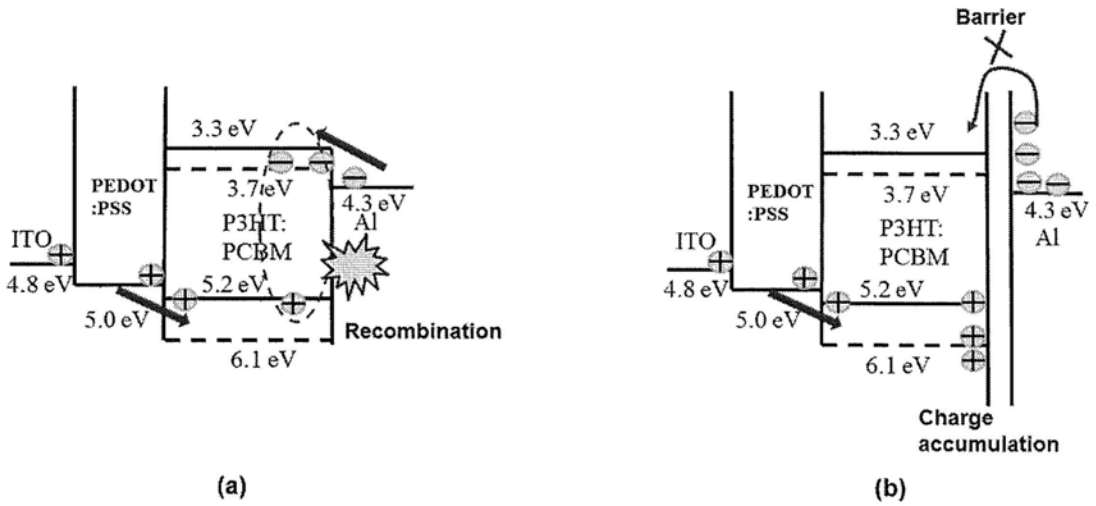

Fig.3.14 Energy-band diagrams of (a) recombination under bipolar injection at forward voltage in fresh devices and (b) a charge barrier formed at cathode interface to block charge extraction and injection in aged devices.

3.6.3 Observation of charge-blocking layer by impedance spectroscopy

To confirm our model on the growth of charge blocking layer at the cathode interface during degradation process, we performed impedance spectroscopy, which is a very useful tool for studying interface properties of organic electronic devices. It has been shown that in organic light-emitting diodes (OLEDs), the decrease in device capacitance at forward bias is always accompanied by the strong luminescence due to the recombination of electrons and holes [42-44]. The negative capacitance due to the charge recombination has also been reported in nanocomposite and polycrystalline solar cells [45-46]. The principle of negative capacitance is detail in chapter 5. Capacitance-voltage (*C-V*) characteristics of our devices are shown in Fig.3.15. For all fresh devices, the capacitance first increases with forward bias, reaching a maximum point close to the open-circuit voltage of the corresponding device, then

decreases, with some of them reaching negative values. The decrease of the device capacitance is consistent with previous reports [42-46] and suggests the turn-on of recombination of bipolar injected carriers at the electrode surface or the donor/acceptor interfaces.

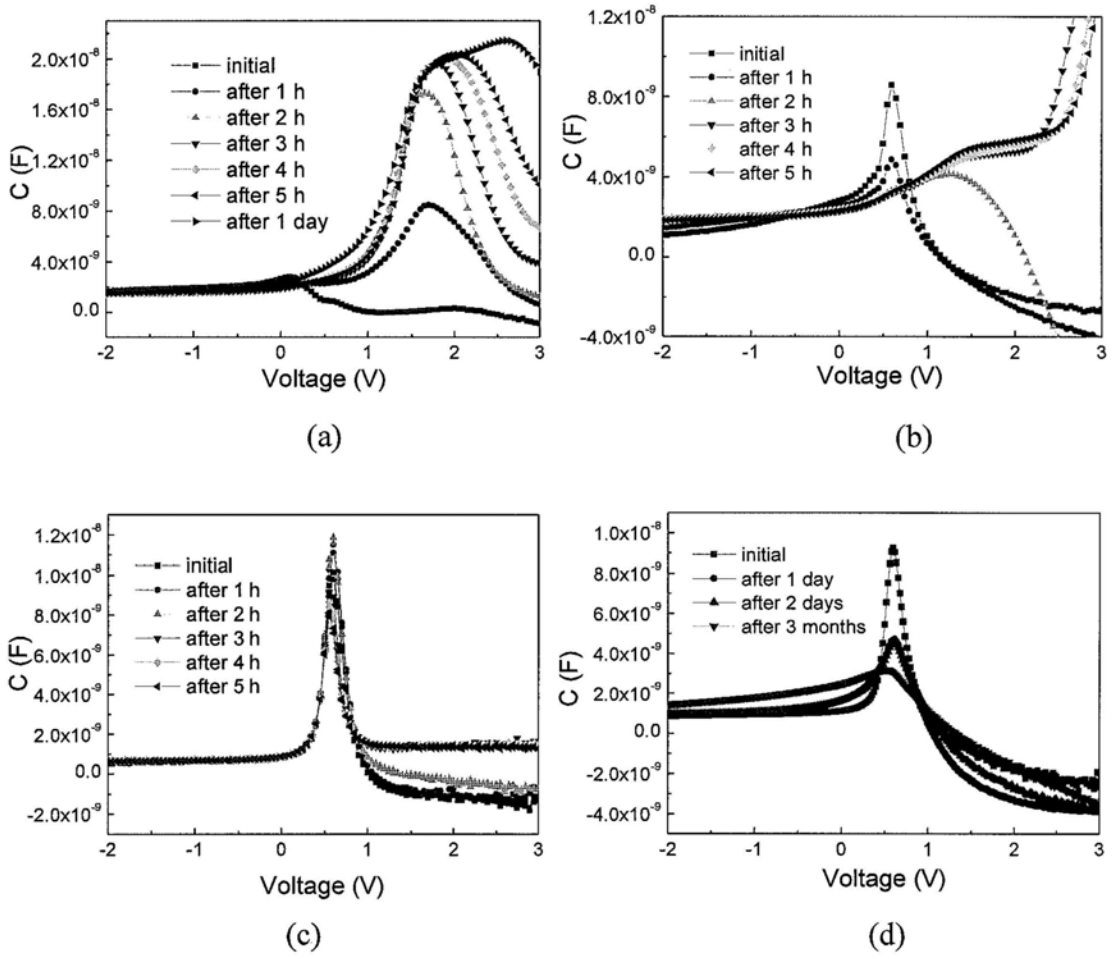

Fig.3.15 Capacitance-voltage (*C-V*) characteristics as a function of storage time of P3HT:PCBM BHJ solar cells (a) without interfacial layer (Al only), (b) with a LiF layer, (c) with a CrO_x layer, and (d) the active layers pre-exposured to air before LiF and Al deposition.

As shown in Fig.3.15 (a), the negative capacitance in the Al-only device disappeared after 1~2 h. And the maximum capacitance increased and shifted gradually to higher forward voltage. This supports our model that a charge-blocking layer has formed at the cathode interface (Fig.3.15 (b)) and that it grows thicker with time exposed to air, resulting in a larger forward voltage required for electron injection. The change of the *C-V* characteristics in the devices with a LiF interfacial layer was found very similar to the Al-only ones, with the negative capacitance disappearing after 2~3 hours.

However, the *C-V* characteristics in devices with a CrO_x interfacial layer are stable in air, similar to the ones of amorphous silicon solar cells (not shown here). The devices with their organic active layers kept in air for 1 day and 2 days before evaporation of LiF and Al had similar *C-V* characteristics as the fresh devices with a LiF interfacial layer and a CrO_x interfacial layer, as shown in Fig.3.15. These results confirm that the rapid failure of devices is not caused by the organic active layer, but by the degradation of the cathode interface due to a formation of the charge-blocking layer, and that the CrO_x interfacial layer improves device lifetime by preventing or reducing the formation of this layer.

3.6.4 Stability improvement by an interfacial bilayer (Mechanism for improved stability)

In order to further understand how the CrO_x layer can reduce the formation of a charge blocking layer, we fabricated devices with an interfacial bilayer and compared

their stability in air with our standard devices as shown in Fig.3.16. First, both the standard devices without interfacial layer (Al only) and with a LiF interfacial layer exhibited rapid decrease of J_{sc}, which is caused by the growth of a charge blocking layer at the cathode interface. The FF also decreased after several hours as a result of the increased series resistance. On the other hand, the V_{oc} of both devices remained relatively stable. This is not surprising, as the charge-blocking layer suppresses the charge recombination, which would benefit the charge built-in at the open-circuit condition. The standard devices with a CrO_x layer are much more stable in air. The J_{sc} and FF decreased very slowly, indicating that the growth of a charge blocking layer is much slower. The V_{oc} of the device appeared to drop. This could be caused by oxygen migration at the CrO_x-Al interface. It is suggested that the Al can obtain oxygen from CrO_x and therefore partially reduce chromium to its metallic state, by $Cr_2O_3 + 2\ Al \rightarrow 2\ Cr + Al_2O_3$ [47]. This process will increase the workfunction of cathode, thus reduce the V_{oc}. The fact that the J_{sc} and FF decrease much slower for the Al/CrO_x/organic contact than those for the Al/organic contact suggests that in the former case the growth of a charge blocking layer is largely suppressed, and therefore the carrier extraction will be affected to a less extent.

To further understand the reaction at the Al/CrO_x interface, we inserted a thin LiF layer between the Al and CrO_x to reduce the CrO_x-Al contact. The devices have an interfacial bilayer (ITO/PEDOT:PSS/P3HT:PCBM/CrO_x/LiF/Al) with ~0.8 nm thick LiF and ~4.2 nm thick CrO_x. Luckily, devices with an interfacial bilayer of CrO_x/LiF reach an initial PCE of 4.0%, with a J_{sc} of 11.0 mA/cm^2, V_{oc} of 0.6 V and FF of 0.64.

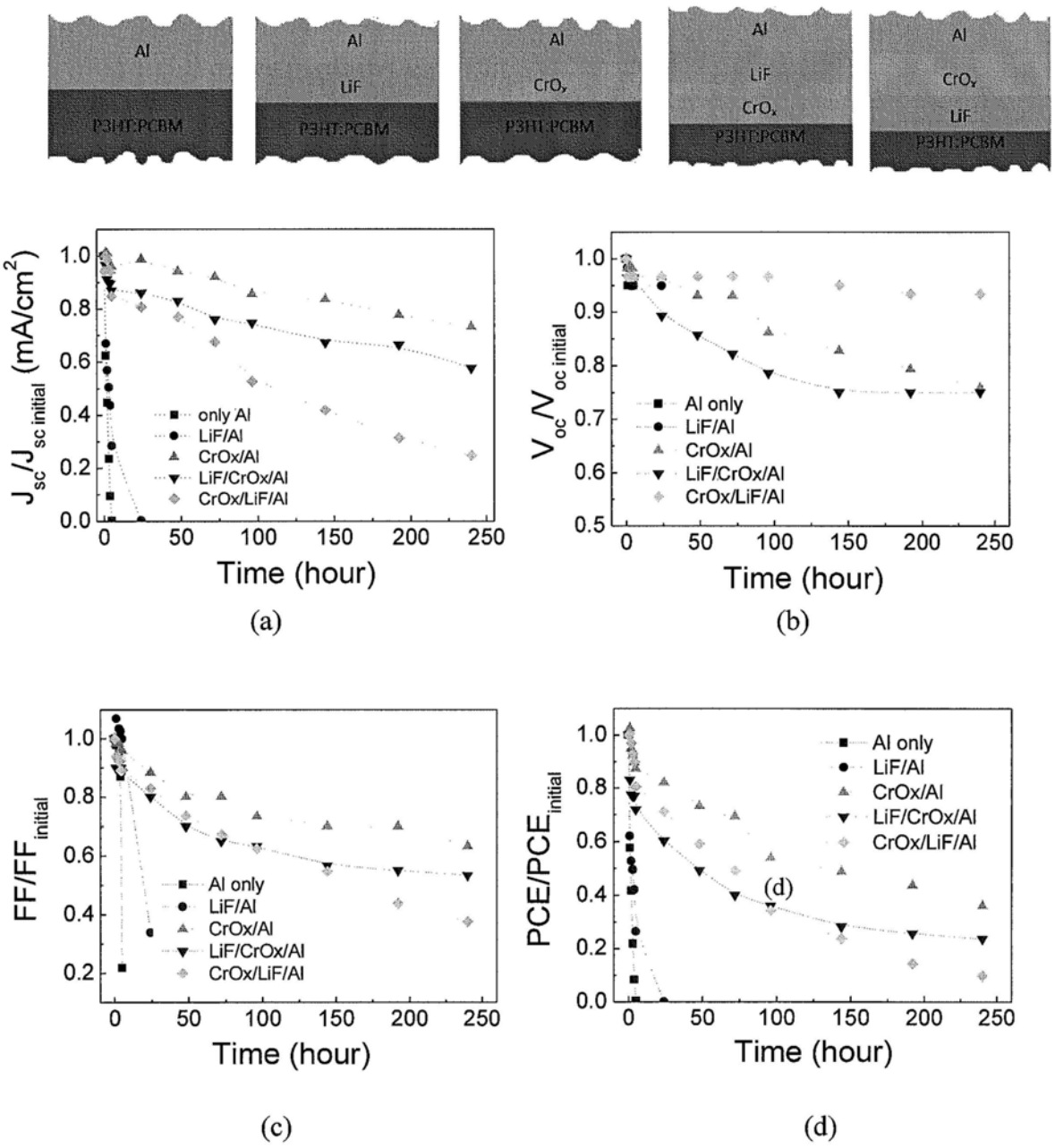

Fig.3.16 Comparison of (a) J_{sc}, (b) V_{oc}, (c) FF, and (d) PCE as a function of storage time for P3HT:PCBM solar cells with a interfacial layer of CrO_x, LiF, LiF/CrO_x, CrO_x/LiF and without any interfacial layer (Al only). Note that the device characteristics are monitored with increasing storage time for the same devices. The devices were not made in the same batch.

Devices with an interfacial bilayer of LiF/CrO_x exhibit an initial PCE of 3.9%. Inserting LiF on top of CrO_x can effectively increase its efficiency while increasing the V_{oc} (to be 0.6 V) as well as make it more stable. But the J_{sc} in devices with CrO_x/LiF bilayer decreases faster than that in devices with a CrO_x-only interfacial layer (Fig.3.16). This suggests that the direct contact between Al and CrO_x is necessary for good charge extraction. The reason for this will be further discussed later. Devices with the LiF layer between the organic active layer and the CrO_x (ITO/PEDOT:PSS/P3HT:PCBM/LiF/CrO_x/Al) also shows better stability than that with a LiF-only interfacial layer. But the V_{oc} still drops due to the change in the workfunction at the CrO_x-Al contact, as discussed for the case of standard devices with single CrO_x interfacial layer.

The above-mentioned results suggest that having CrO_x in direct contact with Al is necessary for the improvement of stability of carrier extraction at the cathode. It is reported that in the aluminothermic reduction of Cr_2O_3 [48-50], the initially aluminothermically formed Al_2O_3 layer can passivate the Cr_2O_3 substrate and protect it against further attack by thermally evaporated Al atoms [49], resulting in an ultra-thin Al_2O_3 interfacial layer. We believe that a somewhat similar scenario occurs in our devices, where the CrO_x interfacial layer improves the initial growth of Al by reducing Al diffusion into the organic active layer. This minimizes the interdiffusion region at the organic-Al contact caused by Al evaporation, and thus effectively improves the device stability. However, inserting a LiF interfacial layer between CrO_x and Al will reduce the improvement of initial Al growth by CrO_x.

3.6.5 Chemical composition analysis at Al/organic contact

The electrical measurements suggest that the CrO_x layer plays a key role in retarding the device degradation process. To quantify the composition variation at the interface area, we performed X-ray photo-electron spectroscopy (XPS) on some of our samples.

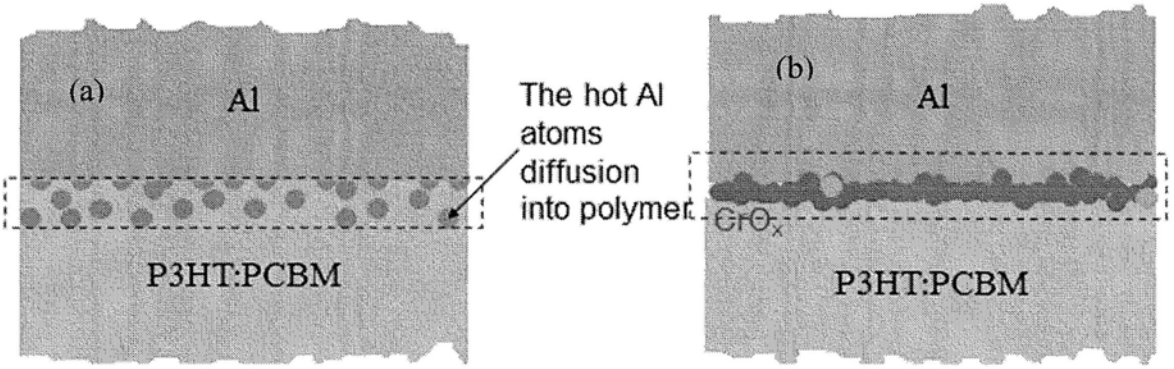

Fig.3.17 Schematic of the interface between the organic active layer and Al cathode (a) without any interfacial layer and (b) with CrO_x as an interfacial layer between them.

As shown in Fig.3.17, for devices without any interfacial layer, during the evaporation of Al, the hot Al atoms can diffuse into the organic active layer and are most likely to form small Al clusters or particles, leading to a large interdiffused area between the organic active layer and Al cathode. It is thought that the interdiffused area is most likely to be oxidized and form Al_2O_3, an insulator. And it is thought that the initially deposited Al atoms were directly oxidized into Al_2O_3 due to the oxygen adsorption at sample surface and possible remaining oxygen in chamber. However, the CrO_x can stop, at least reduce, the diffusion of Al, thus resulting in a small interfacial area between the organic active layer and Al.

To probe the material composition at the Al/organic interface, XPS measurement was employed with an Ar^+ etching process on our real devices. The etching rate is around 0.034 nm/s (using that of SiO_2 as reference). Displayed in Fig.3.18 is the XPS depth profile of the devices with and without a CrO_x interfacial layer. A mixed layer with Al, O, and C was observed at the organic-metal interface. Two peaks corresponding to Al 2*p* were observed, with one peak (72 eV) related to Al metal, and the other (75 eV) related to Al_2O_3, suggesting that Al was partially oxidized at the interface.

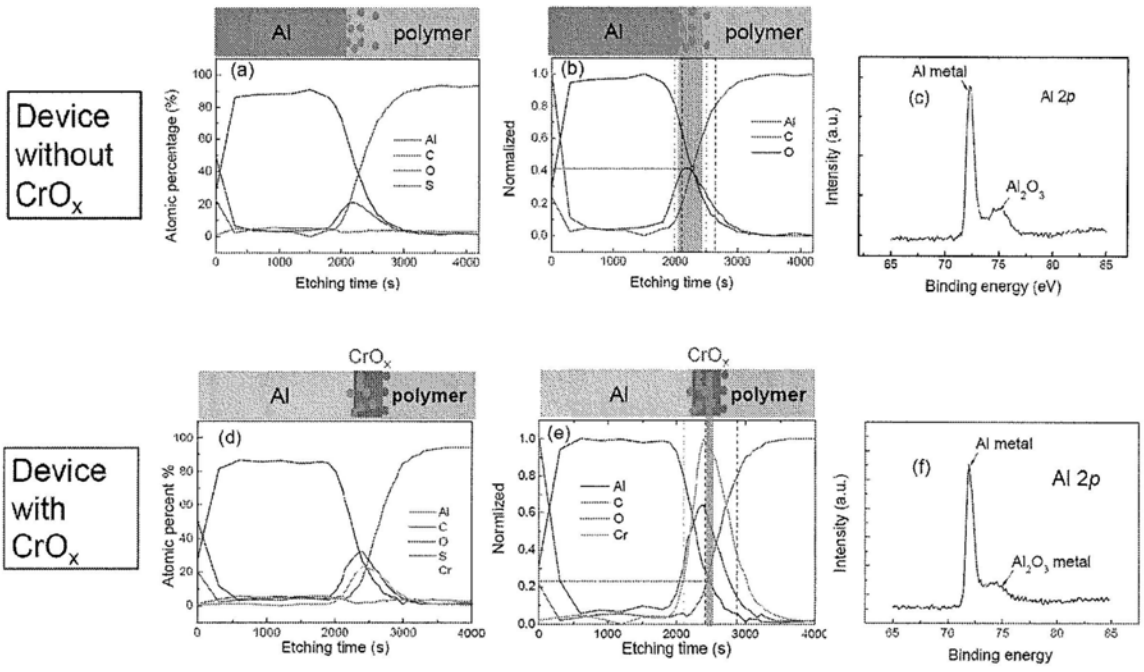

Fig.3.18 XPS depth profiles of (a) atomic distributions in device without any cathode interfacial layer (Al only), (b) normalized atomic distributions in device Al only, (c) Al XPS at interfacial layer of the device Al only, (d) atomic distributions in device with CrO_x, (e) normalized atomic distributions in device with CrO_x, (f) Al XPS at interfacial layer of the device with CrO_x.

In order to compare the thickness of the Al_2O_3 layer in the devices with and without a CrO_x interfacial layer, the atomic percentages of Al, O, and C were normalized. We define the profile of the downside Al interfacial region (above the organic or CrO_x layer) as T_{Al}, the corresponding etching time period which starts from the point corresponding to 80% of the normalized Al atomic percent signal and ends at the point of 20% signal. Similarly, the profile of the upside organic interfacial region is defined by the distance T_C , which corresponds to the period between the etching time point of 20% signal of the normalized C atomic percent and 80% of the one in this devices. The overlapping area $T_{Al\text{-}C}$ between the downside Al interface and the upside organic active interface is therefore the Al-organic interactive (or interdiffusion) region. The overlapping distance (the shaded area in Fig.3.18 (b) and Fig.3.18 (d)) between Al and the organic active layer for the devices without CrO_x interfacial layers ($T_{Al\text{-}C(Al\ only)}$) is 400 s, which corresponds to an estimated thickness of ~13.6 nm. The corresponding value for the devices with CrO_x ($T_{Al\text{-}C(CrOx)}$) is 100 s, with an estimated thickness of ~3.4 nm. The XPS spectroscopic profiles support our model that less Al diffuses into the organic active layer in the devices with a CrO_x interfacial layer, which acts as a blocking layer that prevents Al from penetrating into the polymer and thus reduces the effective interdiffusion area at the organic-Al interface. The observation of a thick interdiffusion region between Al and the organic active layer in the Al-only device is in agreement with its *J-V* and *C-V* characteristics above, which show that the charge blocking layer suppresses charge extraction/injection, and it gradually grows and becomes thicker. The formation of a

thicker charge blocking layer due to the oxidation of the organic-Al interface causes the rapid degradation of device performance. It is important to point out that the XPS profiles can only provide a qualitative comparison between two types of the devices. Firstly, the etching process itself could cause migration of materials, which would smear out the interface border. Secondly there are errors associated with estimating thickness by assuming a constant etching rate from SiO_2 for all the layers. Both factors could result in inaccurate estimation of layer thickness. A cross-section TEM would be a desirable complementary tool to investigate these interfaces.

The observation of a thick interdiffusion region at the Al/organic contact is intriguing. Generally the oxidation of Al is self-terminating thanks to the formation of an initial thin (< 2 nm [51]) and compact layer of Al_2O_3 that can prevent further oxidation. It has also been shown that deposition of an ultrathin (< 2 nm) Al_2O_3 layer between the polymer and aluminum cathode can improve the performance of organic solar cells and OLEDs, although the performance exponentially decreases when the Al_2O_3 layer becomes thicker [52]. During thermal evaporation, hot Al atoms with high kinetic energy can diffuse into the organic active layer and form a rough or even discontinuous interdiffused area. An interdiffused area of ~5 nm has been observed before in organic BHJ solar cells at the Al/organics contact [35]. In organic memory devices, the metal diffusion during the evaporation process has been utilized to create small metal islands in the organic layer to generate memory effects [54]. In our devices, it is likely that the thermal evaporation of Al results in a thick interfacial region that can gradually been oxidized to form a charge-blocking layer.

Our results show that interface properties are crucial for device stability. An interfacial (buffer) layer protecting the cathode interface from Al diffusion during evaporation is extremely important and should have the following characteristics. Firstly, it should not introduce damage to the active layer. Secondly, the buffer layer should not be easily oxidized or susceptible to water. Thirdly, it should be sufficiently electrically conductive to allow a buffer layer of sufficient thickness to prevent hot Al diffusion into polymer. Lastly, its conduction band should be appropriately aligned with the cathode metal. N-type oxide semiconductors with conduction band around 4 eV (e.g., Cr_2O_3, TiO_2, Cu_2O, ZnO) make good choices as interfacial layers between the organic active layer and following thermally evaporated Al cathode for improving the device performance and stability. And thermal evaporation of a thin metal oxide layer is a useful method for enhancing device lifetime, primarily because of its compatibility flexible device concepts and its simple fabrication process.

3.6 Summary of Chapter 3

Chromium oxide (CrO_x), which is formed by simultaneous oxidation of thermally evaporated Cr under low vacuum condition, is employed as a cathode interfacial layer to improve performance and stability of P3HT:PCBM solar cells. The optical properties and electrical properties of CrO_x are favorable for a cathode interfacial layer. Cathode interfacial degradation is crucial for P3HT:PCBM BHJ solar cells with Al cathode. In devices without any cathode interfacial layer or with LiF as an interfacial layer, the top organic-Al interface degrades upon air exposure and forms

a charge blocking layer to hinder charge transportation. Insertion of a thin interfacial layer of thermally evaporated CrO_x between the organic active layer and Al cathode can greatly improve the stability of P3HT:PCBM solar cells. It is found that the CrO_x interfacial layer functions as a protective layer by stopping or minimizing penetration of thermally evaporated Al into the organic active layer to form a diffused organic-Al interface, which would then result in a large oxidized interfacial area upon air exposure. By eliminating or retarding the formation of this charge blocking layer at the cathode/organic interface, the CrO_x layer is able to extend the device lifetime of BHJ organic solar cells. Our model on degradation and stability improvement by CrO_x is supported by measurements of *J-V*, impedance spectroscopy, and X-ray photoelectron spectroscopy (XPS). Our study suggests that metal oxides could be good material candidates to improve the organic-metal contacts , thus greatly increase the performance and stability of organic optoelectronic devices.

Reference:

Most of the content of this chapter were adapted from published work (i and ii):

i. *Mingdong Wang, Qin Tang, Jin An, Fangyan Xie, Jian Chen, Shizhao Zheng, King Young Wong, Qian Miao, and Jianbin Xu, Performance and Stability Improvement of P3HT:PCBM-Based Solar Cells by Thermally Evaporated Chromium Oxide (CrOx) Interfacial Layer, ACS Applied Materials and Interfaces, 10, 2699–2702 (2010).*

ii *Mingdong Wang, Fangyan Xie, Jun Du, Qin Tang, Shizhao Zheng, Qian Miao, Jian Chen, Ni Zhao, J. B. Xu, Aluminum Cathode Interface Degradation of Polymer Solar Cells and Reduced by Incorporation of Chromium Oxide (CrO_x) Layer, Solar Energy Material and Solar Cells, (in press).*

[1] S. H. Park, A. Roy, S. Beaupre, S. Cho, N. Coates, J. S. Moon, D. Moses, M. Leclerc, K. Lee, A. J. Heeger, Nat. Photonics 3, 297 (2009).

[2] Y. Liang, Z. Xu, J. Xia, S.-T. Tsai, Y. Wu, G. Li, C. Ray, L. Yu, Adv. Mater. 22,

E135 (2010).

[3] H. Y. Chen, J. Hou, S. Zhang, Y. Liang, G. Yang, Y. Yang, L. Yu, Y. Wu, G. Li, Nat. Photonics 3, 649 (2009).

[4] W. Cai, X. Gong, Y. Cao, Sol. Energy Mater. Sol. Cells 94, 114 (2010).

[5] J. Xue, P. Rand Barry; S. Uchida, S. R. Forrest. J. Appl. Phys. 98, 124903 (2005).

[6] H.Y. Wei, J. H. Huang, K. C. Ho, C, -W. Chu, ACS Appl. Mater. Inter. 5, 1281 (2010).

[7] T. Tromholt, S. A. Gevorgyan, M. Jørgensen, F. C. Krebs, S. -Hvid, O. Kristian, ACS Appl. Mater. Inter. 1, 2768 (2009).

[8] M. Lögdlund, J. L.Bredas, J. Chem. Phys.101, 4357 (1994).

[9] H. Antoniadis, B. R. Hsieh, M. A. Abkowitz, S. A. Jenekhe, M. Stolka, Synth. Met. 62, 265 (1994).

[10] L. S. Hung, R. Q.Zhang, P. He, M. G. Mason, J. Phys. D: Appl. Phys. 35, 103 (2002).

[11] F. C. Chen, J. L. Wu, S. S.Yang, K. -H. Hsieh, W. C. Chen, J. Appl. Phys. 103, 103721 (2008).

[12] S. K. M. Jonsson, E. Carlegrim, F. Zhang, W. R. Salaneck and M. Fahlman, Jpn. J. Appl. Phys. 44, 3695 (2005).

[13] J. M. Bharathan, Y. Yang, J. Appl. Phys. 84, 3207 (1998).

[14] L. -M. Chen, Z. Xu, Z. Hong and Y. Yang, J. Mater. Chem. 20, 2575 (2010).

[15] M. O. Reese, M. S. White, G. Rumbles, D. S. Ginley and S. E. Shaheen, Appl. Phys. Lett. 92, 053307 (2008).

[16] J. Y. Kim, S. H. Kim, H. H. Lee, K. Lee, W. Ma, X. Gong, A. J. Heeger, Adv. Mater. 18, 572 (2006).

[17] W. Baek, M. Choi, T. Yoon, H. Lee, Y. Kim, Appl. Phys. Lett. 96, 133506 (2010).

[18] J.-S. Huang, C.-Y. Chou, and C. -F. Lin, IEEE Electron device Lett. 31 (4), 332 (2010)

[19] A. B. Chwang, M. A. Rothman, S. Y. Mao, R. H. Hewitt, M. S.Weaver, J. A. S ilvernail, K. Rajan, M. Hack, J. J. Brown, X. Chu, L. Moro, T. Krajewski, N. Rutherford, Appl. Phys. Lett. 83, 413(2003).

[20] L. Moro, T. A. Krajeweski, N. M. Rutherford, O. Philips, R. J. Visser, M. E. Gross, W. D. Bennett, G. L. Graff, A Transparent, Proc. SPIE-Int. Soc. Opt. Eng. 83, 5214 (2004).

[21] M. Pagliaro, G. Palmisano, R. Ciriminna, Wiley-VCH, Flexible Solar Cells, Berlin, Germany (2008).

[22] X. Pang, K. Gao, F. Luo, Y. Emirov, A. A. Levin and A. A. Volinsky, Thin Solid Films 517, 1922 (2009).

[23] Y. Xu, M. A. A. Schoonen, American Mineralogist, 85, 543 (2000).

[24] L. J. Van der Pauw, Philips technical review 59, 220 (1958).

[25] L. Yang, H. Xu, H. Tian, S. Yin, F. Zhang, Sol. Energy Mater. & Sol. Cells 94,1831 (2010).

[26] C. C. Chang, C. F. Lin, J. M. Chiou, T. H. Ho, Y. Tai, J. H. Lee, Y. F. Chen, J. K. Wang, L. C. Chen, K. H. Chen, Appl. Phys. Lett. 96, 263506 (2010)

[27] S. Pokhrel, C. E. Simion, V. Quemenera, N. Barsan and U. Weimar, Sens. Actuators B 133,78 (2008).

[28] J. F. Weaver, H. A. E. Hagelin-Weaver, G. B. Hoflund and G. N. Salaita, Appl.Surf. Sci. 252, 7895 (2006).

[29] H. C. Barshilia, N. Selvakumar, K. S. Rajam, and A. Biswas, J. Appl. Phys. 103, 023507 (2008).

[30] R. Cheng, B. Xu, C. N. Borca, A. Sokolov, C. -S. Yang, L. Yuan, S. -H. Liou, B. Doudin, and P. A. Dowben, Appl. Phys. Lett. 79, 3122 (2001).

[31] F. Bechstedt, Principles of surface physics, Springer-Verlag, Berlin Heidelberg, (2003).

[32] A. J. Medford, M. R. Lilliedal, M. Jørgensen, D. Aarø, H. Pakalski, J. Fyenbo, F. C. Krebs, Optics Express 103, A272 (2010).

[33] F. C. Krebs, T. Tromholt, M. Jørgensen, Nanoscale 2, 873 (2010).

[34] F. C. Krebs, T. D. Nielsen, J. Fyenbo, M. Wadstrøm, and M. S. Pedersen, Energy Environ. Sci. 3, 512 (2010).

[35] M. Jørgensen, K. Norrman, F. C. Krebs, Sol. Energy Mater. Sol. Cells, 92,686 (2008).

[36] K. Norrman, F. C. Krebs, Sol. Energy Mater. Sol. Cells, 90,213 (2006).

[37] Y. Nam, D. Su, C. T. Black, Adv. Funct. Mater. 19, 3552 (2009).

[38] F. So and D. Kondakov, Adv. Mater. 22, 3762 (2010).

[39] K. Norrman, N. B. Larsen, F. C. Krebs, Sol. Energy Mater. Sol. Cells 90, 2793 (2006).

[40] E. Voroshazi, B. Verreet, A. Buri, R. Müller, D. D. Nuzzo and P. Heremans, Organ. Electron. 12 736 (2011).

[41] H.-L Yip, S. K. Hau, N. S. Baek, H. Ma, and A. K. -Y. Jen, Adv. Mater. 20, 2376 (2008).

[42] J. Bisquert, G. Garcia-Belmonte, A. Munar, M. Sessolo, A. Soriano, H. J. Bolink, Chem. Phys. Lett. 465, 57 (2008).

[43] E. Ehrenfreund, C. Lungenschmied, G. Dennler, H. Neugebauer, N. S. Sariciftci, Appl. Phys. Lett. 91, 012112 (2007).

[44] J. Bisquert, G. Garcia-Belmonte, A. Pitarch, H. J. Bolink, Chem. Phys. Lett. 422, 184 (2006).

[45] I. Mora-Sero´ , J. Bisquert, F. Fabregat-Santiago, G. Garcia-Belmonte, G. Zoppi, K. Durose, Y. Proskuryakov, I. Oja, A. Belaidi, T. Dittrich, R. Tena-Zaera, A. Katty, C. Levy-Clement, V. Barrioz, S. J. C. Irvine, Nano Lett. 6, 640 (2006).

[46] J. Bisquert, G. Garcia-Belmonte, A. Munar, M. Sessolo, A. Soriano, H. J. Bolink, Chem. Phys. Lett. 465, 57 (2008).

[47] http://en.wikipedia.org/wiki/Chromium(III)_oxide

[48] K. Dumbuya, K. Christmann, S. L. M. Schroeder, Langmuir 23, 5386 (2007).

[49] B. Sarangi y, H. S. Ra , A. Sarangi, Scand. J. Metall. 25, 256 (1996).

[50] P. Jin, S. Nakao, S. X. Wang, L. M. Wang, Appl. Phys. Lett. 82, 1024 (2003).

[51] F. Li, H. Tang, J. Anderegg, J. Shinar, Appl. Phys. Lett. 70, 1233, (1997).

[52] S. T. Zhang, Y. C. Zhou, J. M. Zhao, Y. Q. Zhan, Z. J. Wang, Y. Wu, X. M. Ding, X. Y. Hou, Appl. Phys. Lett. 89, 043502 (2006).

[53] L. D. Bozano, B. W. Kean, V. R. Deline, J. R. Salem, J. C. Scott, Appl. Phys. Lett. 84, 607 (2004).

Chapter 4

Influence of metal oxides on lifetime of organic solar cells

4.1 Overview

In this chapter, we extend the previously proposed mechanism of device degradation and stability improvement to other metal oxides and organic solar cell systems. Firstly, we investigated the use of CuO_x as a cathode interfacial layer to increase the device lifetime of P3HT:PCBM BHJ solar cells. Then, we demonstrated that a CrO_x cathode interfacial layer can be applied to a variety of organic solar cell systems, including poly[(2-methoxy-5-ethylhexyloxy)-1,4-phenylenevinylene] (MEHPPV:PCBM) BHJ, Copper phthalocyanine ($CuPc/C_{60}$) bilayer, and poly(9,9-dioctylfluorene-co-bis-N, N′-(4,butylphenyl)-bis-N,N′-phenyl-1,4-phenylene -diamine) and poly(9,9-dioctylfluorene-co-benzothiadiazole) (PFB:F8BT) BHJ, to improve the device stability. The extent of the stability improvement varies for different systems, and the underlying reason will be discussed.

4.2 Lifetime improvement of P3HT:PCBM cells by copper oxide (CuO_x)

4.2.1 Introduction

It has been recently reported that applying a cathode/organic interfacial layer, such as TiO_2 and fullerene/LiF, can reduce the degradation of BHJ solar cells [1-2]. In the results mentioned in the previous chapters, we found that the device stability of OPVs depends strongly on the cathode interfacial layers and that chromium oxide can effectively improve the device lifetime [3]. To explore if this finding can be applied to

other oxide systems and to investigate the fundamental mechanism behind the cathode interface degradation, we used copper oxide (CuO_x) and a CuO_x/LiF bilayer to modify the cathode/organic interface. A significant improvement in device stability was achieved and the mechanisms for this improvement will be discussed.

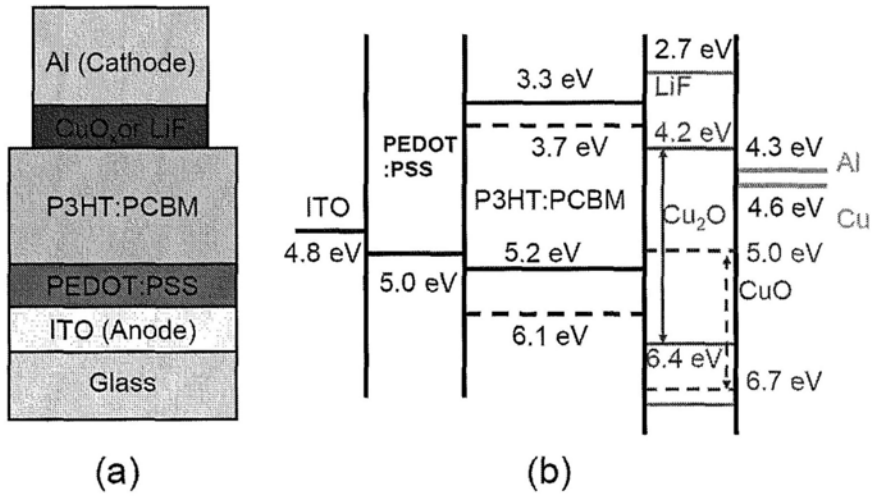

Fig.4.1. (a) Photovoltaic device structure, (b) schematic energy diagrams composed of different organics and interfacial layers.

4.2.2 Experimental details

The device structure and energy diagram are shown in Fig.4.1. A thin CuO_x layer (ca.5 nm) was deposited onto the organic active layer by thermal evaporation of copper metal under low vacuum (with base pressure of 1.0×10^{-2}~5.0×10^{-3} Pa) condition. The deposition rate of CuO_x was about 0.1-0.2 Å/second. It was easier to thermally evaporate the CuO_x film than the CrO_x film, because the melting point of Cu (970°C) is much lower than that of chromium metal (1850 °C). The active area of all devices is 1 mm × 2 mm. The devices with a CuO_x/LiF bilayer

(ITO/PEDOT:PSS/P3HT:PCBM/LiF/CuO_x/Al, and ITO/PEDOT:PSS/P3HT:PCBM/CuO_x/LiF/Al) were also fabricated and tested under the same conditions. The thickness of LiF in bilayer is about 0.6 nm. The other detailed procedures for device fabrication and measurement are the same as those in chapter 3. For all devices, no external package or encapsulation was applied after device fabrication.

4.2.3 Results and discusses

4.2.3.1 Device performance with cathode interfacial layers

Fig.4.2 shows the *J-V* characteristics of P3HT:PCBM BHJ devices without and with cathode interfacial layers under illumination. The parameters of merit for all the devices are listed in Table 4.1. Devices without any interfacial layer (Al only) had a PCE of 1.5%, while devices with a CuO_x interfacial layer (ITO/PEDOT:PSS/P3HT:PCBM/CuO_x/Al) exhibited a similar PCE with an increased J_{sc} but decreased V_{oc}. The reduction in V_{oc} is most likely due to the change in the cathode work function: both copper (around 4.6 eV [4]) and CuO_x (around 4.9 eV [5]) have a work function higher than Al, which is not favorable for obtaining high V_{oc}. In contrast, the devices with the LiF/CuO_x interfacial bilayer showed significantly improved V_{oc}. This suggests that LiF can improve the organic/cathode contact such that the V_{oc} loss due to the energy level offset can be eliminated. In the case of the P3HT:PCBM/CuO_x/LiF/Al structure, although CuO_x is in immediate contact with the organic layer, we suspect that the oxide layer is doped by LiF during evaporation.

Therefore, a good energy-level alignment can still form at the organic/cathode contact. Although applying a CuO_x layer alone cannot improve the overall device performance, it is already sufficient to improve the device stability by approximately two orders, as will be discussed later.

Table 4.1 Initial parameters of P3HT:PCBM solar cells without any interfacial layer (Al only), and with interfacial layers of LiF, CuO_x, CuO_x/LiF, and LiF/CuO_x, respectively.

Sample	PCE (%)	V_{oc} (V)	J_{sc} (mA/cm^2)	FF
Al only	1.5	0.40	8.45	0.46
LiF	3.5	0.59	10.08	0.59
CuO_x	1.5	0.34	9.8	0.45
CuO_x/LiF	3.0	0.55	10.7	0.52
LiF/CuO_x	3.1	0.55	11.0	0.53

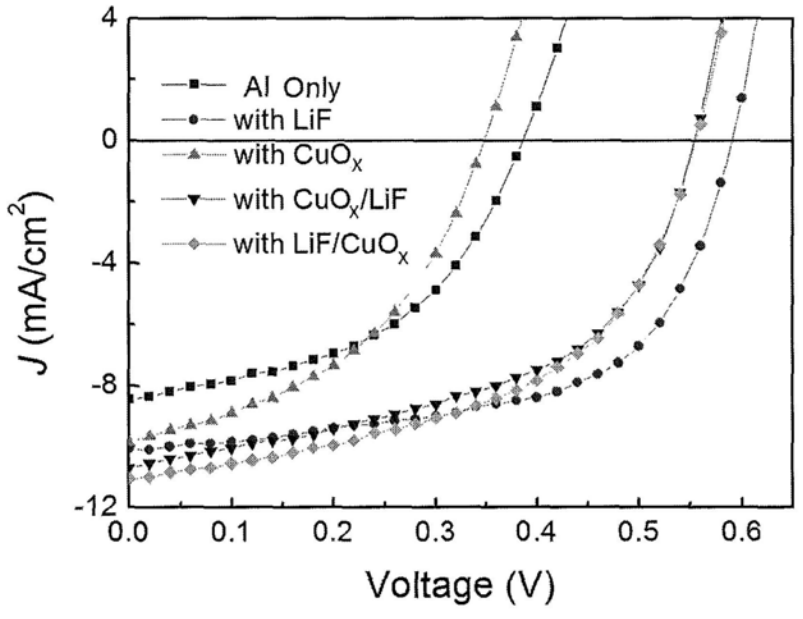

Fig.4.2. *J-V* characteristics of P3HT:PCBM BHJ solar cells under AM1.5 illumination with 100 mW/cm^2 light intensity.

It is well known that Cu metal can be easily oxidized. In our experiment, a low vacuum condition (deposition pressure around 10^{-2} Pa) was purposely used during the thermal evaporation of Cu so that there would be a considerable amount of oxygen left in the chamber to react with hot Cu atoms to form Cu_2O or CuO. Cu_2O and CuO are generally p-type semiconductors due to a high concentration of Cu vacancies [6-7]. On the other hand, it has been suggested that excess Cu can lead to Cu interstitials and/or O vacancies in copper oxide, which results in an n-type conductivity [8]. To elucidate this point, we have performed a 4-probe Hall-effect measurement (BIO-RAD Hall system) on the thermally evaporated copper oxide (CuO_x) thin films. N-type transport behavior was observed, with a carrier mobility of 1.2 $cm^2/V \cdot s$, which is much higher than that of CrO_x and TiO_x [1, 3]. The high mobility is preferable for charge extraction in our current device structure.

4.2.3.2 Composition analysis by XPS

To confirm the formation of CuO_x as well as study its compositional information, X-ray photoelectron spectroscopy (XPS) analysis was performed. Cu 2*p* XPS and Cu *LMM* Auger spectra at the top surface of CuO_x films are shown in Fig.4.3 (a) and (b). The XPS detects $Cu2p_{3/2}$ and $Cu2p_{1/2}$ at 932.5 eV and 952.3 eV. Fitting of the Cu $2p_{3/2}$ spectrum reveals that the primary peak at 934.6 eV is accompanied by two shakeup peaks on the higher binding energy side at 941.5 eV and 944.0 eV and is therefore attributed to the Cu^{2+} state [9]. The peak at 932.5 eV is assigned to Cu^{+}, which is

confirmed by its characteristic peak at 916.3 eV in the auger spectra of Cu *LMM* at which is in the range of the values of Cu^{+} states [10]. The Cu *LMM* kinetic energy of metallic Cu^{0} is about 918 eV [10]. To find out the depth profile of the different chemical species present at the CuO_x/organic interfaces, we performed XPS measurements in combination with sputter profiling using a 0.5 keV Ar^{+} ion beam at 300 nA which is the smallest power used to etching in our instrument. As shown in Fig.4.3 (c)-(f), we observed from the combined spectra of depth profiles that (1) Cu^{2+} species disappear after 30 s of etching, (2) Cu^{+} decreases after 60 s of etching, and (3) Cu^{0} gradually increases at the same time (from the arising of a peak at 918.1 eV in the Cu *LLM* Auger spectra). Interestingly, after 720 s of etching the amount of Cu^{+} increases again, and it becomes the most abundant copper species after 1440 s of etching. Meanwhile we measured the two chemical states of S. The peak around 164 eV is attributed to the S in P3HT, and the one around 162 eV possibly results from reaction of S with Cu. Note that a similar reaction product of S and Ca was measured before by XPS [11]. The XPS results show that the CuO_x film is composed of Cu_2O, CuO and Cu. During the initial stage of evaporation some Cu atoms may diffuse into polymer to react with S, while the first few atomic layers of CuO_x are composed of Cu-rich Cu_2O. The CuO at the top surface is mainly due to oxidation of Cu_2O in air. The diffused Cu species in the organic active layer can cause the lower V_{oc} due to its energy diagram shown in Fig.4.1 (b), which is in agreement with the results of lower V_{oc} in the device with CuO_x layer.

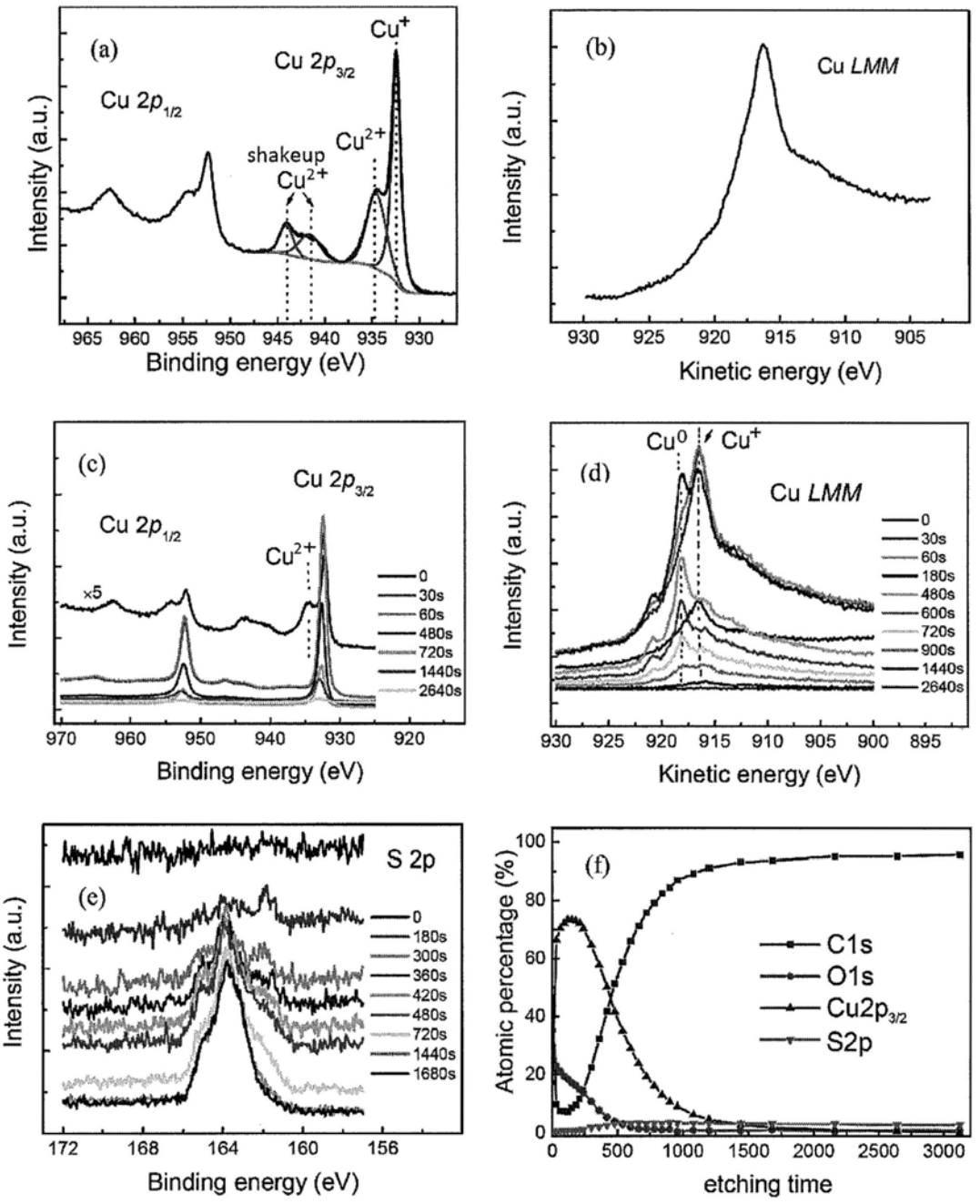

Fig.4.3 (a) Cu 2*p* XPS (b) Cu *LMM* Auger spectrum at the top surface, (c) Cu 2*p* XPS depth profile, (d) Cu *LMM* Auger spectra of depth profile, (e) S 2*p* XPS depth profile and (f) atomic percentages depth profile for 5 nm CuO_x films on the active layer of P3HT:PCBM.

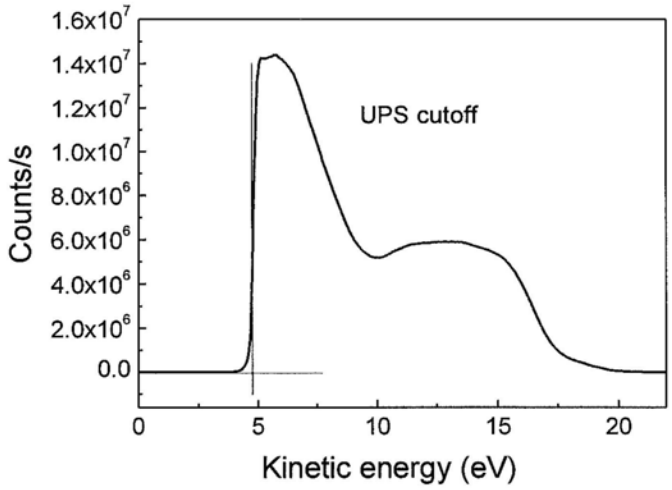

Fig.4.4 UPS spectra of 5 nm CuO_x films on the active layer of P3HT:PCBM.

To check the workfunction of our own CuO_x films, UPS measurement was employed. A typical UPS spectrum of thermally evaporated CuO_x is shown in Fig.4.4. It is usual to apply bias voltage to make the cutoff edge at the lower binding energy part sharp, from which a linear extrapolation is used to determine the workfunction. The workfunction is obtained to be 4.9 eV, which is very similar to the obvious reported value of copper oxide [5]. A material with a high workfunction is not a desirable cathode interfacial layer because high work-function makes it difficult to obtain a high open circuit voltage. This is why the device with a CuO_x layer had even lower V_{oc} than one without any interfacial layer (the workfunciton of Al is determined to be 4.2 eV). Further inserting a LiF layer between the organic active layer and CuO_x or between CuO_x and Al, however, is most likely to reduce the workfunction of the whole contact at the cathode, which is why a CuO_x/LiF interfacial bilayer improves the V_{oc} of the devices.

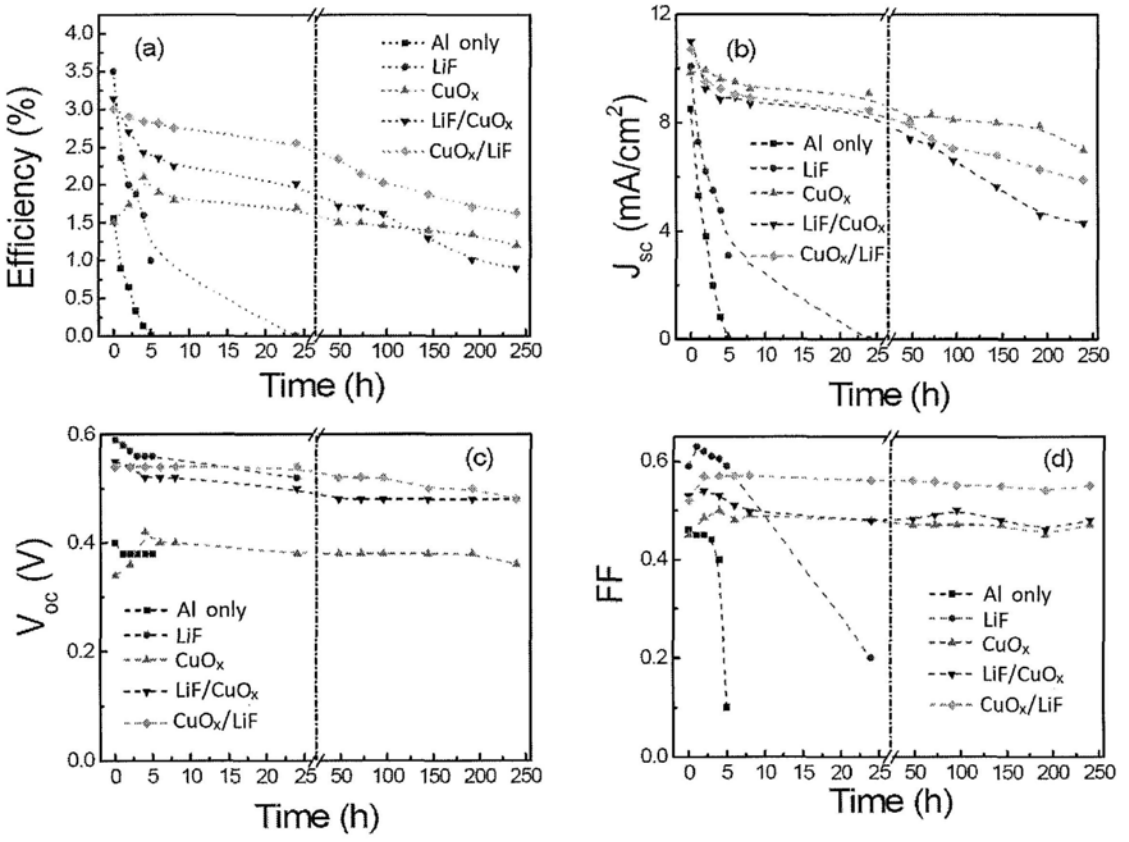

Fig.4.5 Comparison of the (a) power conversion efficiencies (PCE), (b) short circuit current (J_{sc}), (c) open circuit voltage (V_{oc}), and (d) fill factor (FF), as a function of storage time for polymer solar cells without interfacial layer (Al only), with interfacial layer of LiF, CuO_x, CuO_x/LiF, and LiF/CuO_x. Note that the device characteristics are monitored with increasing storage time for the same device.

4.2.3.3 Device lifetime improvement by CuO_x

To check if the rapid degradation of the devices without CuO_x interfacial layer was due to the degradation of organic materials, the substrates with an organic active layer (ITO/PEDOT:PSS/P3HT:PCBM) were first exposed to air for 1~2 days. LiF and Al layers were then deposited, immediately followed by device characterization. In this case the devices still have relatively good performance, which implies that device

lifetime depends most on the cathode interface stability. Fig.4.5 shows the changes of PCE, J_{sc}, V_{oc}, and *FF* as a function of storage time in air for devices with and without interfacial layers. For all devices, no extra package or encapsulation was used. For devices without CuO_x layer, a dramatic decrease of PCE is observed as the storage time increases; after ~2 h PCEs is reduce to around 50% of its initial values, mainly because of the reduction in J_{sc}. For the devices with CuO_x interfacial layer, on the other hand, an initial 40% increase of PCE is observed due to the increase of V_{oc} and FF after air exposure for several hours. The increase in V_{oc} and FF may result from the further oxidation of CuO_x in air, which can increase the shunt resistance as well as reduce the quenching of excitons and/charge carriers at the metal cathode. The device reserves nearly 80% of its initial PCE after 240 hours of air exposure, and ~50% after about 500 hours. Compared to our previously reported devices with a CrO_x interfacial layer, the devices with a CuO_x have lower initial efficiency, but exhibit better stability. We found that applying a CuO_x/LiF interfacial bilayer structure can significantly increase the V_{oc} and FF of the CuO_x modified devices, leading to an improved PCE. This suggests that LiF may help improve charge extraction as well as reduce V_{oc} loss at the cathode/oxide/organics interface due to non-ideal energy level alignment. More importantly, the devices with a CuO_x/LiF interfacial bilayer still have higher stability, remaining 50% of their initial efficiency after ~250 h of exposure to air, making them even more stable than P3HT:PCBM BHJ devices with a CrO_x interfacial layer.

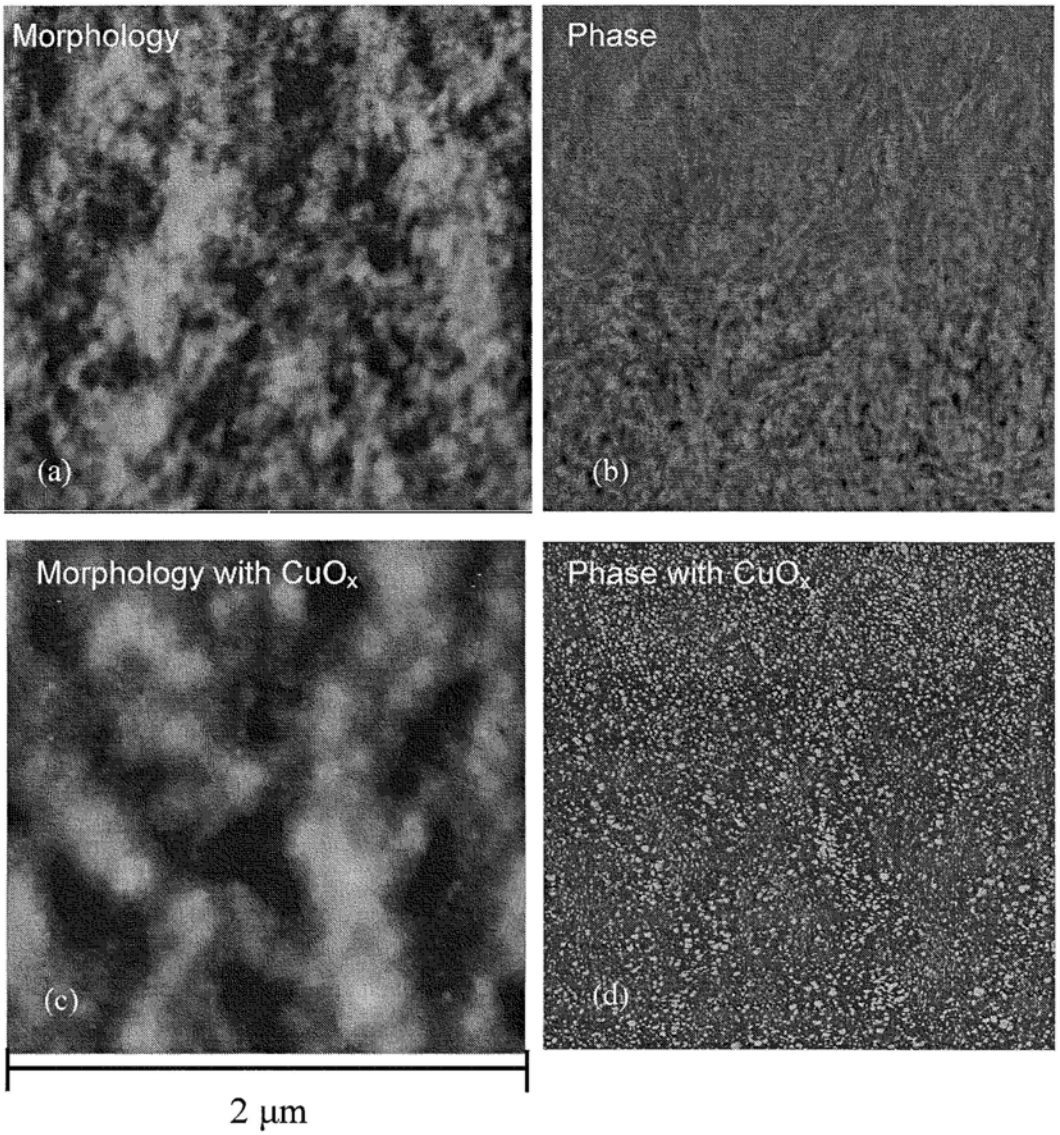

Fig.4.6 AFM image of morphology (a, b) without interfacial layer and (c, d) with 5 nm CuO_x films on the active layer of P3HT:PCBM.

Fig.4.6 shows the AFM topography and phase images of P3HT:PCBM blend thin film before (Fig.4.6 a, b) and after (Fig.4.6 c, d) deposition of CuO_x. No grains or particles are observed on the pristine P3HT:PCBM surface, a typical amorphous structure. By contrast, the surface after deposition of CuO_x presents particles (presumably CuO_x aggregates) around ~20 nm, which is smaller than that of CrO_x

particles on P3HT:PCBM. Unlike the CrO_x, CuO_x particles are not uniform and do not compactly cover the organic active layer. However, this CuO_x layer should reduce direct contact between organic materials and Al, and therefore affect the initial growth of Al layer.

4.2.3.4 Comparison between CrO_x and CuO_x

Compared to P3HT:PCBM devices with CrO_x, the P3HT:PCBM devices with CuO_x exhibit a lower initial efficiency due to its lower V_{oc}. This is possibly caused by the different energy levels between CrO_x (Cr_2O_3 has a CB minimum of 4.0 eV and VB maximum of 7.4 eV [4]) and CuO_x (Cu_2O has a CB minimum of 4.2 eV and VB maximum of 6.4 eV [4]). Another likely possibility is the diffusion of un-oxidized Cu, which has a high workfunction (4.6 eV [12]), into the organic active layer. Similarly to CrO_x, insertion of a CuO_x interfacial layer at cathode can also significantly improve the stability of P3HT:PCBM solar cells; in fact, the CuO_x modified devices are even more stable than those with a CrO_x interfacial layer. This is in agreement with our proposed mechanism for cathode degradation and stability improvement. Since the oxidation products of Cu have higher conductivities than those of Cr and Al, the oxidation of the CuO_x interfacial layer during air exposure will cause much less increase in the series resistance of the solar cells. The oxidation of the Cu first leads to formation of Cu_2O with a bandgap of ~2 eV [4], which can then be further oxidized into CuO with a bandgap of 1.5 eV [13]. Both oxides exhibit decent charge transport properties, therefore the CuO_x/Al can be more stable than CrO_x/Al in air, leading to

the slower degradation of the CuO_x devices in air. As we know, the chromium is not so friendly to human body, one of chromium oxide containing Cr^{+6} is toxic. However, the Cr^{+6} and Cr^0 are non-toxic. Using CrO_x to understand the physics of how cathode modification to improve device performance and stability is good. For the future large scale use of organic solar cells, other metal oxide such as CuO_x with similar function can be a good substitute.

In summary, we have shown that insertion of a thin layer of thermally evaporated CuO_x between the organic active layer and the Al cathode can greatly extend the lifetime of P3HT:PCBM based BHJ solar cells. The CuO_x exhibits good electron transport properties; but more importantly, it prevents formation of a thick organic-Al interdiffusion area by reducing the penetration of evaporated Al into the organic active layer. This leads to a more air-resistive cathode/organic interface and eventually improved device stability. We further demonstrated that application of a CuO_x/LiF interfacial bilayer can increase the power conversion efficiency of devices while still ensuring good air stability.

4.3 Stability improvement in MEHPPV:PCBM cells by CrO_x

4.3.1 Introduction of MEHPP:PCBM

Poly para-phenylenevinylene (PPV) and its derivatives are widely studied in OLEDs and OPVs due to its prosperous luminescence and semiconducting property. In family of PPVs, poly (2-methoxy-5-(2′ -ethylhexyloxy)-1,4-phenylenevinylene

(MEH-PPV) exhibits characteristics such as high solubility that make it particularly favorable for fabrication of BHJ organic solar cells [14-17]. The MEHPPV:PCBM solar cells have been fabricated by various groups, and the highest efficiency of 2.9% was achieved by G. Yu *et al.* in 1995 [18]. The ability to finely control the morphology of MEHPPV:PCBM to form an interpenetrated network is crucial for high device performance [18-19].

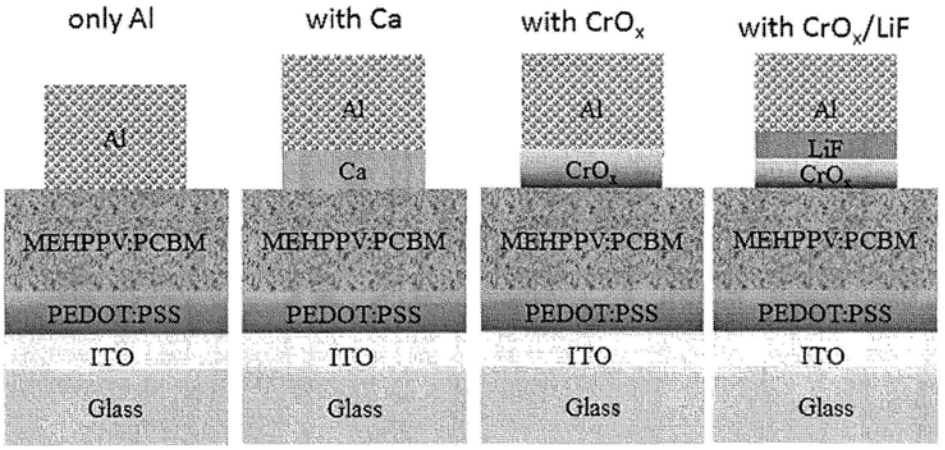

(a)

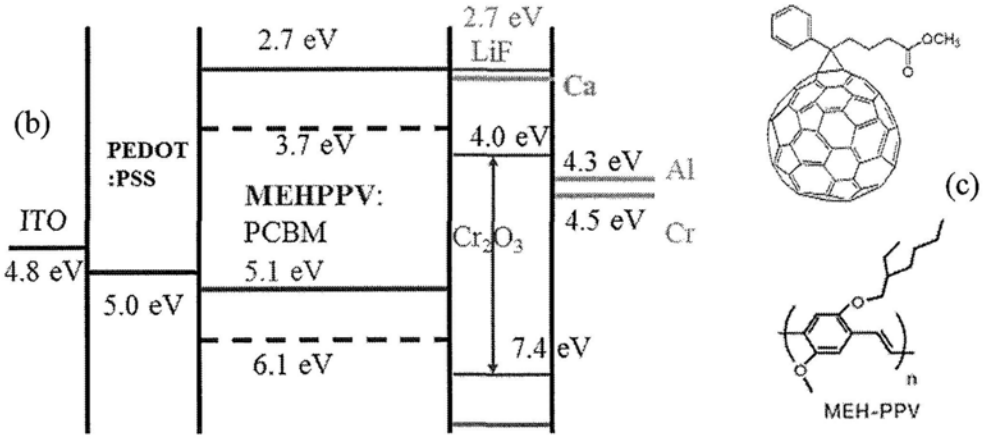

Fig. 4.7 (a) Device structure of MEHPPV:PCBM solar cells with different cathode interfacial layers (b) energy levels and (c) molecules structure of MEHPPV and PCBM.

4.3.2 Experimental details

The device structures and energy diagram of MEHPP:PCBM based solar cells are shown in Fig.4.7. Chlorobenzene solutions of MEHPPV (10 mg/mL) and PCBM (20 mg/mL) were first prepared separately. They were then mixed together with a weight ratio of MEHPPV:PCBM 1:4. The thickness of the photoactive layer was approximately ~90 nm. The Ca interfacial layer was deposited by thermal evaporation of Ca metal under a deposition pressure of ~1.5×10-4 Pa, with a deposition rate of 0.4-0.6 Å/s. The other detailed procedures for device fabrication and measurement are the same as these for P3HT:PCBM BHJ solar cells.

4.3.3 Results and discusses

4.3.3.1. Influence of cathode interfacial layers on performance

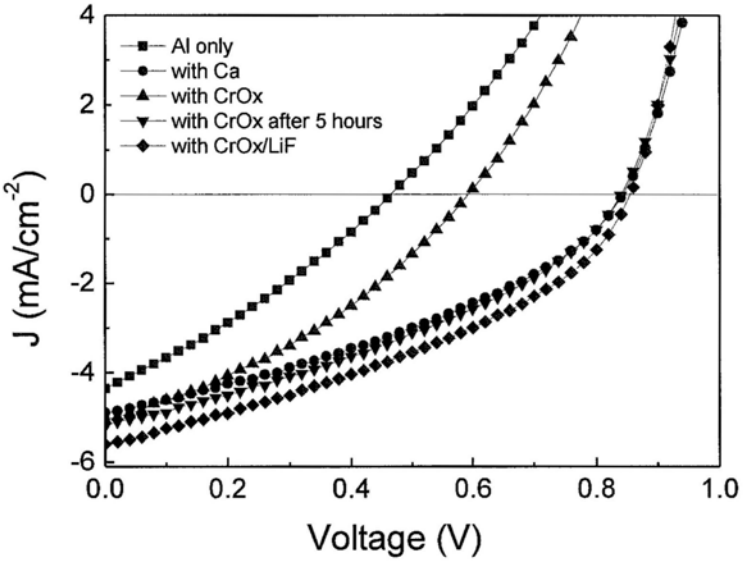

Fig.4.8 *J-V* characteristics of MEHPPV:PCBM based solar cells with different cathode interfacial layers under illumination.

Table 4.2 Initial parameters of MEHPPV:PCBM OPVs with interfacial layers

Sample	PCE (%)	V_{oc}(V)	J_{sc} (mA/cm^2)	FF
Al only	0.61	0.46	4.36	0.3
with Ca	1.5	0.84	4.9	0.37
with CrO_x	1.05	0.6	5.1	0.34
with CrO_x (5h)	1.6	0.84	5.2	0.37
with CrO_x/LiF	1.8	0.86	5.6	0.38

Note that the sample with CrO_x (5h) is the device with a CrO_x cathode interfacial layer after exposure to air for 5 hours.

Fig. 4.8 shows the *J-V* characteristics of MEHPPV:PCBM devices without and with cathode interfacial layers under illumination. The parameters of merit for all the devices are listed in Table 4.2. The MEHPPV:PCBM based devices without interfacial layer (Al only) had a PCE of 0.61% mainly due to its lower V_{oc} of 0.46 V. Ca, a low workfunction metal (~2.8 eV) can effectively improve this device's efficiency to 1.5%, with V_{oc} increasing to 0.84 V. These values are similar to the one reported by others [20-21]. Devices with CrO_x exhibit a PCE of 1.05% with V_{oc} of 0.6 V, while the performance gradually increases to 1.6%, with V_{oc} of 0.84 V after 5 hours of exposure to air. The reason for such improvement will be discussed later. In contrast, devices with a CrO_x/LiF interfacial bilayer showed a high initial PCE of 1.8% and V_{oc} of 0.86 V. By comparison, it is found that device performance is significantly improved by inserting an interfacial layer of either Ca or CrO_x, particularly the CrO_x/LiF interfacial bilayer.

4.3.3.2. Degradation of MEHPPV:PCBM solar cells

One major problem associated with the application of polymer is its instability in

air and under illumination, degrading its electric properties. The light induced degradation of MEHPPV:PCBM has been studied. Under irradiation in air, a decrease of the intensity of light absorption (half-life is about 30 hours) accompanied by a blue shift was observed, which is mainly due to the oxidation of ether substituent followed by the oxidation of double bonds, and if well protected from oxygen, MEHPPV:PCBM active layer could be photochemically stable for several years under illumination [22-24]. Our work, however, will primarily investigate the degradation of the cathode interface in air.

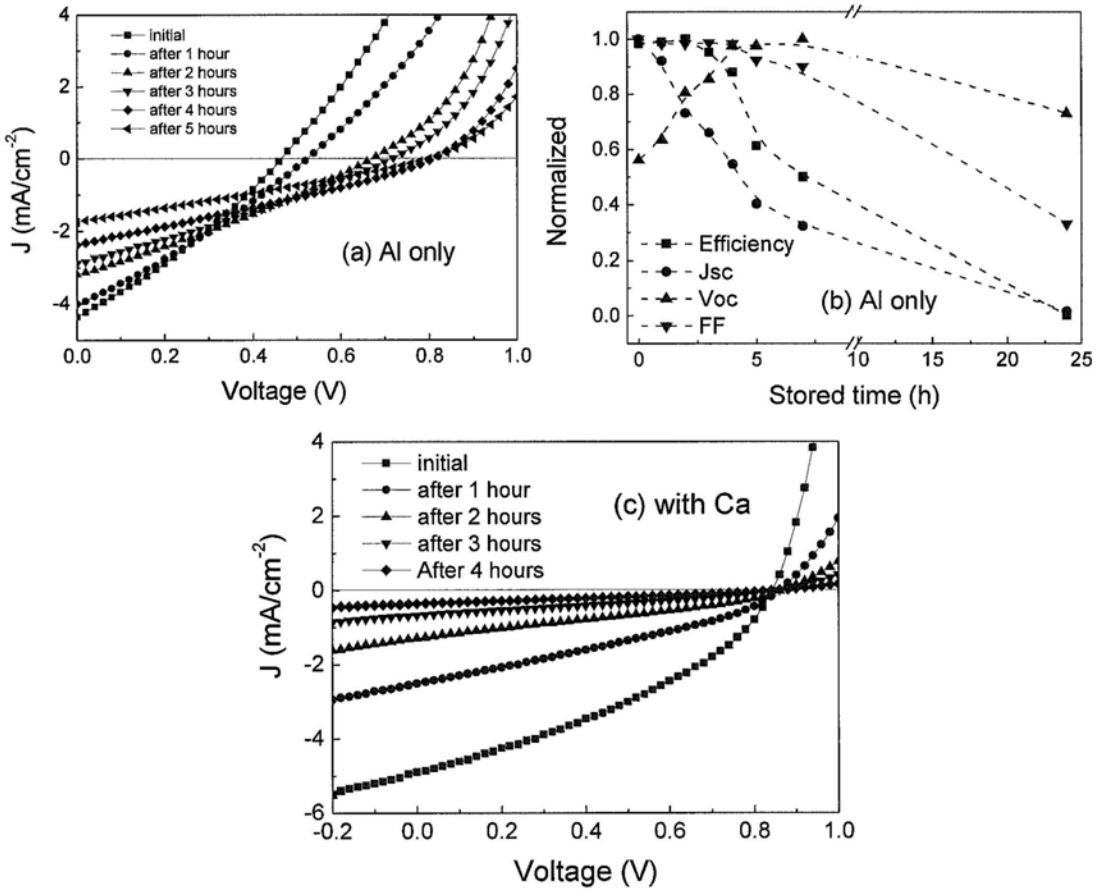

Fig.4.9 *J-V* characteristics of MEHPPV:PCBM solar cells (a) without any interfacial layer (Al only), (b) PCE, J_{sc}, V_{oc} and FF with stored time in air in device without any interfacial layer (Al only) and (c) with Ca under illumination.

Fig.4.9 shows the degradation of MEHPPV:PCBM based devices without a interfacial layer and with a Ca interfacial layer. Devices with a Ca interfacial layer degraded rapidly, retaining less than 50% of their initial PCE after an hour air exposure, mainly due to the oxidation of Ca to CaO or $Ca(OH)_2$ in air, which behaved like an insulator and blocked charge transport at the cathode interface. In contrast to P3HT:PCBM OPV, MEHPPV:PCBM based devices without any interfacial layer (Al only) still kept their initial PCE in the first 2 hours and has ~50% of its initial PCE after 7 hours. Interestingly, the V_{oc} gradually increased while the J_{sc} and FF monotonously decreased after exposure to air for first several hours. The unexpected increase of V_{oc} and FF may partially result from the relatively slower growth of an charge blocking layer at organic/Al interface, which reduces the charge extraction, and increases the shunt resistance. Therefore, it is possible that the MEHPPV:PCBM devices without any interfacial layer exhibited decreasing J_{sc} and increasing V_{oc} and FF during initial exposure to air because the charge blocking layer grew at a sufficiently low rate. Another possibility stems from observations that adding more PCBM to PPV thin films, particularly PCBM particles on top surface, increases their stability because the hardness of the PCBM can reduce the diffusion of Al into the organic active layer [25-27]. It is reported that PPV:PCBM is much stable than the pure PPV thin films. For these reasons, PPV:PCBM blends with a higher concentration of PCBM may provide better device stability.

4.3.3.3. Stability improvement in MEHPPV:PCBM OPV by CrO_x

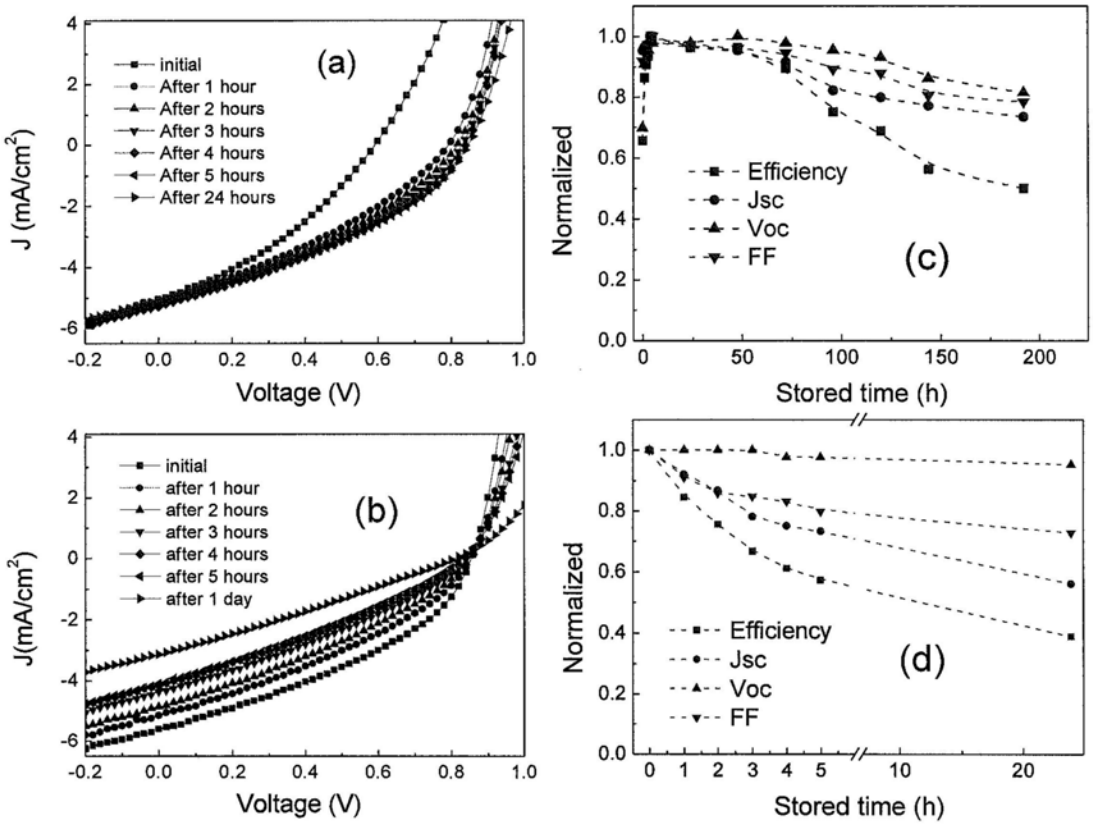

Fig.4.10 *J-V* characteristics of devices with (a) CrO_x and (b) CrO_x/LiF interfacial bilayer under illumination, PCE, J_{sc}, V_{oc} and FF in devices of devices with (c) CrO_x and (d) CrO_x/LiF interfacial bilayer, as a function of storage time in air.

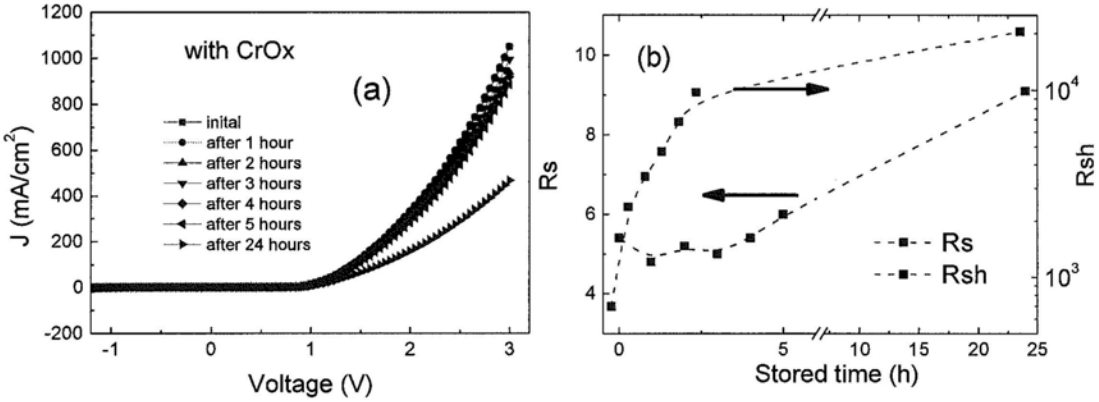

Fig.4.11. (a) Dark *J-V* characteristics of MEHPPV:PCBM devices with CrO_x, (b) series resistance R_s and shunt resistance R_{sh} as a function of storage time in air.

Insertion of a CrO_x layer between the organic active layer and Al cathode can greatly improve the device stability of MEHPPV:PCBM solar cells. The degradation of MEHPPV:PCBM devices with CrO_x and CrO_x/LiF interfacial bilayer are shown in Fig.4.10. For the device with CrO_x, the intial PCE is low but gradually increases due to the increase of its V_{oc} and FF; J_{sc} appears to be stable. Fig.4.11 (a) shows the dark *J-V* characteristics of devices with CrO_x, the shunt resistance and series resistance were extracted from the dark current at 0 V and 1.2 V, respectively. Since a shunt resistance of over 3000 $\Omega\,cm^{-2}$ is necessary to obtain high V_{oc} in solar cells, the increase of V_{oc} and FF in device with CrO_x are mainly attributed to the gradual increases of shunt resistance, from the initial value of 694 $\Omega\,cm^{-2}$ to the one 20,000 $\Omega\,cm^{-2}$ when exposed to air, as shown in Fig.4.11(b). At the same time, the series resistance changes little upon air exposure, indicating that no charge blocking layer is formed and that the charge extraction at the cathode interface remains efficient. In contrast, devices with a CrO_x/LiF interfacial bilayer have a higher initial efficiency, but the J_{sc} and FF drop in air, leading to the decrease of efficiency during air exposure, although this decrease occurs at a much slower rate than those for devices without an interfacial layer or with a Ca interfacial layer. MEHPPV:PCBM cells with a CrO_x/LiF interfacial bilayer can still have better V_{oc} stability, comparable to that of P3HT:PCBM solar cells. We believe this is related to the different morphologies of the two systems, as will be discussed in the following section.

4.3.3.4 Comparison of the impacts of CrO_x in P3HT:PCBM and MEHPPV:PCBM systems

Similarly to P3HT:PCBM system, the cathode degradation plays a crucial role in the degradation of MEHPPV:PCBM BHJ solar cells. As expected, inserting a CrO_x interfacial layer between the organic active layer and Al cathode reduces the penetration of evaporated Al into MEHPPV:PCBM layer, which prevents the formation of a thick organic-Al interdiffusion area between the active layer and cathode, and thus greatly improve the device stability. Different from P3HT:PCBM devices, the MEHPPV:PCBM devices with a CrO_x interfacial layer exhibit a low initial efficiency due to its low V_{oc}, and the V_{oc} then gradually increases to ~0.84 V when exposed to air. Also, the increase of V_{oc} is observed to be accompanied by an increase of shunt resistance. We note that the two blend systems have very different morphologies. For the MEHPPV:PCBM system, due to the greater phase separation and higher volume ratio of PCBM a rougher top surface is formed with presence of PCBM agglomerates [14-15, 25]. This results in formation of defects and grain boundaries, where metal atoms can diffuse into during cathode deposition, leaving behind leakage current paths. As a result, the shunt resistance of fresh MEHPPV:PCBM devices (694 Ω cm^{-2}) is much smaller than that of the fresh P3HT:PCBM devices (3300 Ω cm^{-2}). After being exposed to air for a couple of hours the metal filaments (leakage paths) in MEHPPV:PCBM devices can slowly be oxidized, leading to an increased V_{oc}. We believe this is the main reason that causes the different degradation behaviors of MEHPPV:PCBM and P3HT:PCBM devices.

In summary, the stability of MEHPPV:PCBM based solar cells is largely affected by their cathode interface degradation. Inserting a CrO_x layer between the organic active layer and Al cathode can greatly improve the device stability. CrO_x/LiF interfacial bilayer can effectively improve the efficiency of MEHPPV:PCBM BHJ solar cells.

4.4 Stability improvement in CuPc/C_{60} cells by CrO_x

4.4.1 Introduction of CuPc/C_{60} solar cells

Two common types of organic solar cells are, polymer based and small molecule based OPVs. Copper phthalocyanine (CuPc/C_{60}) solar cells are one of the most successful bilayer small molecule based solar cells [29-30]. The configuration of a bilayer solar cell, as well as the molecule structures of CuPc, C_{60}, and (Bathocuproine) BCP the most used exciton blocking layer (EBL) in small molecule solar cells are shown in Fig.4.12. Small molecule solar cells are commonly fabricated by thermal evaporation of small molecules. It should be noted that purity is crucial for device efficiency, and the source materials are usually purified under vacuum or nitrogen condition for several times before the growth of a organic active layer by thermal evaporation. Efficiencies in bilayer OPV are further limited by the very short exciton diffusion length (L_D), e.g. 10 nm in CuPc and 40 nm in C_{60} [31-32].

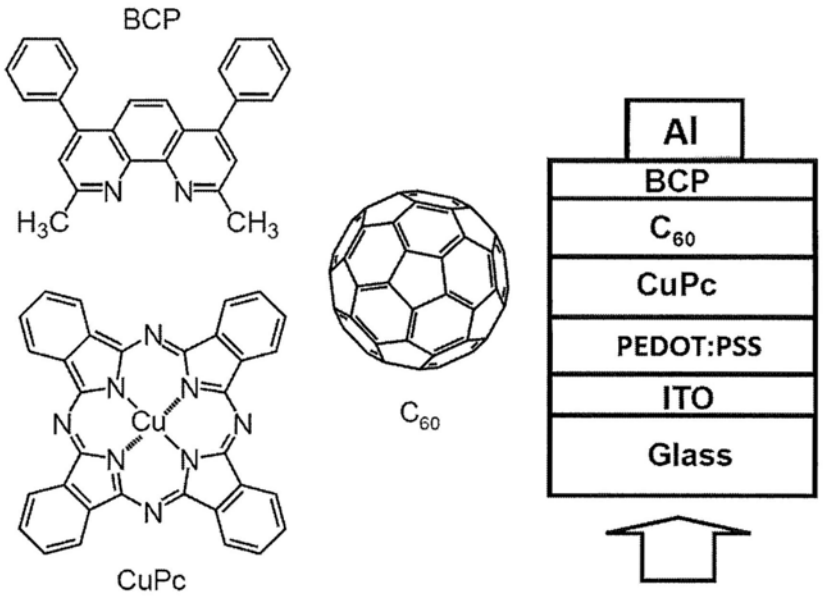

Fig.4.12 (a) Typical small molecules used in bilayer heterostructure organic solar cells; (b) device architecture with ITO anode, PEDOT:PSS hole transport layer, CuPc donor layer, C_{60} acceptor layer, BCP exciton blocking layer, and Al cathode.

4.4.2 Experimental details

The structure of CuPc/C_{60} solar cells is shown in Fig.4.12. For bilayer devices with CuPc/C_{60}, about 40 nm CuPc was first deposited at 100 °C. Then, 50 nm of C_{60} was deposited at 100 °C. A 15 nm interfacial layer of BCP was deposited at room temperature. ITO treatment, methods of PEDOT:PSS deposition, other cathode interfacial layers, and measurement techniques are the same as those in chapter 3.

4.4.3 Results and discusses

4.4.3.1 Influence of interfacial layers on performance

The *J-V* characteristics of our small molecule solar cells are shown in Fig.4.13, and the corresponding initial efficiencies, V_{oc}, FF, R_s, and R_{sh} are listed in Table 4.3. CuPc/C_{60} solar cells without any interfacial layer exhibit a PCE of 0.5%. Inserting a

BCP cathode interfacial layer can effective improve efficiency to ~0.7% by increasing J_{sc} and FF. The shunt resistance was defined as the slope of the dark *J-V* curve at 0 V and a series resistance defined as the slope at 1.2 V. Devices with a BCP interfacial layer also exhibited small series resistance and high shunt resistance. To check what limited the FF in our small molecule solar cells, we used the *J-V* curves of our device with BCP under illumination and under dark together to determine the collection length. The limited collection length in CuPc/C_{60} was calculated to be ~10 nm, which limits the collection efficiency to ~25%, leading to low performance. In contrast, studies by others reported a collection length as high as ~45 nm in CuPc:C_{60}, with corresponding efficiency 4%, a J_{sc} of 7 mA/cm^2, V_{oc} of 0.5 V, FF 0.65 [29-30]. Since we optimize the thicknesses and deposition temperature of CuPc and C_{60} layers, we tentatively attributed the low efficiency to the purity of the small molecules we used, which can reduce the quality of the organic active layers. Although the performance of our small molecule solar cells was not optimal, it should still allow our study on how cathode interfacial layers affect device stability in air.

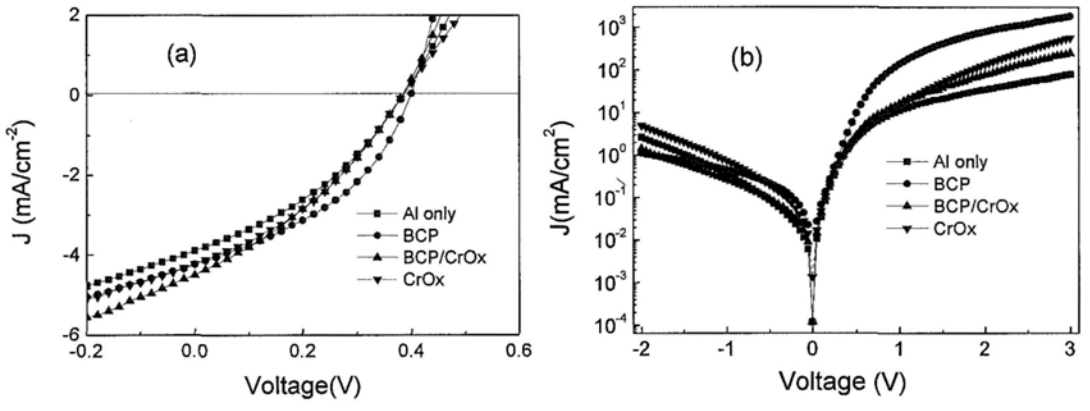

Fig.4.13 *J-V* characteristics of CuPc/C_{60} small molecule based solar cells with different cathode interfacial layers (a) under illumination and (b) in dark.

Table 4.3 Initial parameters of CuPc/C_{60} small molecule based OPV with interfacial layer

Sample	PCE	V_{oc}(V)	J_{sc} (mA/cm^2)	FF	R_s (Ω cm^{-1})	R_{sh}(Ω cm^{-1})
Al only	0.5%	0.38	3.8	0.35	46	7713
with BCP	0.7%	0.4	4.2	041	2.5	2733
with BCP/ CrO_x	0.7%	0.38	4.5	0.41	24	4889
with CrO_x	0.6%	0.38	4.2	0.38	13	3086

4.4.3.2 Degradation of CuPc/C_{60} solar cells

Fig.4.14 shows the degradation of CuPc/C_{60} solar cells without any interfacial layer and with a BCP interfacial layer in air. Since PCE is the product of J_{sc}, V_{oc}, and FF, the changes of each parameter over time are also shown in Fig.4.14. J_{sc} decreases monotonously in both devices, dropping to nearly zero after ~5 hours. V_{oc} in CuPc/C_{60} solar cells drops quickly as well, unlike the cases of polymer:PCBM solar cells. The J_{sc} and V_{oc} drops may be associated to degradation of the organic active layers or any of the three interfaces, including the ITO/PEDOT:PSS/CuPc anode interface, CuPc/C_{60} donor/acceptor interface, and C_{60}/Al interface at cathode. Degradation of CuPc/C_{60} interface and the upper C_{60} active layer has been previously studied. It is reported that the conductivity of a single C_{60} layer decreased by several orders of magnitude upon exposure to air, while exposure to N_2, Ar and He gases has no effect on the conductivity of C_{60} films [33-35]. In our study, however, it is shown that the degradation at the cathode interface affects the device efficiency the most.

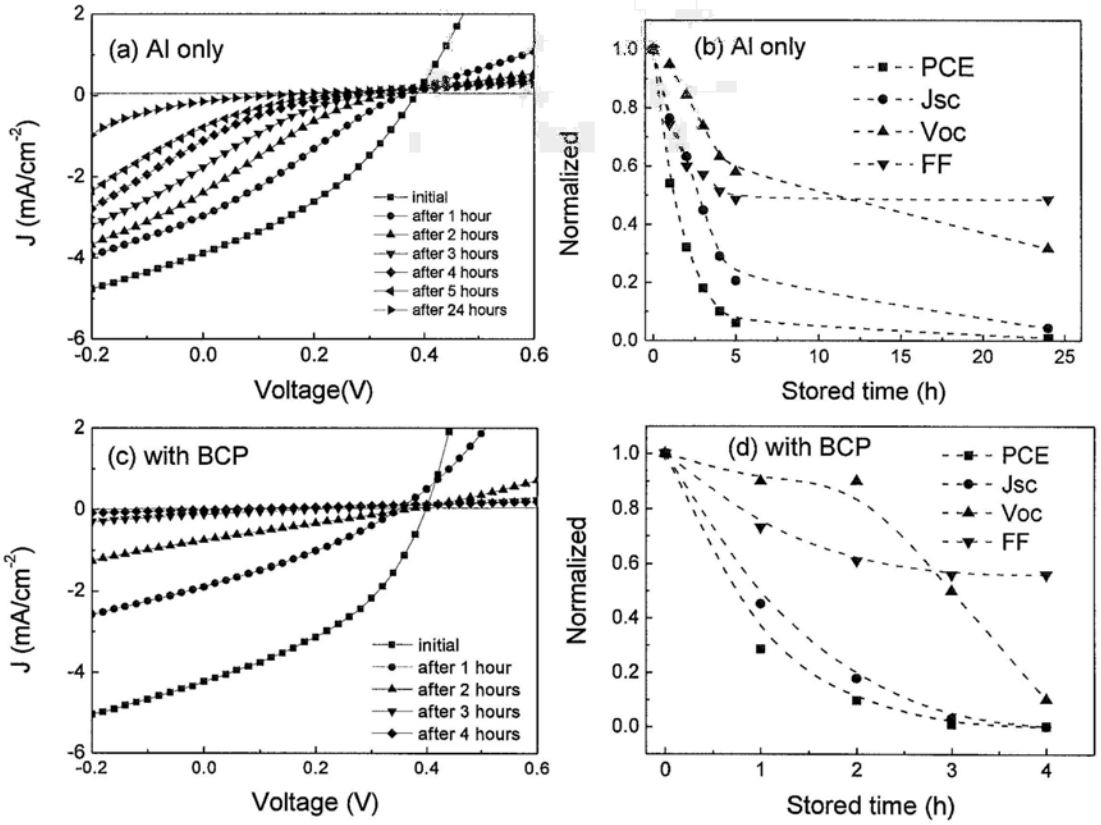

Fig.4.14 *J-V* characteristics under illumination in devices (a) Al only and (c) with BCP, PCE, J_{sc}, V_{oc} and FF in devices (b) Al only and (d) with BCP, as a function of storage time in air.

Devices with a BCP interfacial layer were observed to degrade faster in air than devices without any interfacial layer. It has been previously reported that CuPc/C_{60} solar cells lose 50% of their initial efficiency after 23 min of air exposure [35, 36], which is in agreement with our degradation data. Typically, BCP is one of the most widely used cathode interfacial materials in small molecule solar cells, and plays a very important role in blocking exciton transport. However, the lifetime of solar cells with BCP is very short. This is probably due to the instability of BCP in air, as it readily crystallizes in moist environments and forms numerous inner voids in the interfacial layer, which facilitate more oxygen and water diffusing into the organic/Al

contact or organic active layer, leading to an even more rapid decrease of J_{sc} [35-37]. BCP that is used to improve the electroluminescence efficiency in OLEDs also shortens the OLEDs' lifetime because of its instability in air [38].

Both the devices with Al-only contact and with BCP/Al contact degraded quickly in air, and they lost their initial PCE completely after ~5 hours. To check if the rapid degradation of the bilayer device was due to degradation of the organic materials, substrates with the organic active layer (ITO/PEDOT:PSS/CuPc/C_{60}) were first exposed to air for either 5 hours or 1 day. Al layer was then deposited, immediately followed by device characterization. In both cases the devices still had relatively good performance as shown in Fig4.15. However, the degradation rate of the CuPc/C_{60} active layer is still much faster than that of the P3HT:PCBM active layer. This indicates that the degradation at the CuPc/C_{60} interface and/or within C_{60} layer also plays an important role in device stability, although the initial fast decay of the devices is still dominated by the degradation at cathode/organic interface.

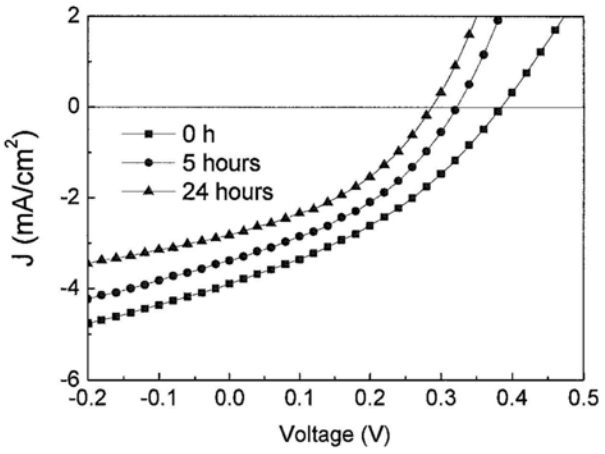

Fig.4.15 *J-V* characteristics of devices with active layers pre-exposed to air for 5 hours and 1 day under illumination.

4.4.3.3 Stability improvement by CrO_x

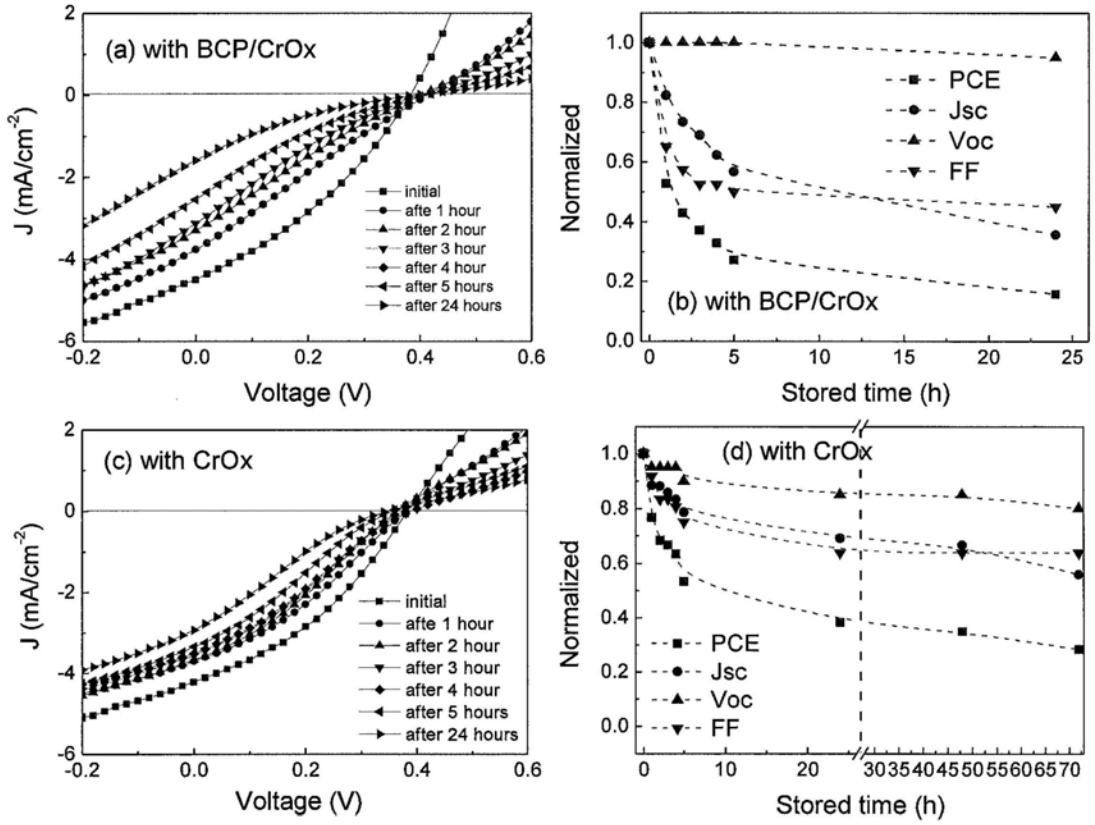

Fig. 4.16 *J-V* characteristics under illumination in CuPc/C_{60} solar cells with (a) CrO_x and (c) BCP/CrO_x interfacial bilayer, the PCE, J_{sc}, V_{oc} and FF in devices with (b) CrO_x and (d) BCP/CrO_x interfacial bilayer, as a function of storage time in air.

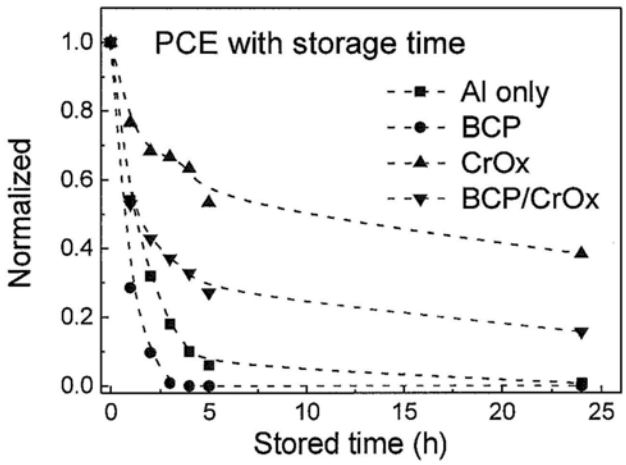

Fig.4.17 PCE in CuPc/C_{60} solar cells with different cathode interface layers as a function of storage time in air.

Fig4.17 shows the degradation of devices with a CrO_x layer inserted before the deposition of Al to form $C_{60}/CrO_x/Al$ and $BCP/CrO_x/Al$ contacts, respectively. Although the addition of CrO_x protect both devices to some extent, their degradation after the first several hours of air exposure were much more pronounced than the initial degradation of P3HT:PCBM and MEHPPV:PCBM solar cells. In devices with the $BCP/CrO_x/Al$ contact, the V_{oc} is very stable and the degradation is mainly due to the decrease of J_{sc} and FF caused by the degradation of BCP in air. It is possible that CrO_x can't wet the BCP surface well, and therefore an incomplete CrO_x film may form on the BCP surface, which would then reduce the effectiveness of the oxide protection layer. In devices with $C_{60}/CrO_x/Al$ contact, the stability is improved over 10 times, with the solar cells retaining 50% of its initial PCE after 5 hours and 30% after 72 hours. The degradation rate slowed down with increasing exposure time. The CrO_x can prevent formation of a thick organic-Al interdiffusion area by reducing the penetration of evaporated Al into the organic active layer. This leads to a more air-resistive cathode/organic interface. Unfortunately, oxygen and water molecules could still easily permeate through the thermally evaporated aluminum cathode or from lateral sides of the edges into the BCP and organic active layers, causing the degradation of the C_{60} layer and cathode interface. To summarize, we found that the most stable cathode contact is CrO_x/Al, followed by $BCP/CrO_x/Al$, C_{60}/Al, and BCP/Al, in order of decreasing stability.

4.4.3.4 Comparison between polymer-PCBM BHJ and small molecule bi-layer

Like polymer:PCBM BHJ solar cells, the cathode degradation plays an important role in CuPc/C_{60} small molecule bilayer solar cells. Insertion of a CrO_x interfacial layer at cathode can effectively improve the air stability of CuPc/C_{60} solar cells, however, their stability is much poorer than that of P3HT:PCBM devices. The degradation of conductivity in C_{60} layer, and the interface between CuPc and C_{60} may also play a great role in the device degradation in air. Compared to the polymer:PCBM BHJ structure, there are more grain boundaries in the small molecule double layer structure, which could facilitate diffusion of oxygen and water molecules into the organic active layer and therefore degrade the electronic properties of the materials.

In summary, we have shown that inserting a thin layer of thermally evaporated CrO_x between the CuPc/C_{60} active layer and Al cathode can effectively extend the lifetime of CuPc/C_{60} small molecule solar cells. As expected, the cathode interface degradation affects the stability of such devices the most, while the degradation of the organic active layer also impacts cell performance, even after effectively improving the stability at cathode interface.

4.5 Stability improvement in PFB:F8BT cells by CrO_x

4.5.1. Introduction of PFB and F8BT

The polymer-polymer blend of poly(9,9-dioctylfluorene-co-bis-N,

N′-(4,butylphenyl)-bis-N,N′-phenyl-1,4-phenylene-diamine) (PFB) and poly(9,9-dioctylfluorene-co-benzothiadiazole) (F8BT) (shortened as PFB:F8BT hereinafter) has been used to fabricate solar cells, with a maximum external quantum efficiency around 3% (a PCE of ~0.1%) at the wavelength of 550 nm [39-42]. F8BT is a green fluorescent polymer with ambipolar transport properties and exhibits electron and hole mobility of $\sim 10^{-3}$ cm^{-2} V^{-1} s^{-1} [43, 44], which is lower than that of PCBM. PFB has a hole transport mobility of around ~ 10^{-3} cm^{-2} V^{-1} s^{-1} [45], one order of magnitude lower than that of P3HT.

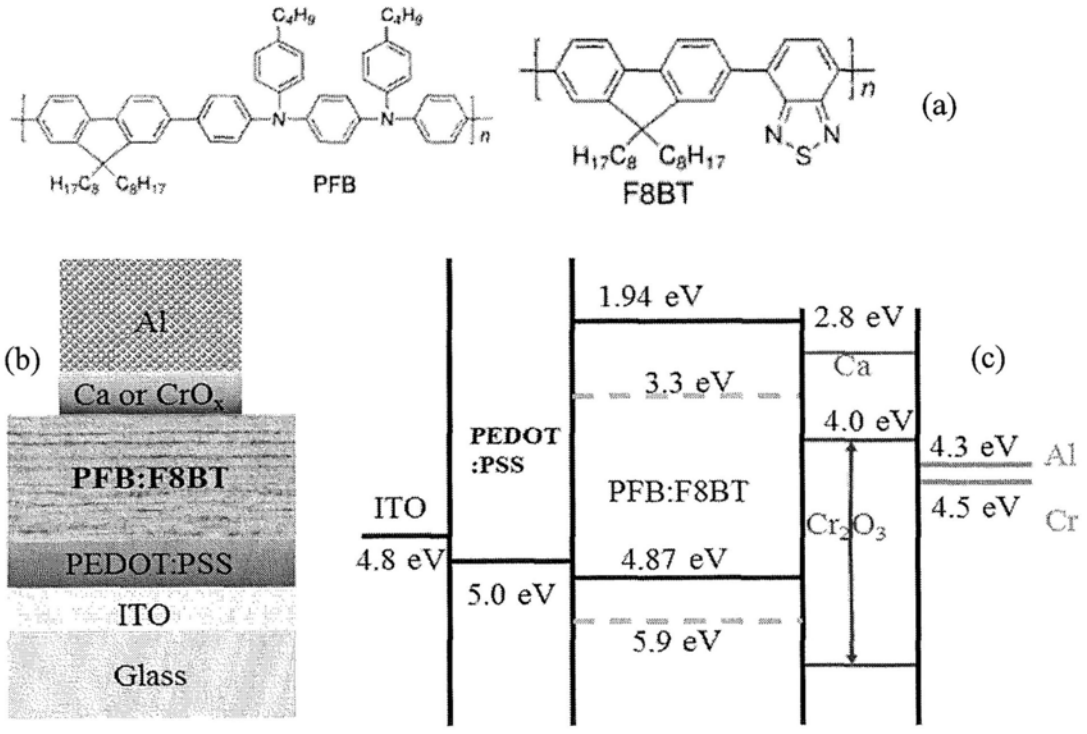

Fig.4.18 (a) Molecular structure of F8BT and PFB, (b) PFB:F8BT solar cells structure, and (c) energy diagram of different layers in devices.

4.5.2. Experimental details

The device structures of PFB:F8BT based solar cells are shown in Fig.4.18. The photoactive active layer was prepared by spincoating a mixed chloroform solution of PFB and F8BT, adding 0.6% p-xylene. The mixed solution had a PFB:F8BT weight ratio of 1:1 and a concentration of 15 gm/ml each. The thickness of the photoactive layer was approximately ~120 nm. The fabrication process and conditions were similar to those mentioned in reference [39-42]. ITO treatment, deposition of PEDOT:PSS, deposition of other cathode interfacial layers and measurement techniques were the same as these of other solar cells.

4.5.3 Results and discussions

4.5.3.1 Influence of cathode interfacial layers on performance

The performances of PFB:F8BT devices with cathode interfacial layers are shown in Fig.4.19, and the parameter of merits are listed in table 4.4. The device without any interfacial layer exhibits low efficiency due to low V_{oc}. The J_{sc} is comparable for all devices, regardless of cathode interfacial layer. The device with a Ca interfacial layer had a high efficiency of 0.15%, which is close to the value reported by others [39-42]. The extremely low J_{sc} in this kind of solar cells is most likely caused by inefficient charge separation due to recombination of tightly bound electron-hole pairs into neutral triplet [46].

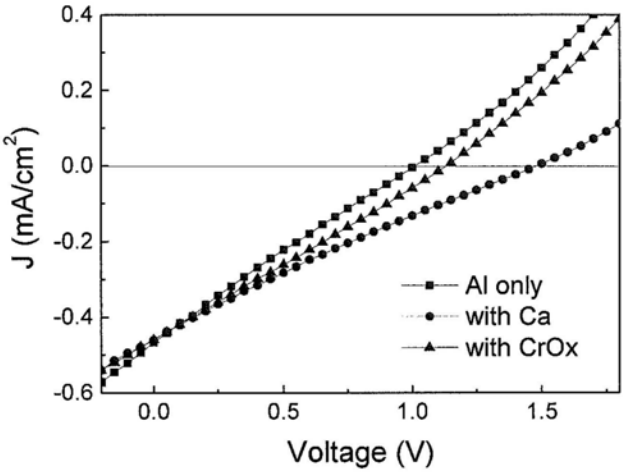

Fig.4.19 *J-V* characteristics of PFB:F8BT BHJ polymer solar cells under illumination.

Table 4.4 Initial parameters of PFB:F8BT polymer solar cells with interfacial layers.

Sample	PCE	V_{oc}(V)	J_{sc} (mA/cm^2)	FF
Al only	0.11%	1.05	0.46	0.23
with Ca	0.15%	1.45	0.46	0.22
with CrO_x	0.13%	1.2	0.46	0.24

4.5.3.2. Degradation of PFB:F8BT solar cells

The degradation of PFB:F8BT devices without any interfacial layer (Al only) and stored in the dark is shown in Fig.4.20. The devices lost most of their initial efficiency within an hour of air exposure, mainly resulting from the decrease of photo-current. The degradation is much faster than that of P3HT:PCBM, MEHPPV:PCBM, and CuPc/C_{60} solar cells. In contrast to these devices, the V_{oc} of PFB:F8BT devices also drops quickly. To check the unusually rapid decrease of V_{oc} and J_{sc}, the series resistance and shunt resistance were calculated as a function of storage time in the dark, as shown in Fig.4.20 (d). Interestingly, the dark current first

increases and then decreases, which is in agreement with the initial decrease of R_s as well as the re-increasing of R_s after ~2 hours. Same trend was also observed for the R_{sh}. Although the increase of R_s and R_{sh} after 2~3 hours can be explained by the formation of a charge blocking layer under the cathode, which would be in agreement with the degradation observed in other organic solar cells, we can't use the same mechanism to interpret the subsequent drop for both resistances. We also found similar rapid degradation in PFB:F8BT devices with Ca, as shown in Fig.4.21.

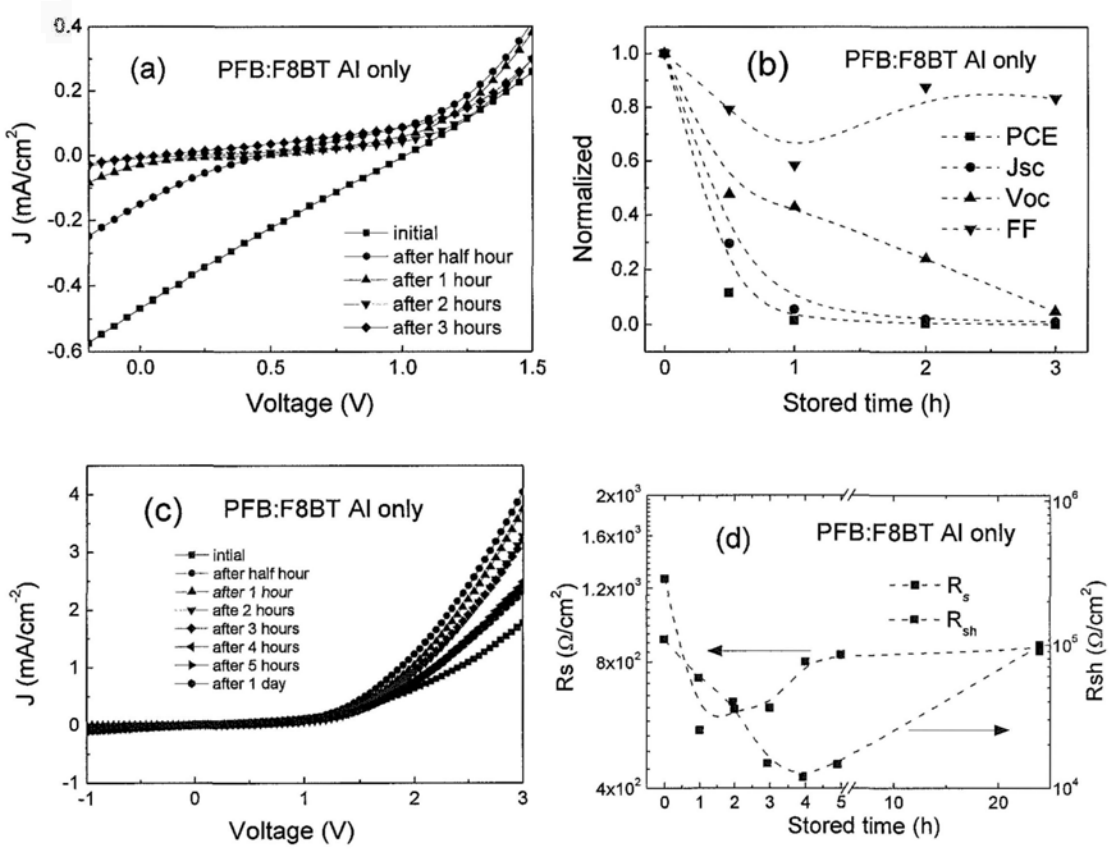

Fig.4.20 Characteristics of PFB:F8BT solar cells without any interfacial layer as a function of storage time in air (a) *J-V* under illumination, (b) degradation of PCE, J_{sc}, V_{oc} and FF, (c) *J-V* under dark, and (d) R_s and R_{sh}.

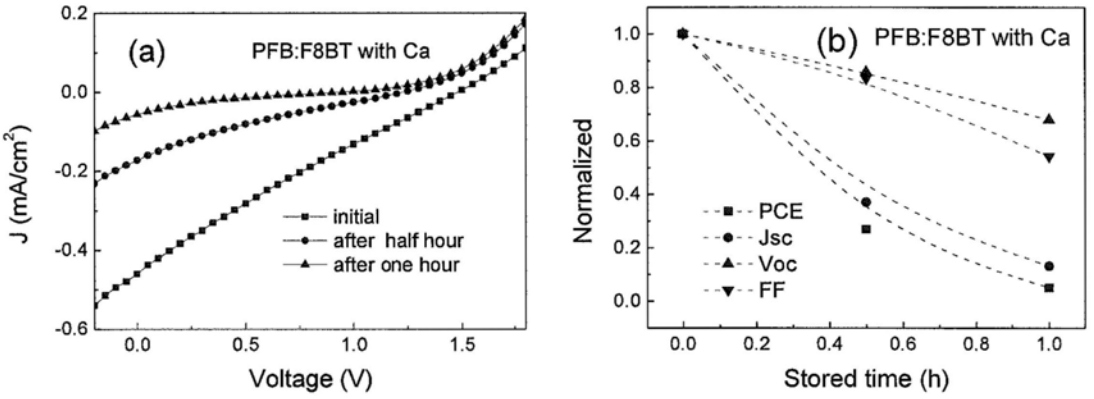

Fig.4.21. (a) *J-V* characteristics under illumination and (b) degradation of PCE, J_{sc}, V_{oc} and FF of PFB:F8BT solar cells with Ca interfacial layer as a function of storage time in air.

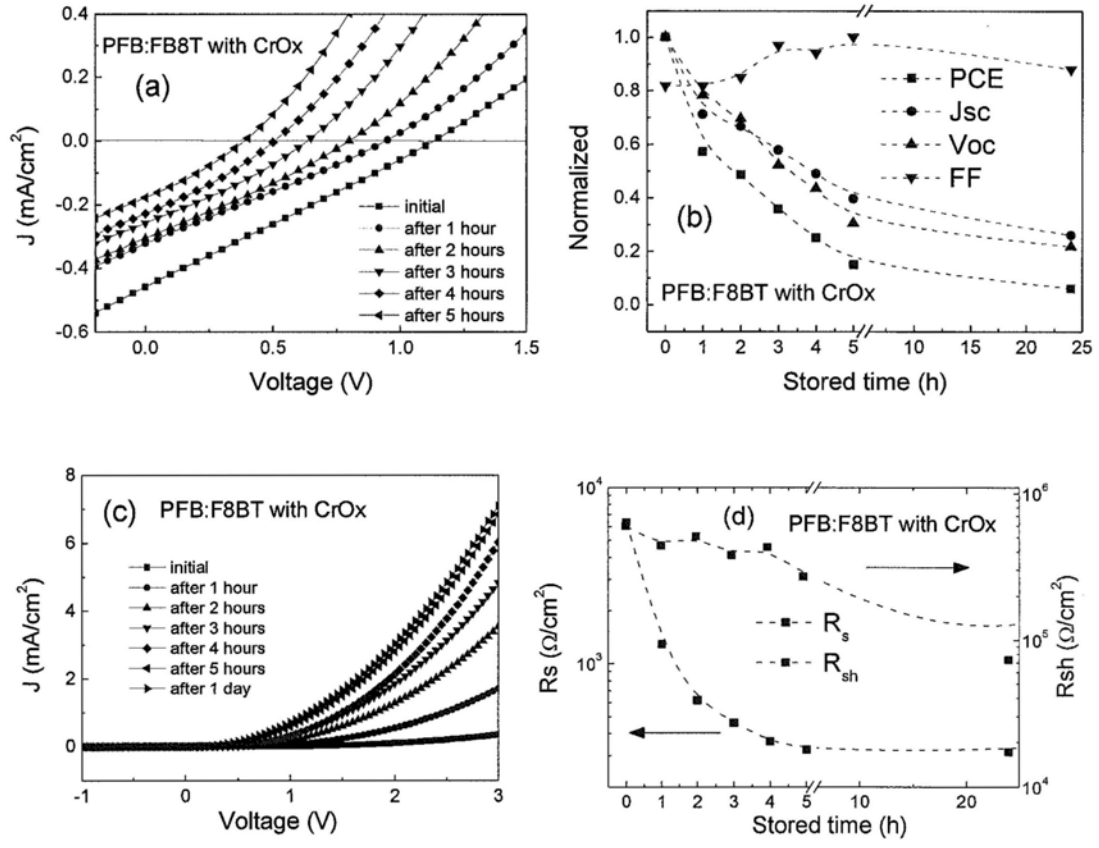

Fig.4.22 Characteristics of PFB:F8BT solar cells with CrO_x interfacial layer as a function of storage time in air (a) *J-V* under illumination (b) changes of PCE, J_{sc}, V_{oc} and FF, (c) *J-V* under dark, and (d) R_s and R_{sh}.

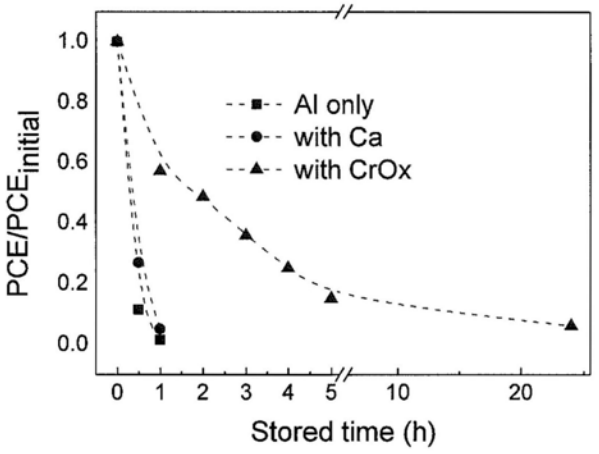

Fig.4.23 Comparison of device efficiencies as a function of storage time for PFB:F8BT solar cells Al only, and with Ca and CrO_x interfacial layers.

4.5.3.3 Stability improvement of PFB:F8BT cells by CrO_x

We also inserted a thin CrO_x layer between the Al cathode and the organic active layer to improve the lifetime of PFB:F8BT based solar cell. As shown in Fig.4.22, PFB:F8BT devices with a CrO_x layer maintained 50% of their initial efficiency after ~2 hours and 20% after 4~5 hours, upon air exposure. Decrease in both J_{sc} and V_{oc} significantly contribute to the decrease of the device efficiency. Although devices with CrO_x layer lasted over 5 times longer than devices without any interfacial layer or with a Ca interfacial layer, the relative improvement of stability in PFB:F8BT cells is much smaller than that of other organic solar cells we investigated. As can be seen in Fig.4.22 (c) and (d), the dark current monotonously increased in first 24 hours, which reduces the values of both R_s and R_{sh}. It is worth to mention that even after the dramatic decreasing process, the R_s of the devices remains to be large (~300 Ω/cm^2), rendering the FF and efficiency extremely low.

4.5.3.4 Comparison between polymer:PCBM blend and PFB:F8BT blend

The comparisons of device stability with different cathode interfacial layers are shown in Fig.4.23. CrO_x can improve the device stability of PFB:F8BT BHJ solar cells, but to a limited extent. Clearly, there are other degradation mechanisms that significantly contribute to the rapid failure of PFB:F8BT solar cells. Compared to other material systems studied previously, the PFB:F8BT system exhibits several distinct features of the device degradation. First, the V_{oc} drops quickly in PFB:F8BT solar cells both with and without a cathode interfacial layer. Second, the R_s decreases monotonically during the first several hours upon air exposure, (instead of increasing as it in other material systems). Third, the weak correlation between V_{oc} and R_{sh} indicates that the degradation of V_{oc} was not caused by leakage current. Now we shall discuss the mechanisms that cause these three features. In F8BT (including F8BT only, and F8BT:PFB and F8BT:TFB blends) based LEDs, an interfacial dipole layer adjacent to the anode contact (ITO\PEDOT:PSS), formed by deep-trapped holes and injected electrons under an electric field, has been observed to enhance hole injection into the F8BT domains [47]. This will largely reduce R_s as it boosts the holes current in F8BT network. On other hand, it is reported that the hole transport across the interface between PEDOT:PSS and PFB can be blocked due to electrochemical oxidation of the PFB molecules adjacent to the PEDT:PSS layer [48]. This process can be accelerated at presence of water and oxygen, and will greatly reduce hole extraction from PFB to the anode, which will thus greatly reduce photocurrent. Lastly the drop of V_{oc} can be understood using the equation $V_{oc} = \frac{nkT}{q} \ln(\frac{J_{ph}}{J_0})$, where J_{ph} is

the photocurrent, J_0 is the saturation current in device, n is the ideal factor, k is the Boltzman constant, and T is the temperature. In our previous organic solar cell systems, the decrease of J_{ph} is caused by the formation of charge blocking layer at the cathode interface, which at the same time also greatly reduces J_s, thus keeping the V_{oc} almost unchanged. In PFB:F8BT solar cells, however, the J_{ph} decreases dramatically because hole extraction in PFB is blocked, while J_s should remain at similar level since the hole injection in F8BT allows electron-hole recombination within the same phase and therefore avoids the formation of long-lived exciplex states. (This is also consistent with the initial drop of R_{sh}). As a result, V_{oc} will drop during degradation. To summarize, we propose that the enhancement of hole injection into F8BT and the reduction of hole transport across PFB/anode interface are the possible mechanisms that degrade the photovoltaic properties of PFB:F8BT BHJ solar cells, particularly in air. This would suggest that degradation process at the anode surface can affect the device stability as much as, or even more greatly than, that at the Al cathode interface. Therefore in PFB:F8BT BHJ solar cells degradation still occurs relatively fast even after the CrO_x modification at the cathode.

In summary, CrO_x can improve the stability of PFB:F8BT solar cells by reducing cathode degradation, but other degradation mechanisms, such as degradation in F8BT/anode and/or at the anode top surface, also play a comparable or more dominant role in the device degradation.

4.6 Summary of Chapter 4

In this chapter, we extend mechanisms of the Al cathode degradation and stability improvement to other oxide semiconductors and variety of organic solar cells.

It is shown that inserting a thin layer of thermally evaporated CuO_x between the organic active layer and the Al cathode can greatly extend the lifetime of P3HT:PCBM BHJ solar cells. The CuO_x exhibits good electron transport properties; Although, the Cu atoms can diffuse into the organic active layer, the oxidation products of Cu have higher conductivities than those of Cr and Al, the oxidation of the CuO_x interfacial layer during air exposure will cause much less electrical degradation. This leads to a more air-resistive cathode/organic interface and eventually improved device stability. We further demonstrated that application of a CuO_x/LiF interfacial bilayer can also increase the initial efficiency of devices while still ensuring good air stability.

Insertion of CrO_x as a cathode interfacial layer was observed to improve the stability of various organic solar cells, including the P3HT:PCBM and MEHPPV:PCBM blends, CuPc/C_{60} small molecule bilayer structure, and PFB:F8BT all polymer blend. However, the extent of the stability improvement varies for different systems. We found the degradation of the organic active layer significantly impacts the CuPc/C_{60} solar cell performance, and for PFB:F8BT BHJ solar cells degradation at the anode/active layer interface plays an important role in the overall device stability.

Reference:

[1] K. Kawano, C. Adachi, Appl. Phys. Lett. 96, 053307 (2010).

[2] J. Y. Kim, S. H. Kim, H. H. Lee, K. Lee, W. Ma, X. Gong, A. J. Heeger, Adv. Mater. 18, 572 (2006).

[3] M. D. Wang, Q. Tang, J. An, F. Xie, J. Chen, S. Zheng, K. Wong, Q. Miao, J. B. Xu, ACS Appl. Mater. Inter. 2, 2699 (2010).

[4] Y. Xu, M. A. A. Schoonen, Am. Mineral. 85, 543 (2000).

[5] S. Kim, K. Hong, K. Kim, I. Lee, J. Lee, J. KIEEME 23, 550 (2010).

[6] N. D. Hoa, S. Y. An, N. Q. Dung, N. V. Quy, D. Kim, Sens. Actuators B 146, 239 (2010).

[7] D. Wu, Q. Zhang, Phys. Rev. B 73, 235206 (2006).

[8] K. Han and M. Tao, ECS Trans. 25(15), 103 (2009).

[9] M. Yin, C.K. Wu, Y. Lou, C. Burda, J. T. Koberstein, Y. Zhu, S. Obrien, J. Am. Chem. Soc. 127, 9506 (2005).

[10] J. F. Moulder, W. F. Sticle, P. E. Sobol, K. D. Bomben, Handbook of X-ray Photoelectron spectroscopy, Physical Electronics, Inc, 1992.

[11] W. Zhao, Y. Guo, X. Feng, L. Zhang, W. Zhang, J. Zhu, Chin. Sci. Bull. 54, 1978 (2009).

[12] http://en.wikipedia.org/wiki/Work_function.

[13] H. J. Möller, Semiconductors for solar cells, Boston: Artech House, (1993).

[14] T. Martens, J. D'Haen, T. Munters, Z. Beelena, L. Goris, J. Manca, M. D'Olieslaeger, D. Vanderzande, L. De Schepper, R. Andriessen, Synthetic Metals, 138, 243 (2003).

[15] L. Zheng, Q. Zhou, X. Deng, M. Yuan, G. Yu, and Y. Cao, J. Phys. Chem. B, 108, 11921 (2004).

[16] C. J. Brabec, S. N. Sariciftci, Monatshefte für Chemie 132, 421 (2001).

[17] X. Y. Deng, M. Yuan, G. Yu, Y. Cao, J. Phys. Chem. B, 108, 11921 (2004).

[18] G. Yu, J. Gao, J. C. Hummelen, F. Wudi, A. J. Heeger, Science, 270, 1790 (1995).

[19] J. Peet, M. L. Senatore, A. J. Heeger, G. C. Bazan, Adv. Mater. 21, 1521 (2009).

[20] S. Alem, R. de Bettignies, and J.-M. Nunzi, Appl. Phys. Lett. 84, 2178 (2004).

[21] H. Z. Yu and J. B. Peng, Organ. Electron. 9, 1022 (2008).

[22] K. Norrman, S. A. Gevorgyan, and F. C. Krebs, ACS Appl. Mater. & Inter., 1, 102 (2009).

[23] A. Rivaton, S. Chambon, M. Manceau, J. -L. Gardette, N. Lemaître, S. Guillerez, Polym. Degrad. Stab. 95, 278 (2010).

[24] F. C. Krebs, J. E. Carle, N. Cruys-Bagger, M. Andersen, M. R. Lilliedal, M. A. Hammond, S. Hvidt, Sol. Energy Mater. Sol. Cells, 86,499 (2005).

[25] L. W. Barbour, R. D. Pensack, M. Hegadorn, S. Arzhantsev, and J. B.Asbury, J. Phys. Chem. C, 112, 3926 (2008).

[26] H. Hoppe, T. Gltzel, M. Niggemann, W. Schwinger, F. Schaeffler, A. Hinsch, M. C. Lux-Steiner, N. S. Sariciftci, Thin Solid Films, 511-512, 587 (2006).

[27] D. C. Coffey, O. G. Reid, D. B. Rodovsky, G. P. Bartholomew, and D. S. Ginger, Nano Lett. 7, 738 (2007).

[28] M. Jørgensen, K. Norrman, F. C. Krebs, Sol. Energy Mater. Sol. Cells, 92, 686 (2008).

[29] J. Xue, B. P. Rand, S. Uchida and S. R. Forrest, Adv. Mater. 17, 66 (2005).

[30] S. Uchida, J. Xue, B. P. Rand, and S. R. Forrest, Appl. Phys. Lett. 84, 4218 (2004).

[31] B. P. Rand, J. Genoe, P. Heremans and J. Poortmans, Prog. Photovolt: Res Appl. 15, 659 (2007).

[32] P. Peumans, A. Yakimov, S. R. Forrest, J. Appl. Phys. 93 3693 (2003).

[33] X. Xi, F. Li, Q. Meng, Y. Ding, J. Ji, Z. Shi, G. Li, Sol. Energy Mater. Sol. Cells, 94, 924(2010).

[34] R. Lessmann, Z. Hong, S. Scholz, B. Maennig, M. K. Riede, K. Leo, Organ. Electron. 11, 539 (2010).

[35] S. Heutz, P. Sullivan, B. M. Sanderson, S. M. Schultes, T. S. Jones, Sol. Energy Mater. Sol. Cells, 83, 229 (2004).

[36] Q. L. Song, M. L. Wang, E. G. Obbard, X. Y. Sun, X. M. Ding, and X. Y. Hou, C. M. Li, Appl. Phys. Lett. 89, 251118 (2006).

[37] Q. L. Song, F.Y. Li, H. Yang, H. R. Wu, X. Z. Wang, W. Zhou, J. M. Zhao, X. M. Ding, C. H. Huang, X. Y. Hou, Chem. Phys. Lett. 416, 42 (2005).

[38] B. W. D'Andrade, J. Esler and J. J. Brown, Synth. Metals, 156, 405 (2006).

[39] A. R. Campbell, J. M. Hodgkiss, S. Westenhoff, I. A. Howard, R. A. Marsh, C. R. McNeill, R. H. Friend, and N. C. Greenham, Nano Lett. 8, 3942 (2008).

[40] C. R. McNeill, S. Westenhoff, C. Groves, R. H. Friend, and N. C. Greenham, J. Phys. Chem. C, 111, 19153 (2007).

[41] H. Yan , S. Swaraj, C. Wang , I. Hwang, N. C. Greenham,C. Groves, H. Ade , and C. R. McNeill, Adv. Funct. Mater. 20, 4329 (2010).

[42] R. A. Marsh, C. R. McNeill, A. Abrusci, A. R. Campbell, and R. H. Friend, Nano Lett., 8, 1393 (2008).

[43] M. Voigt, J. Chappell, T. Rowson, A. Cadby, M. Geoghegan, R. A. L. Jones and D. G. Lidzey, Organ. Electron., 35(2005).

[44] T. Kreouzis, D. D. C. Bradley and A. J. Campbell, Proc. SPIE 5214, 141 (2004).

[45] T. -W. Lee, M. -G. Kim, S. Y. Kim, S. H. Park, O. Kwon, T. Noh, and T. -S. Oh, Appl. Phys. Lett. 89, 123505 (2006).

[46] S. Westenhoff, I. Howard, J. M. Hodgkiss, K. R. Kirov, H. A. Bronstein, C. K. Williams, N. C. Greenham, R. H. Friend, J. Am. Chem. Soc., *130*, 13653 (2008).

[47] A. J. A. B. Seeley, R. H. Friend, and J. -S. Kim, J. Appl. Phys., 96, 7643 (2004).

[48] J. -S. Kim, P. K.H. Ho, C. E. Murphy, A. J. A. B. Seeley, I. Grizzi, J. H. Burroughes, R. H. Friend, Chem. Phys. Lett., 386, 2 (2004).

Chapter 5

Limit of V_{oc} in polymeric BHJ cells predicted by a Double-Junction model

Overview

For further understanding the physics of cathode modification on device performance, we study the limit of the open-circuit voltage (V_{oc}) in polymer BHJ solar cells using a double-junction model, in this Chapter. We firstly give the introductions of the mechanisms of limitation to V_{oc}, the negative capacitance of solar cells measured by impedance spectroscopy, and the phase separation in organic BHJ solar cells. Then, the non-ideal structure of phase separation in a P3HT:PCBM blend are characterized by AFM, XPS and UPS, based on which a double-junction model is proposed for the BHJ solar cell structure and its limits on V_{oc} is described. Impedance spectroscopy in combination with transient photovoltage measurements are employed to investigate this model. A negative capacitance behavior and its relation to V_{oc} is observed in different BHJ systems, including P3HT:PCBM devices with different cathode interfacial layers, as well as MEH-PPV:PCBM and PFB:F8BT based devices. Our results suggest that the V_{oc} is determined by the junction with the smaller negative capacitance onset and that the cathode modification can tune the V_{oc} maximum from the Schottky junction limited regime to the donor/acceptor junction limited regime. Transient photovoltage measurements also support the two-junction model in the investigated BHJ systems.

5.1. Introduction

5.1.1 Introduction of the limits of open-circuit voltage

The power conversion efficiencies (PCE) of solar cells are determined by the open-circuit voltage V_{oc}, the fill factor (FF), and the short-circuit density J_{sc}. The physics understanding and optimization of V_{oc} play an important role in increasing efficiency. To date, significant progress has been made to derive the upper limits of the efficiency with empirical arguments related to the origin of the V_{oc} in polymer based solar cells.

Since photons are converted into electricity, fundamental losses should be taken into account and it should be possible to derive an upper limit of V_{oc} on factual devices. In 1961, Shockley and Queisser found that for single absorber materials [1], the upper limit of V_{oc} could be described as , $V_{oc} = E_g(1-\frac{T_c}{T_s})$, E_g a band gap of the semiconductor material, T_c the temperature of the solar cells and T_s the temperature of the sun as a black body, based on the balance of absorption and emission of a solar cell. It is found that V_{oc} reaches a maximum value in the ideal case when the charges can only recombine through radiation.

Instead, in organic solar cells the V_{oc} was initially attributed to a built-in electric field from the workfunction difference between the anode and cathode, known as metal-insulator-metal (MIM) model [2, 3]. The origin of V_{oc} depends strongly on the cell architecture and the Fermi level pinning at organic/metal contact [3,4], a linear relation between the V_{oc} and metal workfunctions with a slope parameter of ~0.1 was observed by using Ca, Al, and Au as metal contact [2,4,5]. Alternative, V_{oc} is found to

be limited by the difference between the highest occupied molecular orbital energy of the donor ($HOMO_D$) and the lowest unoccupied molecular orbital energy of the acceptor ($LUMO_A$) [6-8]. However, it is also suggested that the interface recombination though both unimolecular and bimolecular mechanisms controls V_{oc} [9-11], or the recombination through trail states in polymer-fullerene solar cells [12]. The energetic losses between E_{CT} and V_{oc} are around ~0.6 eV, 0.25 eV of this loss is radiation recombination and however 0.35 eV due to the non-radiation recombination through CT states [13-14]. So far, there is still no full picture on limits of V_{oc}, considering both the MIM model and the $HOMO_D$-$LUMO_A$ model.

5.1.2 Introduction of the negative capacitance in impedance spectroscopy

Negative capacitance has been well observed in Si diodes [15], metal-oxide-semiconductor tunneling diodes [16], LEDs including organic and inorganic semiconductors [17], solar cells including polycrystalline Si [18], dye-sensitized solar cells [18], thin film CdS/CdSe solar cells [18], and organic solar cells [19]. Negative capacitance can be attributed to the minority carrier flow, slow transient time of injected carrier, dispersive charge transportation, charge trapping and both radiation and non-radiation recombination [15-20]. However, it has been shown that the negative capacitance in OLEDs is primarily caused by charge recombination of bipolar injection.

In a typical *C-V* characteristic with a negative capacitance, the capacitance first increases with forward bias, reaching a maximum point (maximum capacitance, C_{max}),

then decreases with some of them even reaching negative values. The increasing of capacitance is contributed to the injected charges, which increase the charge density at the organic active layer, e.g. electrons accumulate at PCBM (the acceptor) and holes at P3HT. With increasing of forward bias voltage, the junction capacitance (chemical capacitance) exponentially increases $C_j \propto e^{(-\frac{qV_a}{nkT})}$, where C_j is the junction (both Schottky and pn) capacitance, n the ideal factor of a diode, V_a the applied bias voltage, kT the room temperature energy [17]. At certain point, the electron-hole recombination under bipolar injection starts to prevail and can result into a negative capacitance, $C_r \propto \gamma C_g$, where C_r is the negative capacitance due to the recombination current, γ a parameter which increases with bias voltage, C_g the geometrical capacitance [17]. The total capacitance $C=C_j+C_r$ can reach a maximum point with increasing voltage, implying that a recombination pathway opens up at forward bias and therefore decreases the ability of charge accumulation in organic solar cells. Compared to PL and EL, the impedance spectroscopy with a negative capacitance can be more sensitive and useful to study the influence of recombination including radiation and non-radiation on V_{oc} in BHJ solar cells.

5.1.3 Introduction of phase separation in BHJ

Nanoscale phase separation and interpenetrated networks of donor and acceptor materials are crucial for the performance of BHJ devices. Lateral phase separation within ~10 nm can be reached in P3HT:PCBM blend systems [21-22], providing enough donor/acceptor interfaces for the excition dissociation. Besides, vertical phase

separation is also important, particularly along the top surface connected to the Al cathode. In an ideal BHJ structure, the acceptor material should be more prevalent at the cathode and the donor more prevalent at anode. However, it is reported that the donor materials are often undesirably accumulated on the top surface of polymer-fullerene blend systems [23], leading to a non-ideal vertical phase separation. Although an inverted structure can avoid this non-ideal distribution, it is still necessary to investigate the vertical phase separation to further understand the device physics in BHJ structure.

5.2 Experimental details

Electrical measurements were performed by a semiconductor characterization system (Keithley 236) under the spectral output from a solar simulator (Newport) using an AM 1.5 filter with a light power of 100 mW/cm^2. The top morphologies were observed by AFM in the taping mode. The capacitance measurements were performed with a Hewlett Packard 4284A impedance analyzer. The fixed frequency to measure capacitance-voltage was 1 kHz. The homemade setup for transient photovoltage measurement systems were detailed in chapter 2. The device structure and fabrication procedures have been described in chapters above.

5.3 Results and discussions

5.3.1 Vertical phase separation of P3HT:PCBM

Phase separation is crucial for the performance of devices. An AFM morphology image with its surface potential and phase images are shown in Fig.5.1. Despite some sub-micron features were observed in the topographical image due to surface roughness, the surface potential image (or Electric Force Microscopy, EFM image) of the film looks uniform and featureless. If there were some PCBM aggregates on the top surface of P3HT:PCBM, they would be distinguishable by EFM [24,25]. From the in-situ study of the annealing process of P3HT:PCBM BHJ solar cells by AFM, the top surface of P3HT:PCBM is dominated by enriched P3HT.

Fig.5.1 AFM images of morphology, surface potential and phase on P3HT:PCBM blend with a size of 5μm×5μm.

To investigate the composition ratio of donor/acceptor materials throughout a P3HT:PCBM blend thin film, XPS is employed. XPS spectra of C1s and S2p are shown in Fig.5.2. Although it is not easy to detect O atoms in the P3HT:PCBM blend by XPS, it is still possible to obtain the ratio of P3HT:PCBM from the ratio of C:S [25]. In previous reports, percentages of P3HT on film surfaces, ranging from 69% to 90%, have been obtained from XPS analysis and the partial-electron yield from the

near-edge x-ray absorption fine structure [25-27]. The sample featured in Fig. 5.2 was determined to contain 7% S and 93% C at the top surface, which corresponds to the calculated weight ratio of ~80% of P3HT and ~20% of PCBM. This suggests that P3HT is prevalent at the top surface, and that the observed vertical phase is not optimal. Furthermore, we also employed XPS with layer-by-layer etching to investigate the vertical phase separation as a function of film depth. Near the top surface (0-10 nm), the film is P3HT enriched, while the P3HT concentration gradually decreases deeper in the film. In the middle of the film (~40 nm to 110 nm), greater PCBM content was shown. At the bottom of the film, the P3HT content re-increases again. Past ~170 nm, the S% sharply increases while the O1s peak also became detectable, indicating the start of PEDOT:PSS. (PETOT:PSS $((C_6H_6O_2S)_x(C_8H_8O_3S)_y)$ contain more O than the layer of P3HT:PCBM.)

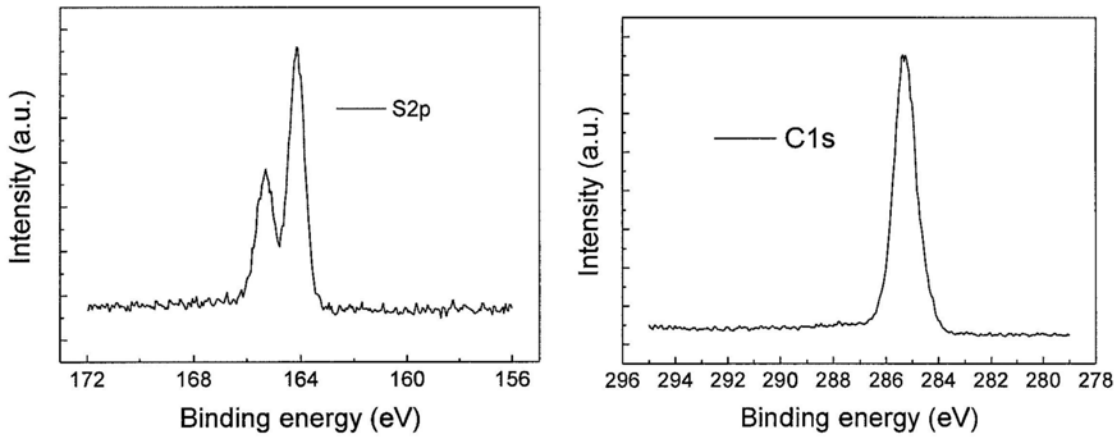

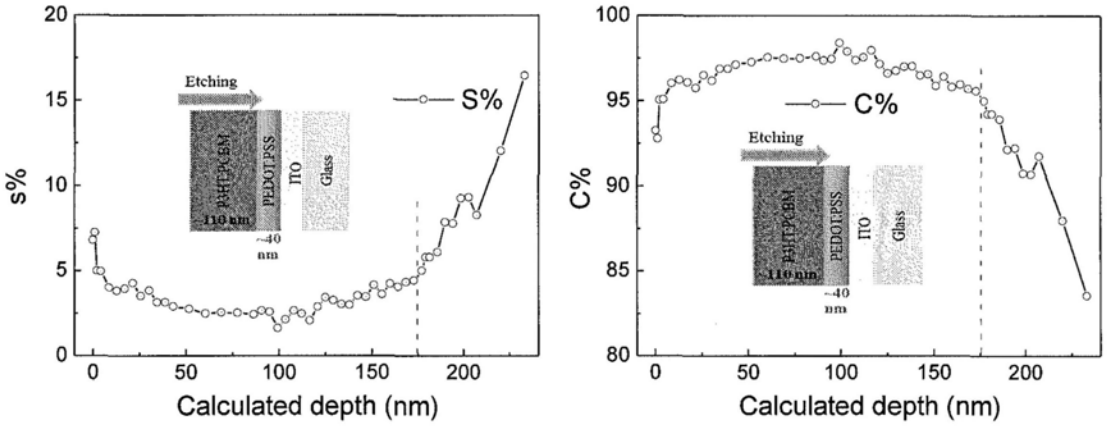

Fig.5.2 XPS of (a) S 2p and (b) C 1s, atomic percentage depth profile of (c) S and (d) C for P3HT:PCBM blend film on ITO glass with a PEDOT:PSS layer.

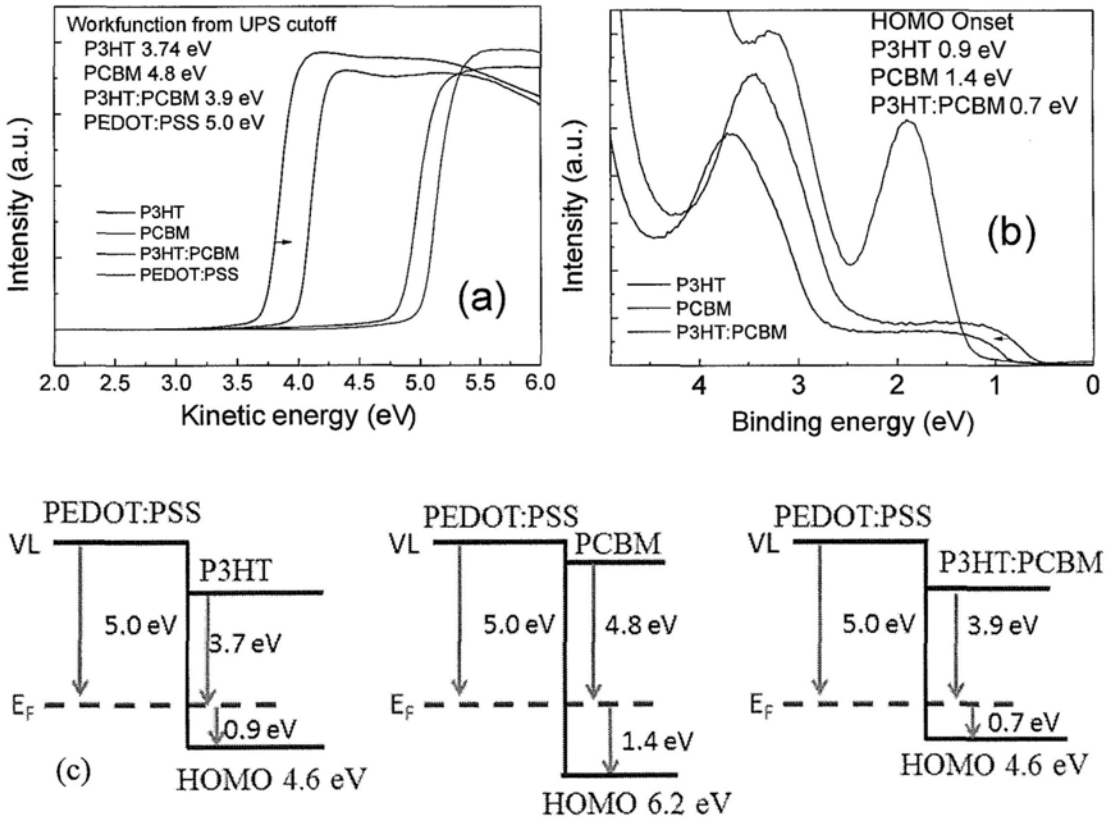

Fig.5.3 (a) work functions as determined by second electron cutoff from UPS spectra (b) HOMO onsets as determined by UPS spectra of valence band, and (c) corresponding energy level diagrams of P3HT, PCBM and P3HT:PCBM on PEDOT:PSS.

We also examine the top surface with Ultraviolet Photoemission Spectroscopy (UPS), which allows us to study the energy level alignment of different layers. As shown in Fig.5.3, the workfunction of PEDOT:PSS on ITO glass was determined to be 5.0 eV, which is close to the reported values by others [28]. The low binding energy edge of the organic semiconductor (valence band) corresponds to the HOMO feature position [29]. The values of the workfunction and HOMO in P3HT, PCBM, and P3HT:PCBM blend on the PEDOT:PSS substrates are shown in Fig.5.3, respectively, and these values are close to those reported by others [28,30]. For P3HT similar values are observed for both the workfunction and HOMO in the pure polymer phase and the P3HT:PCBM blend. Besides, the valence band spectra of P3HT:PCBM blend show no PCBM features from 1.5 to 2.5 eV. These, again, indicates that the top surface is dominated by P3HT.

Both XPS and UPS results show that the top surface of the P3HT:PCBM blend is mainly dominated by the P3HT component, which is in agreement with the vertical phase separation with P3HT accumulated on the top surface, due to its lower surface energy (γ_{P3HT}: 27 mN/m^2, γ_{PCBM}: 38 mN/m^2) [30, 31].

5.3.2 A Double-Junction model

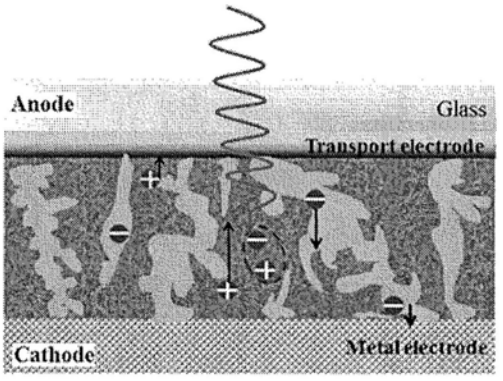

(a)

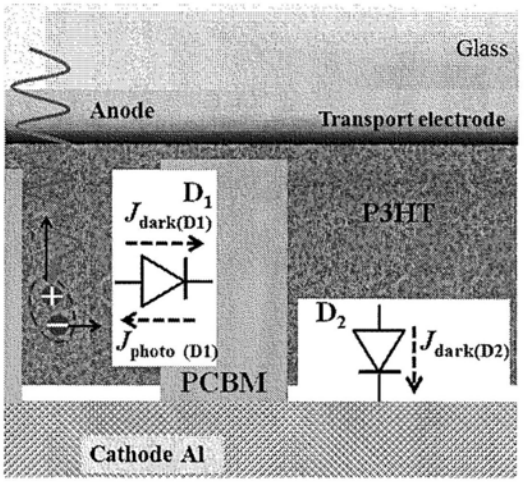

(b)

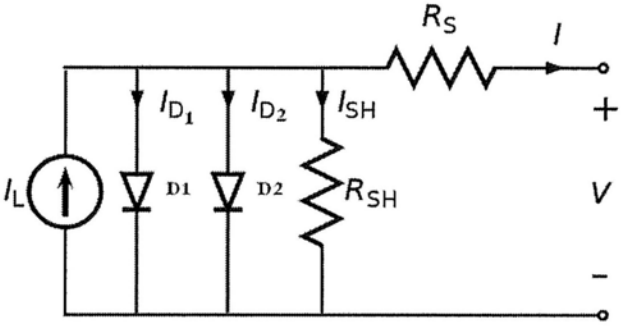

(c)

Figure 5.4 (a) Schematic structure of BHJ solar cells (b) simplified BHJ structure with D_1 representing a pn junction at the P3HT/PCBM interface and D_2 a Schottky diode between P3HT and the Al cathode. The photocurrent generated at the P3HT/Al Schottky diode is negligible compared to $J_{photo\ (D1)}$, (c) an equivalent circuit of BHJ solar cells with double-junction model.

The BHJ structure is shown in Fig.5.4. Both P3HT and PCBM can be directly connected to the Al electrode. In the MIM model, the organic semiconductor and metal forms a metal/insulator contact, not a Schottky contact, because the carrier densities of organic semiconductors are usually low. However, it is thought that P3HT can form Schottky diode at the P3HT-Al contact [32]. There are at least two causes for the formation of a P3HT/Al Schottky diode. It is well-known that P3HT is a conjugated polymer that can be easily p-doped when exposed to oxygen and/or water molecules [33, 34]. Another factor is that the charge transfer between PCBM and P3HT results in the accumulation of holes in P3HT [23]. This Schottky diode should be studied because the P3HT component is prevalent on the top surface and directly connects to the Al electrode in the BHJ structure as discussed above. On the other hand, the P3HT/PCBM (donor/acceptor) interface is a pn junction that behaves like a diode. Therefore, the device behavior in P3HT:PCBM BHJ solar cells should be described considering two diodes, one formed at the P3HT/PCBM interface and the other at the P3HT-Al contact. Regarding other interfaces in the BHJ organic solar cell structure, the contact between PCBM and Al is generally thought as an ohmic contact [2, 35-36]. At the bottom interface, the PEDOT:PSS layer blocks electron injection from PCBM into the ITO electrode while facilitating holes transferring to ITO [37, 38], due to the work function of PEDOT:PSS being in the middle of the gap between the HOMO and LUMO states of PCBM. Thus the influence of the anode interface on V_{oc} is small, since it is modified by a PEDOT:PSS layer. We therefore do not consider

any possible diode at the anode interface.

Taking into account an ohmic contact for holes transport at the anode via P3HT and an ohmic contact for electron transport at cathode via PCBM, we can use a double-junction model to simplify the BHJ solar cell into a device with two diodes, which is shown in Fig.5.4 along with its equivalent circuit. The diode D_1 is attributed to the donor/acceptor interface P3HT/PCBM, a pn junction that is essentially dominated by the HOMO of the donor and LUMO of the acceptor; Diode D_2 is a Schottky diode between P3HT (donor) and the cathode. The Schottky diode between P3HT and Al should be sensitive to the properties of the cathode interface, such as the workfunction of the metal, relative energy diagram of interfacial layers and the oxidation of the cathode. In the double-junction model, the contribution of the Schottky diode to the photocurrent is negligible compared to that of the pn diode, $J_{photo\ (D1)}$. On the other hand, solar cells reach open circuit conditions when $J_{dark(D1)}+ J_{dark(D2)}=J_{photo}$, and the device stops outputting power if $J_{dark(D1)}+ J_{dark(D2)}>J_{photo}$. Therefore the turn-on voltage or built-in potential (V_{bi}) of each diode is crucial for the V_{oc} of the solar cells.

From the *J-V* characteristics shown in Fig.5.5, we observe that devices with pure P3HT (structure of ITO/PEDOT:PSS/P3HT/Al) acts as a Schottky diode with its turn-on voltage at ~0.4 V. Inserting an interfacial layer (e.g. LiF or Ca) between the P3HT and the Al cathode can effectively increase the turn-on voltage of the diode to ~1 V. Interestingly, the P3HT:PCBM BHJ device without any cathode interfacial layer (structure of ITO/PEDOT:PSS/P3HT:PCBM/Al) also displayed similar *J-V*

characteristics with a turn-on voltage of ~0.4 V, indicating that the P3HT diode plays a key role in the performance of P3HT:PCBM BHJ solar cells. After inserting an interfacial layer between the organic active layer and Al cathode, the turn-on voltage is only increased to ~0.6 V, a much smaller increase compared to that of the pure P3HT diode. (We also observe that the V_{oc} of the corresponding devices increases from ~0.4 V to ~0.6 V.) The small increase gained from adding a cathode interfacial layer can be explained by the double-junction model: for the BHJ structure the turn-on voltage is originally limited by the Schottky diode; after insertion of cathode interfacial layer the turn-on voltage of the Schottky diode is increased and the overall turn-on voltage of the solar cell is then limited by that of the pn diode. To verify this model, we employ the impedance spectroscopy and transient photovoltage spectroscopy on difference organic PV systems. The results are discussed in the following sections.

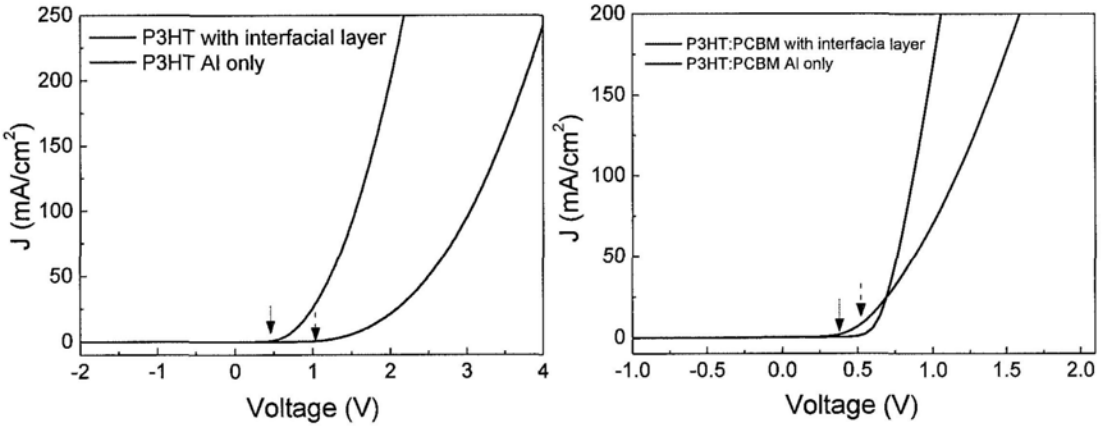

(a) (b)

Fig.5.5 *J-V* characteristics of (a) pure P3HT diode and (b) P3HT:PCBM BHJ solar cells with and without interfacial layer.

5.3.3 Negative capacitance of the double-junction structure probed by impedance spectroscopy

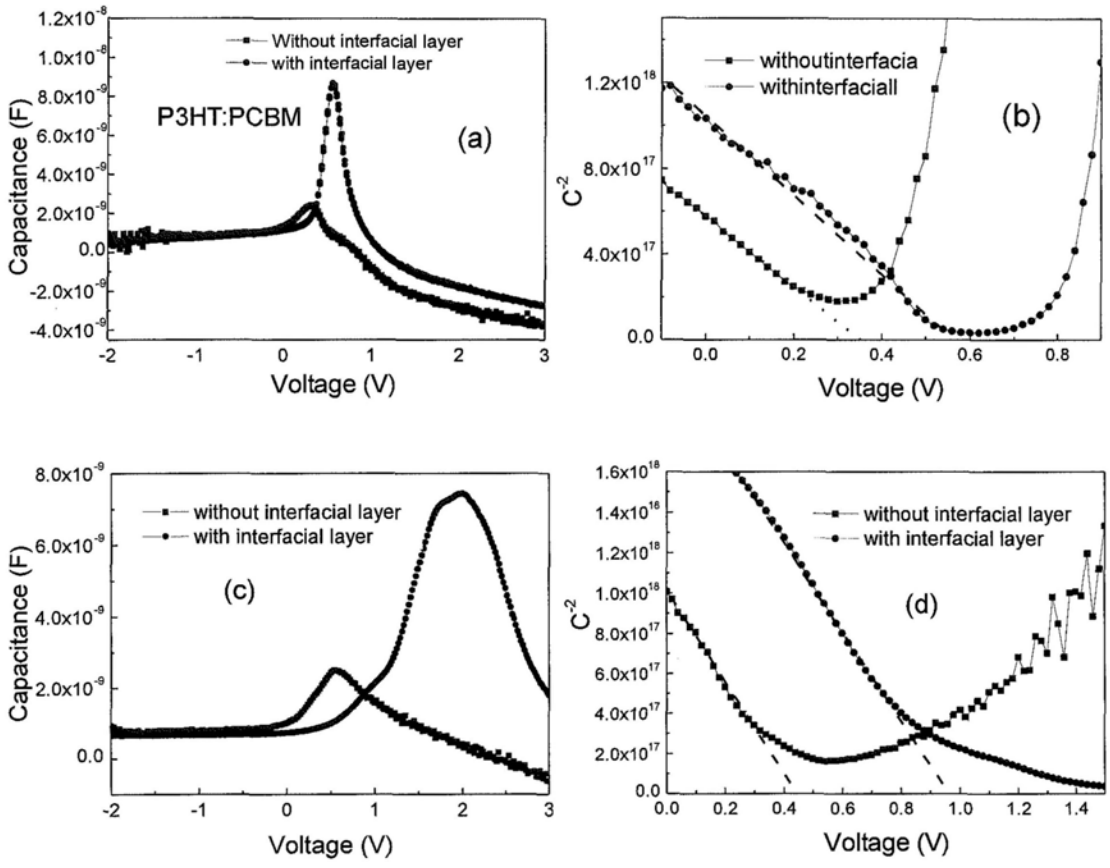

Fig.5.6 *C-V* characteristics of (a) P3HT:PCBM BHJ solar cells (c) P3HT diodes, with and without an interfacial layer, and their Mott-Schottky curves of (b) P3HT:PCBM BHJ solar cells (d) P3HT diodes, with and without an interfacial layer.

C-V measurements are one of the most useful methods for extraction of the built-in potential according to the Mott-Schottky relation: $C^{-2} = \frac{2(V_{bi} - V_a)}{A^2 q \varepsilon \varepsilon_0 N_A}$, where A is the device area, ε the dielectric constant, N_A the concentration of impurities or charges. Fig.5.6 shows the *C-V* characteristics and Mott-Schottky curves of P3HT:PCBM BHJ solar cells and P3HT diodes with and without an LiF interfacial layer under the Al cathode. The N_A of P3HT is estimated to be 5×10^{15} cm^{-3}, smaller

than that of P3HT:PCBM (8×10^{15} cm^{-3}). This is not surprising as the charge-transfer process at P3HT/PCBM interface can be considered as a doping process for both materials. Unlike the sharp increase of V_{bi} (from ~0.4 to ~1.0 V) in pure P3HT diode after insertion of a LiF interfacial layer, the V_{bi} in P3HT:PCBM only increase from ~0.4 to ~0.6 V, after the same cathode modification. Meanwhile, we observed that the V_{oc} of P3HT:PCBM cells is also increased from 0.4 V to 0.59 V by inserting a LiF at the cathode interface, indicating that the V_{oc} can be limited by the built-in potential of the solar cell.

The observed *C-V* characteristics can be explained using the double-junction model mentioned in the previous section by assigning a pn junction between the donor and acceptor (P3HT and PCBM), D_1, with a built-in potential of 0.6 V, and a Schottky diode between P3HT-Al, D_2, with a built-in potential of 0.4 V. In the device without any interfacial layer, the Schottky diode D_2 has a low built-in voltage and will therefore first be turned-on under forward bias, which opens a charge recombination pathway and consequently limits the V_{oc} to ~ 0.4 V. On the other hand, after insertion of an interfacial layer the D_2 diode seems to be diminished, and it becomes the D_1 pn junction that turns on first and limits the V_{oc} to ~ 0.6 V. Our results here suggest that the diode with lower built-in potential will be turned on first and will then serve as the charge recombination pathway, eventually terminating the photocurrent and limiting the V_{oc}.

It is interesting to note that the maximum capacitance (C_{max}) under forward bias voltage under dark is located around V_{oc}. Fig.5.7 shows a typical *J-V* characteristicand

C-V characteristic curves of P3HT:PCBM based devices with cathode interfacial layer, both measured in the dark. The *J-V* characteristics can be clearly divided into three regions: ohmic current, trap-charge limited current (TCLC, or trap filling), and space charge limited current (SCLC) [39, 40]. The *C-V* characteristics with negative capacitance are consistent with previous reports [32, 41]. We believe that the negative capacitance in the P3HT:PCBM BHJ solar cells is caused by the charge recombination, either through trap-assisted recombination or bimolecule recombination. As described in the introduction section, a device will exhibit negative capacitance-voltage slope when the radiative or non-radiative charge recombination starts to prevail in the device. This will then lead to a sharp increase of the recombination current, which limits the device V_{oc}. As a result, a close relation between the V_{oc} and the onset of the negative capacitance-voltage slope can be observed.

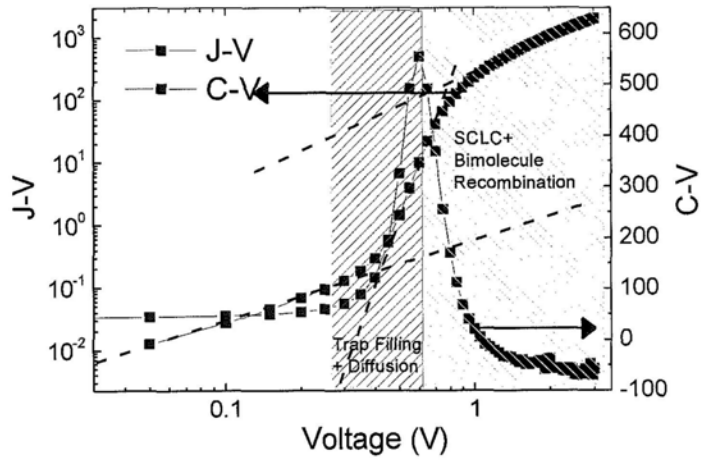

Fig.5.7 *J-V* and *C-V* characteristics of a P3HT:PCBM BHJ solar cell in the dark.

Before investigating the relationship between the energy alignment at the donor/acceptor interface and the V_{oc} of the device, it is necessary to first understand how inserting an interfacial layer, such as LiF and Ca, affects the Schottky diode between the donor material and Al cathode (e.g. P3HT-Al). The negative capacitances in the dark and the corresponding *J-V* characteristics under illumination are shown in Fig.5.8 for P3HT:PCBM, MEHPPV:PCBM, and PFB:F8BT solar cells. Consistently, we observe that the V_{oc} can be located at the voltage corresponding to the C_{max} in MEHPPV:PCBM and PFB:F8BT BHJ solar cells with a Ca interfacial layer.

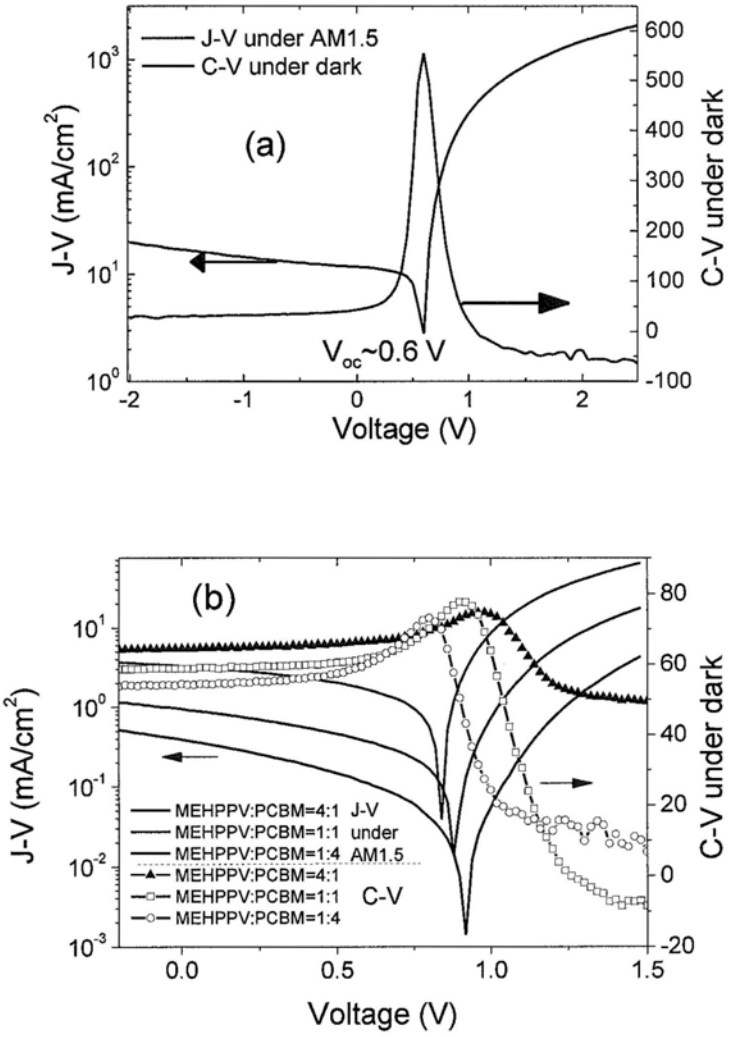

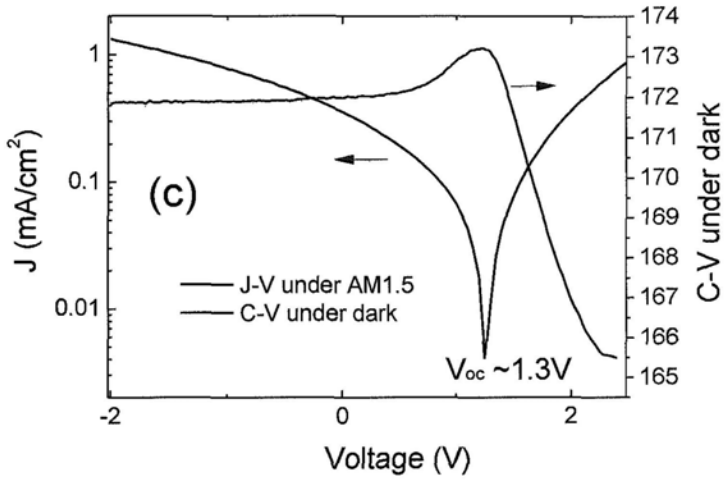

Fig.5.8 *J-V* characteristics under illumination and *C-V* characteristics in the dark of (a) P3HT:PCBM, (b) MEHPPV:PCBM, and (c) PFB:F8BT BHJ solar cells.

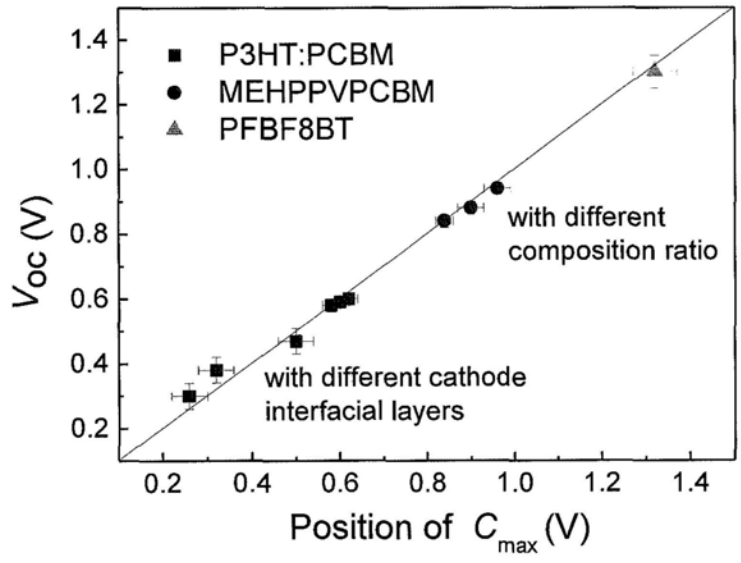

Fig.5.9 Open circuit voltage for the solar cells under AM1.5 illumination vs. the peak position of maximum capacitance (C_{max}). MEHPPV:PCBM cells with three different stoichiometries (1:4, 1:1, 4:1) as well as P3HT:PCBM devices with different cathode interfacial layers, inducing CuO_x, Al only, Cr, CrO_x, LiF and Ca, are included in the graph.

Figure 5.9 shows the relation between the V_{oc} and the voltage position corresponding to C_{max} for various types of devices we fabricated, including F8BT:PFB cells, MEHPPV:PCBM cells with three different blending ratio as well as P3HT:PCBM devices with different cathode interfacial layers. The data can be nicely fitted with a straight line with a slope of 1, and no offset between the V_{oc} and the peak position of maximum capacitance is required. This suggests that the negative capacitance and V_{oc} are limited by the same charge recombination process, which can either be at the donor/cathode interface or at the donor/acceptor interface.

Our study shows that there is indeed no conflict of the origin of the V_{oc} between MIM model and $HOMO_D$-$LUMO_A$ model, under the double-junction model. Both models are reconciled by the negative capacitance resulting from charge recombination, and they can be used in conjunction by assuming that V_{oc} is determined by the junction with the smaller negative capacitance onset. For most devices cathode modification can tune the V_{oc} maximum from the Schottky junction limited regime to the donor/acceptor junction limited regime.

5.3.4 Double-Junction confirmed by transient photovoltage spectroscopy

To further understand the recombination behavior of the donor/cathode junction and the donor/acceptor junction, particularly under illumination, we employ the transient-voltage method to investigate the dynamics of such recombination processes [42,43].

The bimolecular recombination at the donor/acceptor interface is often described

by the Langvin equation $R=np/\tau$ or n^2/τ, where τ is the lifetime of perturbation charge carriers, and n and p the concentrations of photo-induced electrons and holes, respectively. A more generalized description is proposed by Durrant *et al.* [44], which states that the lifetime of charge carriers, τ, is related to n and p by a power-law and τ increasing with n and p. On the other hand, recombination at cathode electrode surface by trap states can be simply expressed as $R= n/\tau$, where τ is the lifetime of carriers, $\tau \propto 1/N_t$, N_t being the trap density. The recombination dynamics of two diodes should be different and distinguishable through the transient photovoltage measurements, in which varying the incident light intensity into devices changes concentration of the photo-induced charges. The working principle behind transient photovoltage has been introduced in the characterization part of chapter 2.

The transient photovoltage spectra of P3HT:PCBM solar cells without any interfacial layer (Al only) and with a Ca interfacial layer are shown in Fig.5.10. The transient photovoltage (ΔV) can be taken as a function of V_{oc} by varying the bias light intensity. The signals have been normalized to the same height at time zero, before turning off the transient, triggering light. The actual perturbation voltage maximum was kept below 6 mV, controlled by tuning the intensity of the triggering light. As Fig.5.10 shows, both types of P3HT:PCBM BHJ solar cells had similar transient times under light with an intensity of 1.2 Sun, however, the device with a Ca interfacial layer had much longer transient time than the one without an interfacial layer when the bias light intensity was decreased from 1 Sun to 0.02 Sun. Pseudo-first-order rates for the recombination reactions, are extracted from exponentially fitting the transient

photovltage spectra [42, 43], and are plotted as a function of light intensity as shown in Fig. 5.10 (b) and (d).

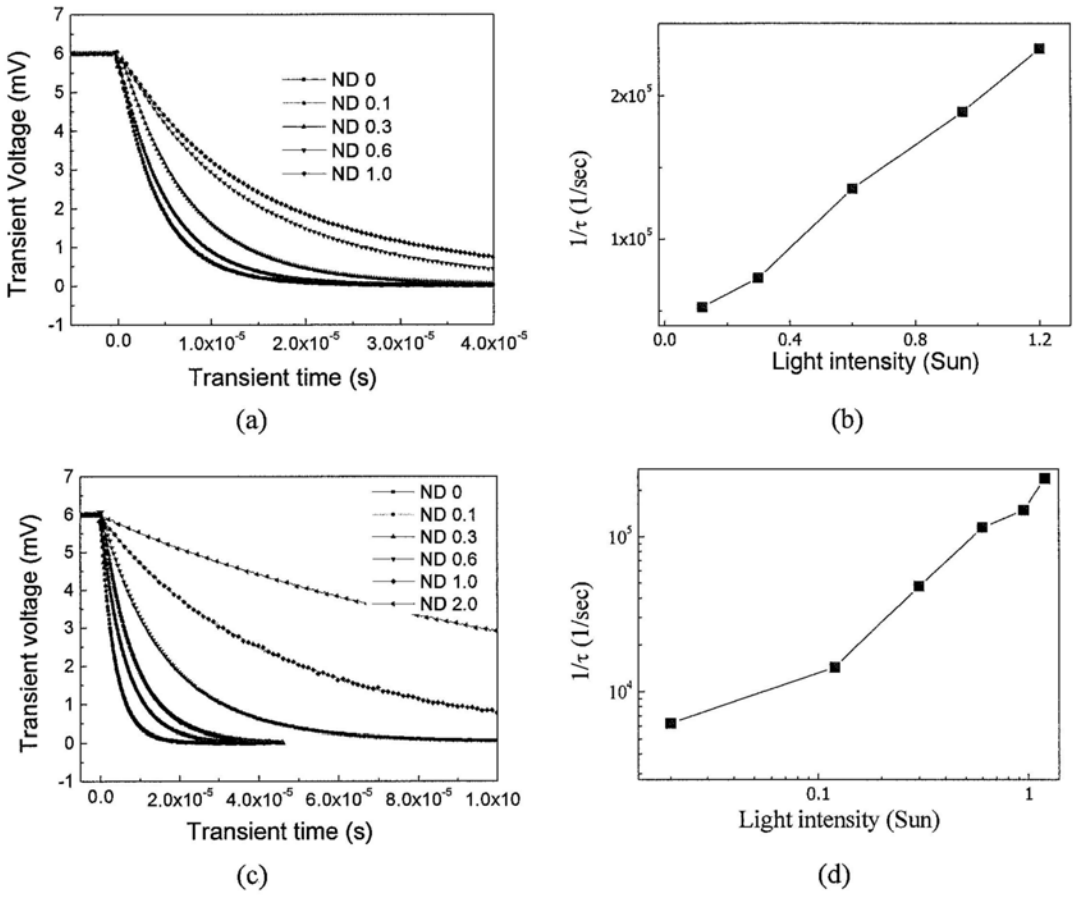

Fig.5.10 Transient photovoltage curves of P3HT:PCBM BHJ solar cells (a) with and (c) without any interfacial layer, and recombination rates of devices (b) with and (d) without any interfacial layer, respectively.

As shown in Fig.5.10, there is a strong dependence of the recombination rate constant on the intensity of the bias light (or the V_{oc}). For P3HT:PCBM solar cells with an interfacial layer, the recombination rate under 1.2 Sun illumination is 2×10^{5} s^{-1}, giving a lifetime of 5×10^{-6} s. Under 0.12 Sun, the recombination rate decreased to 1.4×10^{4} s^{-1}, corresponding to a lifetime of 7×10^{-5} s. For devices without any

interfacial layer, the recombination rate constant decreases considerably less from 2.3 $\times 10^5$ s^{-1} to 5.3 $\times 10^4$ s^{-1} as the light intensity drops from 1.2 to 0.12 Sun. The different extents of the recombination rate drop in the devices with and without any interfacial layer can be well explained by our double junction model, as illustrated in Fig.5.11. In devices with a Ca interfacial layer, the recombination is dominated by bimolecular recombination at the pn junction of donor/acceptor interface. The recombination rate is very sensitive to the bias light intensity as it determines n and p. In the device without an interfacial layer, however, the Schottky diode turns on first and therefore plays a more important role in charge recombination at the cathode surface through trap states (N_τ), which is less affected by the bias light intensity. Thus the drop of the recombination rate as a function of bias light intensity is much slower in devices without interfacial layer, limited by a Schottky diode.

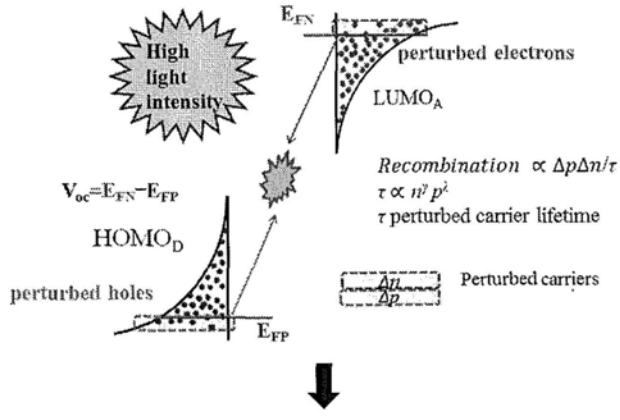

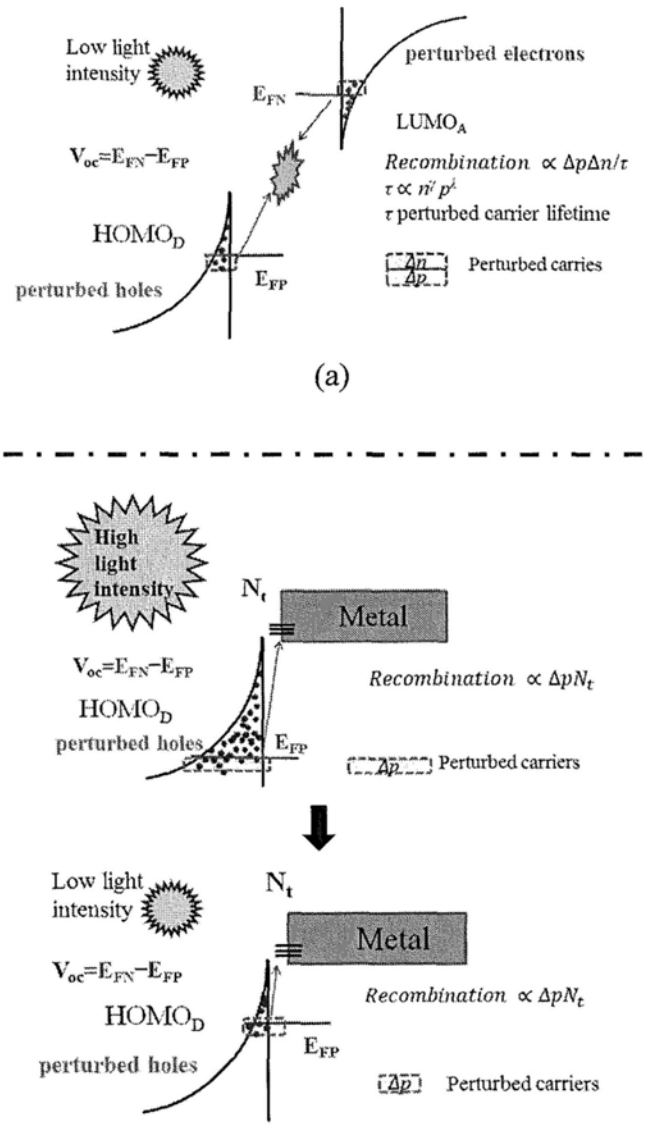

Fig.5.11 Schematic diagrams of recombination at (a) the donor/acceptor interface and (b) electrode surface with high light intensity and low light intensity. Higher Fermi level indicates higher density states, leading stronger recombination.

To verify our hypothesis and to further understand how modifying the cathode interface changes the V_{oc} maximum from the Schottky junction limited regime to the donor/acceptor junction limited regime, we also measured the transient photovoltage spectra in P3HT:PCBM solar cells without cathode interfacial layer and with different

interfacial layers, including Ca, CrO_x CuO_x, LiF, and a CrO_x/LiF bilayer. Fig.5.12 shows the recombination rates in different devices as a function of V_{oc}, obtained by varying the intensity of bias light. First, different dropping speeds of the recombination rate as of all cathode interfacial layersare shown. Similarly to device Al only, in devices with a CuO_x interfacial layer, the V_{oc} drops quickly with decreasing bias light intensity and maintained a relatively higher recombination rate. Due to its high work function of 4.9 eV, the CuO_x interfacial layer reduces the turn-on voltage of the Schottky diode, leading to a higher surface recombination rate at the cathode. On other hand, the recombination rate similarly drop faster in devices with other interfacial layers than that in devices Al only and with CuO_x, with their decreasing V_{oc}. It indicates that recombination is dominated at real donor-acceptor interface after good cathode modification.

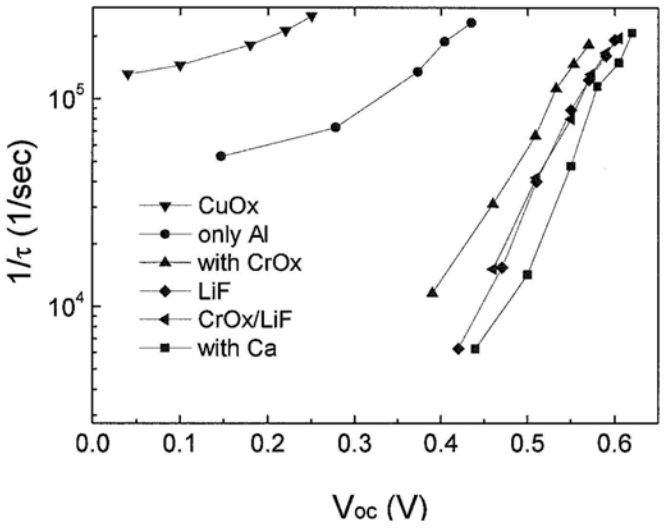

Fig.5.12 Recombination rates vs. V_{oc} for P3HT:PCBM cells with different cathode interfacial layers. V_{oc} was varied by varying the bias light intensity. Triggering light intensity was varied to maintain a peak ΔV below 6 mV.

The result of the transient photovoltage measurement is in good agreement with the impedance spectroscopy result, which suggests that there are at least two junctions affecting the charge recombination process and the V_{oc} in the studied BHJ solar cells and that cathode/active layer interface modification can determine which junction is the limiting factor for the device performance.

5.3.5 Simulation of V_{oc}

We have demonstrated several experimental results that suggest the limitation of V_{oc} can be explained using the double-junction model. In this section we quantitatively analyze the V_{oc} loss using the simple equivalent circuit shown in Fig. 5.4 (c). The total current, containing both injected dark current and photo-induced current, in the double-junction model for BHJ solar cells can be described by: $J = J_{0D1}(e^{\frac{q(V_a - JR_s)}{n_1 kT}} - 1) + J_{0D2}(e^{\frac{q(V_a - JR_s)}{n_2 kT}} - 1) + \frac{V_a - JR_s}{R_{sh}} - J_{ph}$. To reduce the fitting parameters and improve the fitting accuracy, we first simplify the model back into an one-diode equation, $J = J_0(e^{\frac{q(V_a - JR_s)}{nkT}} - 1) + \frac{V_a - JR_s}{R_{sh}} - J_{ph}$, where J_{ph} is the photocurrent, J_0 the saturation current in device, n the ideal factor, k the Boltzman constant, T the temperature, R_s the series resistance, R_{sh} the shunt resistance. This simplification is based on the assumption that close to V_{oc} the current-voltage characteristics will be dominated by one of the two diodes. From the above equation, we can obtain an equation for V_{oc} $V_{oc} = \frac{nkT}{q}\ln(\frac{J_{ph} - V_{oc}/R_{sh}}{J_0} + 1)$, which can further

be simplified into $V_{oc} = \frac{nkT}{q}\ln(\frac{J_{ph}}{J_0}) \approx c - \frac{nkT}{q}\ln(J_0)$, and $\beta = \frac{nkT}{q}\ln(J_0)$ can be a most important parameter for determining the open circuit voltage (for example, a device with J_{sc} of 10 mA/cm^2 and β=30 has a V_{oc} of 0.6 V).

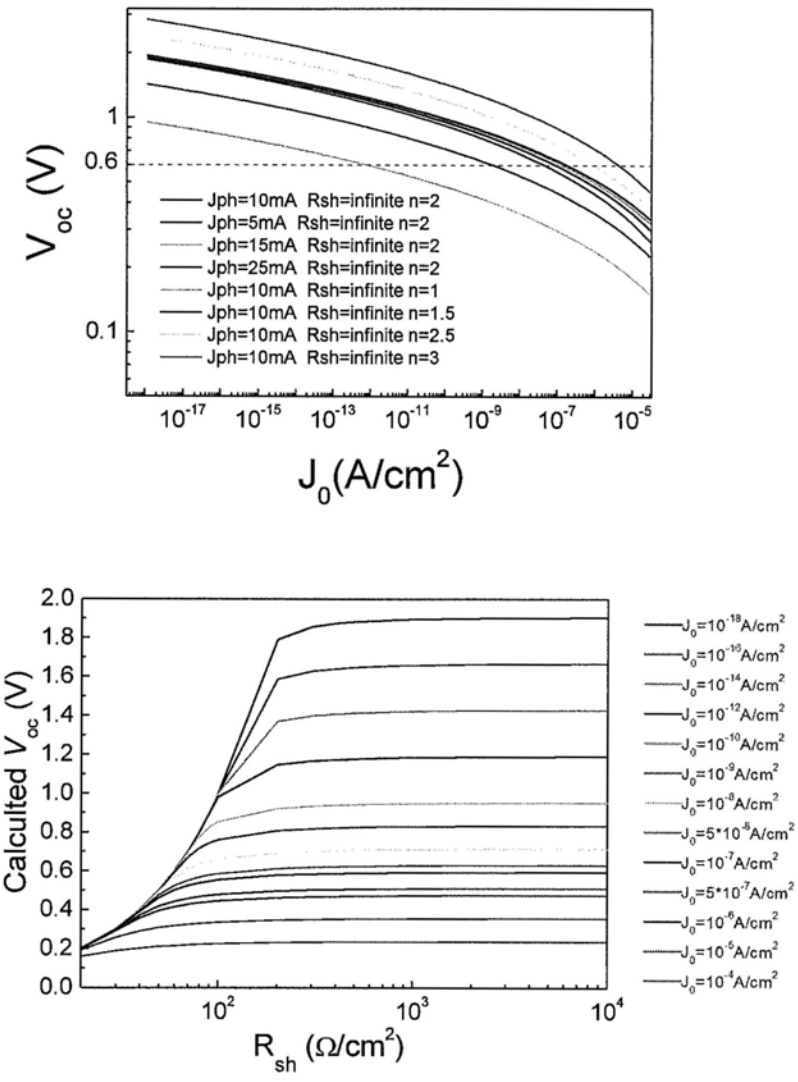

Fig.5.13 V_{oc} simulated (a) with J_{ph}, J_0, n and (b) with R_{sh}.

Fig5.13 shows the influence of J_{ph}, J_0, n, and R_{sh} on the simulated V_{oc}. The influence of J_{ph} on the V_{oc} is relatively small compared to J_0, n, and R_{sh}, which is in

agreement with the previous observation that for some of the P3HT:PCBM solar cells the photocurrent can rapidly decay upon air exposure while the V_{oc} of the same devices remains almost unchanged. Small shunt resistance (below 500 Ω/cm^2) seriously reduces V_{oc}, although it has little effect on V_{oc} after reaching a value over 3000 Ω/cm^2. V_{oc} is more sensitive to n and J_0. Empirically, n=1 when the current is dominated by the diffusion process, and n=2 if the current is dominated by recombination process [45]. In organic solar cells, the n is ~2, meaning that the recombination processes play a key role in device operation. Usually, devices with higher V_{oc} have lower J_0. Typically, J_0 is determined by recombination at the donor/acceptor interface and the electrode surfaces as well as traps sites [46, 47].

Table 5.1 Fitted and measured parameters for P3HT:PCBM solar cells with different cathode interfacial layers.

Sample	J_{ph} (mA/cm^2)	V_{oc} (V)	FF	PCE (%)	J_0	n	R_s	R_{sh}	V_{oc} (calculated) V	$n \times ln(J_0)$
only Al	8.45	0.40	0.46	1.5	8×10^{-7}	1.95	5	2020	0.46	-27.4
LiF/Al	10.08	0.59	0.59	3.8	4×10^{-10}	1.38	1.3	7246	0.608	-29.8
Cr/Al	9.90	0.47	0.49	2.3	9×10^{-8}	1.80	2.2	1000	0.538	-29.2
CrO_x/Al	11.15	0.58	0.61	3.9	3×10^{-10}	1.33	1.3	3300	0.599	-29.16
Ca/Al	10.65	0.61	0.57	3.7	5×10^{-10}	1.43	2.3	18000	0.626	-30.62

**The R_s and R_{sh} are firstly calculated from J-V curve in the dark [47], and slightly changed around these calculated value during following fitting. J_0 and n are extracted by fitting dark J-V curve using the equation* $J = J_0(e^{\frac{q(V_a - JR_s)}{nkT}} - 1) + \frac{V_a - JR_s}{R_{sh}}$.

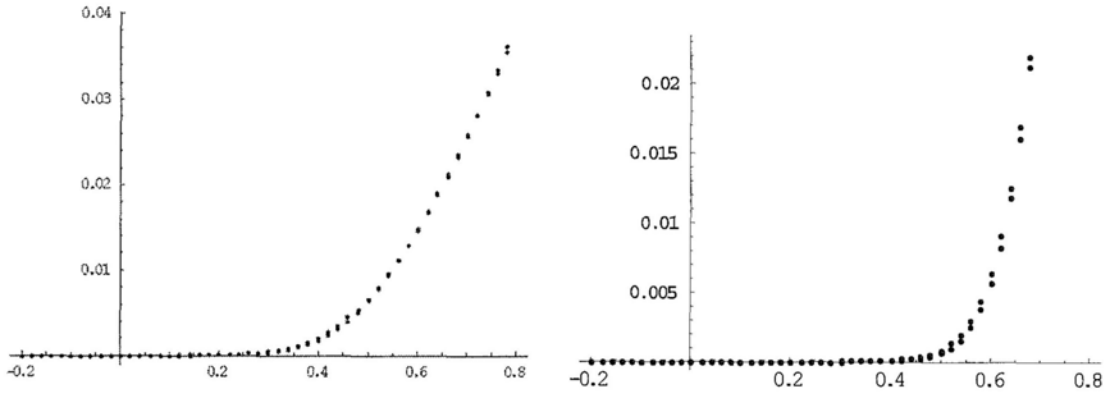

(a) (b)

Fig. 5.14 The measured and fitted *J-V* curves under dark inP3HT:PCBM solar cells (a) Al only and (b) with a LiF interfacial layer. The dark points are measured data, and red points are fitted data.

Based on the double-junction model, the J_0 of the Schottky diode and pn junction at the donor/acceptor should be distinguishable in P3HT:PCBM BHJ organic solar cells. This is indeed confirmed by the fitting parameters as shown in Table 5.1. To avoid the complexity of voltage dependent J_{ph}, we fit the dark current curves to extract the parameters. The measured and fitted curves in device Al only and with a LiF interfacial layer are shown in Fig.5.14. For devices without interfacial layer, J_0 was determined to be 8×10^{-7} A/cm^2 with a high n of 1.9, which was mainly attributed to the Schottky diode. After modification by CrO_x, LiF and Ca, the J_0 was significantly reduced to ~4×10^{-10} A/cm^2 and the n dropped to ~1.4, which indicates that the J_0 of the pn junction at the P3HT/PCBM interface had a value of around 10^{-10} A/cm^2. On other hand, the value of J_0 should differ from different donor/acceptor interfaces as well, so the types of materials used in the active layer should also affect the V_{oc} of BHJ organic solar cells [47].

5.3.6 Electroluminescence of organic solar cells

Various types of recombination events in BHJ solar cells limit their performance. The four most important recombination processes include exciton recombination, trap-assisted recombination, geminate recombination and bimolecular recombination. Exciton recombination can give rise to polymer luminescence while it is not a limiting factor in BHJ solar cells because the exciton dissociation is greatly facilitated by the nanoscale phase separation between donor and acceptor [11]. The trap states in the forbidden gap can be recombination center in disordered organic blend system, which is usual in the way of non-radiation. Geminate recombination can occur after charge-transfer across the donor-acceptor interface if the following charge separation process is inefficient. Finally, the already-separated charge carriers ("free" carriers) or the injected carriers from external circuit can recombine either at the donor/acceptor interface or within one phase, referred to as bi-molecular recombination. It is believed that both geminate and bimolecular recombination primarily occur during operation of solar cells and light emitting diodes. The radiative recombination from free carrier recombination through weakly bound charge transfer (CT) states in polymer fullerene based OPV has been observed by electroluminescence (EL) [11,47].

Here we try to use one of our model BHJ systems to study radiative bimolecular recombination process. EL measurement is a good tool for investigating radiative recombination in OPVs. It has been reported that a PFB:F8BT BHJ device can work both as an LED and a PV, although the performance of either device is poor [49]. In our experiment we observe the EL emission of the BHJ devices as we change their operation mode from PV to LED by increasing the forward bias voltage.

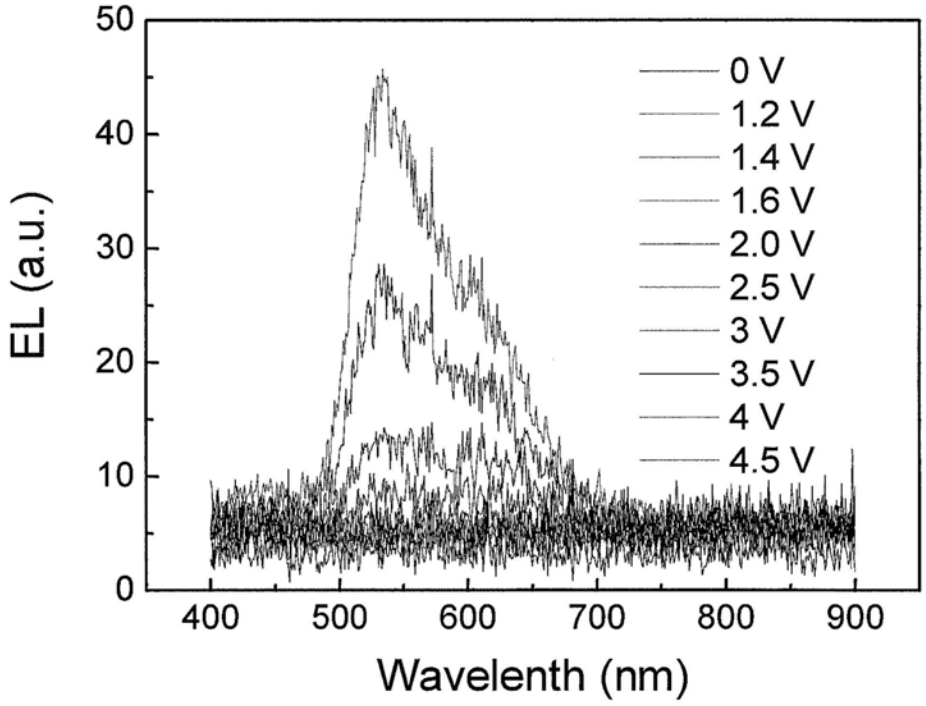

Fig.5.15 EL spectra of PFB:F8BT BHJ solar cells with increasing forward bias voltage.

As shown in Fig.5.15, it is difficult to observe the EL emission with a forward bias bellow or around V_{oc}. This is possibly due to the low signal-to-noise ratio of our measurement apparatus at room temperature. Nevertheless, we can observe EL emissions starting from the bias voltage of ~3 V. The emission centered around the wavelength of 550 nm is attributed to F8BT, and the one around 650 nm to the CTs of PFB:F8BT [50]; the PFB exciton emission is absent. With the increased forward bias voltage, the EL of the F8BT emission increases more than that of the CT emission. This is probably due to the onset of the electron-back transfer in Macus inverted regime [51, 52].

5.4 Summary of Chapter 5

We describe the limit of V_{oc} in polymer BHJ solar cells with Al cathode using a double-junction model. In addition to the often-discussed junction at donor/acceptor interface, we also consider the role of a Schottky junction formed between the cathode and the donor material. To investigate the double-junction structure, we used AFM, XPS, UPS, impedance spectroscopy combined with transient photovoltage measurements. A negative capacitance behavior is observed, which marks the onset of a predominant charge recombination in one of the two junctions and is found to be closely related to the device V_{oc}. By studying different BHJ systems, including P3HT:PCBM, MEH-PPV:PCBM, and PFB:F8BT blend films, we found that the V_{oc} is determined by the junction with the smaller negative capacitance onset and that the cathode modification can tune the V_{oc} maximum from the Schottky junction limited regime to the donor/acceptor junction limited regime. Our results also suggest that the negative capacitance and V_{oc} are limited by the same charge recombination process at either the donor/cathode or donor/acceptor interface, it is suggested that the non-radiation recombination significantly and radiation partly limit the V_{oc} in BHJ solar cells.

Reference:

[1] W. Shockley, H. Queisser, J. Appl. Phys. 32, 510 (1961).

[2] V. D. Mihailetchi, P. W. M. Blom, J. C. Hummelen, and M. T. Rispens, J. Appl. Phys. 94, 6849 (2003).

[3] C. J. Brabec, Sol. Energy Mater. Sol. Cells 83, 273 (2004).

[4] C. J. Brabec, A. Cravino, D. Meissner, N. S. Sariciftci, T. Fromherz, M. T. Rispens, L. Sanchez, and J. C. Hummelen, Adv. Funct. Mater. 11, 374 (2001).

[5] M. F. Lo, T. W. Ng, T. Z. Liu, V. A. L. Roy, S. L. Lai, M. K. Fung, C. S. Lee, and S. T. Lee, Appl. Phys. Lett. 96, 113303 (2010).

[6] G. Dennler, M. C. Scharber, C. J. Brabec, Adv. Mater. 21, 1323 (2009).

[7] M. C. Scharber, D. Mühlbacher, M. Koppe, P. Denk, C. Waldauf, A. J.Heeger, and C. J. Brabec, Adv. Mater. 18, 789 (2006).

[8] S. Günes, H. Neugebauer, N. S. Sariciftci, Chem. Rev. 107, 1324 (2007).

[9] J. Cuiffi, T. Benanti, W. J. Nam, and S. Fonash, Appl. Phys. Lett. 96, 143307 (2010).

[10] C. G. Shuttle, B. O'Regan, A. M. Ballantyne, J. Nelson, D. D. C. Bradley, and J. R. Durrant, Phys. Rev. B 78, 113201 (2008).

[11] K. Tvingstedt, K. Vandewal, A. Gadisa, F. Zhang, J. Manca, O. Inganäs, J. Am. Chem. Soc. 131, 11819 (2009).

[12] G. Garcia-Belmontea, J. Bisquert, Appl. Phys. Lett. 96, 113301 (2010).

[13] C. Deibel , T. Strobel , and V. Dyakonov, Adv. Mater. 22, 4097 (2010).

[14] K. Vandewal, K. Tvingstedt, A. Gadisa, O. Inganäs, and J. V. Manca, Phys. Rev. 81, 125204 (2010).

[15] M. Matsumura and Y. Hirose, Appl. Surf. Sci. 175, 740 (2001).

[16] S. E. Laux and K. Hess, IEEE Trans. Electron Devices, 46, 396 (1999).

[17] E. Ehrenfreund, C. Lungenschmied, G. Dennler, H. Neugebauer, N. S. Sariciftci, Appl. Phys. Lett., 91, 012112 (2007).

[18] I. Mora-Sero´ , J. Bisquert, F. Fabregat-Santiago, G. Garcia-Belmonte, G. Zoppi, K. Durose, Y. Proskuryakov, I. Oja, A. Belaidi, T. Dittrich, R. Tena-Zaera, A. Katty, C. Le´vy-Cle´ment, V. Barrioz, S. J. C. Irvine, Nano Lett. 6, 640 (2006).

[19] C. Lungenschmied, E. Ehrenfreund, N. S. Sariciftci, Organ. Electron. 10, 115 (2009).

[20] L. S. C. Pingree, B. J. Scott, M. T. Russell, T. J. Marks, and M. C. Hersam, Appl. Phys. Lett. 86, 073509 (2005).

[21] S. Wu, J. Li, Q. Tai, F. Yan, J. Phys. Chem 114, 21873 (2010).

[22] L. F. Drummy, R. J. Davis, D. L. Moore, M. Durstock, R. A. Vaia, and J. W. P. Hsu, Chem. Mater. 23, 907 (2011).

[23] D. H. Yan, H. B. Wang, B. X. Du, Heterojunction Theory Organic of Semiconductor, Science Press, Beijing, (2008).

[24] D. C. Coffey, O. G. Reid, D. B. Rodovsky, G. P. Bartholomew, and D. S. Ginge, Nano Lett. 7, 738 (2007).

[25] H. Hoppe, T. Glatzel, M. Niggemann, A. Hinsch, M. Ch. Lux-Steiner, and N. S. Sariciftci, Nano Lett. 5, 269 (2005).

[26] A. Orimo, K. Masuda, S. Honda, H. Benten, S. Ito, H. Ohkita, and H. Tsuji, Appl. Phys. Lett. 96, 043305 (2010).

[26] Z. Xu, L. Chen, G. Yang, C. Huang, J. Hou, Y. Wu, G. Li, C. Hsu, and Y. Yang, Adv. Funct. Mater. 19, 1227 (2009).

[27] D. S. Germack, C. K. Chan, G. H. Hamadani, L. J. Richter, D. A. Fischer, D. J. Gundlach, and D. M. Delongchamp, Appl. Phys. Lett. 94, 233303 (2009).

[28] Y. Vaynzof, D. Kabra, L. Zhao, L. L. Chua, U. Steiner, and R. H. Friend, ACS Nano, 5 329 (2011).

[29] Y. L. Gao, Mat. Sci. and Engineer. R 68, 39 (2010).

[30] L. -M. Chen, Z. Xu, Z. Hong, Y. Yang, J. Mater. Chem. 20, 2575 (2010).

[31] J. Jaczewska, I. Raptis, A. Budkowski, D. Goustouridis, J. Raczkowska, M. Sanopoulou, E. Pamula, A. Bernasik, and J. Rysz, Synth. Met. 157,726 (2007).

[32] G. Garcia-Belmonte, A. Munar, E. M. Barea, J. Bisquert, I. Ugarte, R. Pacios, Organ. Electron. 9, 847 (2008).

[33] M. S. A. Abdou, F. P. Orfino, Y. Son, S. Holdcroft, J. Am. Chem. Soc. 119, 4518 (1997).

[34] S. Hoshino, M. Yoshida, S. Uemura, T. Kodzasa, N. Takada, T. Kamata, K. Yase, J. Appl. Phys. 95, 5088 (2004).

[35] V. D. Mihailetchi, P. W. M. Blom, J. C.Hummelen, M. T. Rispens, J. Appl. Phys. 94, 6849 (2003).

[37] M. D. Irwin, D. B. Buchholz, A. W. Hains, R. P. H. Chang, and T. J. Marks, PNAS 105, 2783 (2008).

[38] Q. L. Song, C. Gong, H. B. Yang, C. M. Li, Sol. Energy Mater. Sol. Cells 94, 2422 (2010).

[39] M. Kiy, P. Losio, I. Biaggio, M. Koehler, A. Tapponnier, and P. Gunter, Appl. Phys. Lett. 80, 2002.

[40] K. C. Kao and W. Hwang, Electrical Transport in Solids, Pergamon, Oxford, U.K. (1981).

[41] J. Bisquert, G. Garcia-Belmonte, A. Munar, M. Sessolo, A. Soriano, H. J. Bolink, Chem. Phys. Lett. 465, 57 (2008).

[42] B. C. O'Regan, S. Scully, A. C. Mayer, E. Palomares and J. Durrant, J. Phys. Chem. B 109, 4616 (2005).

[43] R. Hamilton, C. G. Shuttle, B. O'Regan, T. C. Hammant, J. Nelson, and J. R. Durrant, J. Phys. Chem. Lett. 1, 1432 (2010).

[44] D. Credgington, R. Hamilton, P. Atienzar, J. Nelson, and J. R. Durrant, Adv. Funct. Adv. Funct. Mater., xx, 1–10 (2011).

[45] S. M. Sze and K. K. Ng, Physics of Semiconductor Devices, A JOHN WILEY & SONS, Hoboken, New Jersey, U.S.A. (2007).

[46] D. Bruan, J. Polym. Sci. Part B: Polym. Phys. 41, 2622 (2003).

[47] K. Vandewal, K. Tvingstedt, A. Gadisa, O. Inganäs and J. V. Manca, Nature Mater. 8, 904 (2009).

[48] H. -L. Yip, S. K. Hau, N. S. Baek, H. Ma, A. K. -Y. Jen, Adv. Mater. 20, 2376 (2008).

[49] J. Poortmans, V. Arkhipov, Thin film solar cells fabrication, characterization and application, John Wiley & Sons, England, U.K. (2006).

[50] A. C. Morteani, P. K. H. Ho, R. H. Friend, C. Silva, Appl. Phys. Lett. 86, 163501 (2005).

[51] R. A. Marcus and N. Sutin, Biochimica et Biophysica Acta 811, 265 (1985).

[52] B. P. Rand, J. Genoe, P. Heremans and J. Poortmans, Prog. Photovolt.: Res. Appl. 15, 659 (2007).

Chapter 6

Conclusion and future plan

6.1 Conclusion

In this work, organic solar cells with different cathode interfacial layers, including the polymer-fullerene systems of P3HT:PCBM and MEHPPV:PCBM, the polymer-polymer system of PFB:F8BT, and the small molecule system of CuPc/C_{60}, have been fabricated and characterized. The main conclusions can be drawn as follows:

1. Cathode interface degradation greatly impacts the lifetime of organic solar cells. By conducting interface modification combined with electrical and chemical characterization techniques, it can be shown that rapid degradation originates from the thick interdiffused organic-Al interface between the organic active layer and Al cathode, which forms a charge blocking layer at Al cathode upon air exposure, and thus significantly reduces device performance.
2. Polymer-fullerene solar cells with CrO_x and CuO_x cathode interfacial layer show higher stability than those without the interfacial layer, typically with the stability improved by more than ~100 times than that of devices without any interfacial layer or with a LiF interfacial layer. We conclude that the CrO_x and CuO_x interfacial layers lead to more air-resistive cathode/organic interfaces by stopping or minimizing the penetration of thermally evaporated Al into the organic active layer, which would otherwise form a thicker diffused organic-Al interface that

results in a large oxidized interfacial area that will become a charge blocking layer upon air exposure.

3. Insertion of a CrO_x interfacial layer between the organic active layer and Al cathode can improve the stability of CuPc/C_{60} small molecule and PFB:F8BT all-polymer solar cells. However, the extent of the stability improvement in these devices is limited by the degradation within the organic active layer and/or at the anode/organic interface.

4. The performance of polymer-fullerene BHJ cells can be further improved by applying a CrO_x-LiF and CuO_x-LiF cathode interfacial bilayer structure, which is shown to maintain both higher stability and open-circuit voltage. In general, the thermally evaporated metal oxide/LiF interfacial bilayer structure could provide a good strategy for improving efficiency and stability of organic solar cells.

5. The existence of donor/acceptor pn junction and donor/cathode Schottky junction (a double-junction model) in polymeric BHJ solar cells was confirmed by various measurements. An observed negative-capacitance behavior marks the onset of a predominant charge recombination process occurring in one of the two junctions and is found closely related to the device V_{oc}. By studying different BHJ systems, we found that the V_{oc} is determined by the junction with a smaller negative capacitance onset and that the cathode modification can tune the V_{oc} maximum from the Schottky junction limited regime to the donor/acceptor junction limited regime. The negative capacitance and V_{oc} are limited by the same charge recombination process at either the donor/cathode or donor/acceptor interface.

The ultimate goals of this thesis are to understand the degradation mechanisms of organic solar cells, to develop new strategies that can be used to improve device stability and are compatible with device flexibility and ease of fabrication, and to achieve an in-depth insight into the origins of limitation of V_{oc} by both the cathode interface and donor/acceptor interface in BHJ organic solar cells. It is my hope that this work will provide a foundation for the continued research into this direction of organic solar cells.

6.2 Recommendations for future directions

The future research directions on organic solar cells are suggested as follows.

1. Further disclose the origins of V_{oc} by various recombination processes by combination of the EL emission and negative capacitance onset in impedance spectroscopy around the forward bias voltage of V_{oc}. It is necessary to verify the influence of both radiation and non-radiation recombination on the open circuit voltage, and find out the dominated recombination process, including exciton recombination, trap-assisted recombination, geminate recombination and bi-molecule recombination, to primarily limit device performance. And quantify their contributions to the limitation of V_{oc} in different organic solar cells. Studies of the pathways for recombination at donor/acceptor interfaces are instructive to designs for new molecules and device structures.
2. Identify the method to reduce degradation at the anode/organic interface. Due to its acidic and hydrophile properties, PEODT:PSS should be replaced with a different

anode interfacial layer to further improve device stability. Metal oxides such as MoO_3, NiO, V_2O_5, and WO_3 are good substitutes. Sputtering is a feasible method to deposit high quality films of these metal oxides, which will function as the transport and interfacial layer on anode for glass and flexible substrates.

3. Study the degradation of the organic active layer and better understand how oxygen and water molecules affect device performance. Besides chemical composition analysis by XPS and SIMS, EL, PL and impedance spectroscopy are good tools for correlating the physical property changes with the chemical changes occurred in the donor, acceptor, and donor/acceptor interface, which will be beneficial to fully understand the origins of the degradation in the organic active layer.
4. Develop solution based soft encapsulation techniques that are compatible with device flexibility and ease of fabrication. Encapsulation is necessary to stop water and oxygen from penetrating into the devices, thus will extend their lifetime.
5. Further improve the reproducibility of devices with metal oxide cathode interfacial layers by thermal evaporation, particularly in large-area devices. There are two aspects to affect chemical composition of metal oxide, reacted oxygen from air and deposition pressure decreasing during its deposition. For controlling oxygen content of metal oxide, it is better to introduce oxygen into chamber, to thus keep the oxygen partial pressure at a value during the whole deposition process.

Publications

Papers

1. Mingdong Wang, Qin Tang, Jin An, Fangyan Xie, Jian Chen, Shizhao Zheng, King Young Wong, Qian Miao, and Jianbin Xu, Performance and Stability Improvement of P3HT:PCBM-Based Solar Cells by Thermally Evaporated Chromium Oxide (CrOx) Interfacial Layer, ACS Applied Materials and Interfaces, 10, 2699–2702 (2010).

2. Mingdong Wang, Fangyan Xie, Weiguang Xie, Shizhao Zheng, Ning Ke, Jian Chen, Ni Zhao, J. B. Xu, Device lifetime improvement of polymer-based bulk heterojunction solar cells by incorporation copper oxide layer at Al cathode, Applied Physics Letter 98 183304 (2011).

3. Mingdong Wang, Fangyan Xie, Jun Du, Qin Tang, Shizhao Zheng, Qian Miao, Jian Chen, Ni Zhao, J. B. Xu, Aluminum Cathode Interface Degradation of Polymer Solar Cells and Reduced by Incorporation of Chromium Oxide (CrO_x) Layer, Solar Energy Material and Solar Cells, (in press).

4. Mingdong Wang, Ni Zhao, Shizhao Zheng, Ning Ke, Jun Du, Weiguang Xie, J. B. Xu, Limit of V_{oc} in Polymeric BHJ Cells Predicted by a Double-Junction Model, (be preparing)

5. Mingdong Wang, Fangyan Xie, Shizhao Zheng, Jianbin Xu, Stability Improvement of Polymer Based Solar Cells by Thermally Evaporated Cr_2O_3 Interfacial Layer, 2010 MRS Fall Meeting Proceeding (accepted).

6. Daoyun Zhu, Changxi Zheng, Mingdong Wang, Yi Liu, Dihu Chen, Zhenhui He, Lishi Wen, W.Y. Cheung, Materials Chemistry and Physics, 124 1146 (2010).

Patents

1. 2 U.S. patents pending

Conference presentations

1. Jianbin XU, Mingdong WANG, Qian MIAO, Qing TANG, Fangyan XIE, Jian CHEN, Ni ZHAO, Understanding Improved Stability of Organic Photovoltaic Devices, International Conference on Materials for Advanced Technologies (ICMAT2011) Singapore. (Invited talk);

2. Jian-Bin Xu, Q. Miao, Z. F. Li, M. D. Wang, Q. Tang and J. Du, Interface Engineering of Organic Thin Film Transistors and Organic Photovoltaic Devices, 2011 MRS Spring Meeting, USA (oral).

3. Mingdong Wang, Qin Tang, Jin An, Fangyan Xie, Jian Chen, Wong, Qian Miao, J. B. Xu, Performance and stability improvement of P3HT:PCBM based solar cells by chromium oxide interfacial layer, 2010 MRS Fall Meeting (oral)

4. Mingdong Wang, Jin An, Jianbin Xu, In-situ study of annealing process on morphology of BHJ solar cells by AFM, 2010 MRS Spring Meeting (Poster).

5. Wang Mingdong, Jian-bin Xu, A simple model to estimate the photocurrent and efficiency in hybrid BHJ solar cells, 2009 MRS Fall Meeting (Poster).

6. Wang Ming-Dong, Wu Yuan-yuan, He Zhen-Hui, Chen Di-Hu, Influence of Bias Voltage on ZnO Thin Films by CVAD for Solar Cells Application, 2008 Beijing-Hong Kong International Doctoral Forum (oral).

Curriculum Vita

Wang Mingdong

July 1982	Born in Shaoxing, Zhejiang Province, P. R. China
July 2001	Graduated from Shengzhou NO.1 High Middle School, Shengzhou, Shaoxing, Zhejiang Province, China
Sep. 2001—Jul. 2005	B. E. in Applied Physics Nanchang University, Nanchang, Jiangxi Province, China
Sep. 2005—Jul. 2008	M. E. in Condensed Solid Physics (Optoelectronic materials) Sun Yat-sen University, Guangzhou, Guangdong Province, China (Under supervision of Prof. Lishi Wen and Prof. Zhenhui He)
Aug. 2008—Sep.2011	Ph. D. in Electronic Engineering (Organic solar cells) The Chinese University of Hong Kong, Shatin, New Territories, Hong Kong (Under supervision of Prof. Jianbin Xu and Co-supervision of Prof. Ni Zhao)